LBL-20192

Actinide Production in ^{136}Xe Bombardments of ^{249}Cf

by

Kenneth Edward Gregorich

LBL--20192

DE86 002004

Nuclear Science Division
Lawrence Berkeley Laboratory
University of California
Berkeley, California 94720

This work was supported by the Director, Office of Energy Research, Division of Nuclear Physics of the Office of High Energy and Nuclear Physics of the U.S. Department of Energy under Contract DE-AC03-76SF00098.

Actinide Production in ^{136}Xe Bombardments of ^{249}Cf

Kenneth Edward Gregorich

ABSTRACT

The production cross sections for the actinide products from ^{136}Xe bombardments of ^{249}Cf at energies 1.02, 1.09, and 1.16 times the Coulomb barrier were determined. Fractions of the individual actinide elements were chemically separated from recoil catcher foils. The production cross sections of the actinide products were determined by measuring the radiations emitted from the nuclides within the chemical fractions. The chemical separation techniques used in this work are described in detail, and a description of the data analysis procedure is included. The actinide production cross section distributions from these ^{136}Xe + ^{249}Cf bombardments are compared with the production cross section distributions from other heavy ion bombardments of actinide targets, with emphasis on the comparison with the ^{136}Xe + ^{248}Cm reaction.

A technique for modeling the final actinide cross section distributions has been developed and is presented. In this model, the initial (before deexcitation) cross section distribution with respect to the separation energy of a dinuclear complex and with respect to the Z of the target-like fragment is given by an empirical procedure. It is then assumed that the N/Z equilibration in the dinuclear

complex occurs by the transfer of neutrons between the two participants in the dinuclear complex. The neutrons and the excitation energy are statistically distributed between the two fragments using a simple Fermi gas level density formalism. The resulting target-like fragment initial cross section distribution with respect to Z, N, and excitation energy is then allowed to deexcite by emission of neutrons in competition with fission. The result is a final cross section distribution with respect to Z and N for the actinide products. The successes and shortcomongs of this model are discussed and conclusions are drawn as to the roles of shell effects and nucleon equilibration in the dinuclear complex of damped heavy ion collisions.

ACKNOWLEDGEMENTS

Many people have helped me to make it through graduate school; directly, indirectly, knowingly, or unknowingly. Some deserve special thanks.

I wish to thank Glenn T. Seaborg. My association with him has always been a big inspiration.

The University of California and Lawrence Berkeley Laboratory have provided an ideal setting in which to work, learn and live.

Kenton Moody provided a lot of the initial guidance for my graduate study. His unique views on things such as science and his own way of getting things done have often been valuable tools.

Diana Lee helped with much of the chemistry and maintained many of the computer programs necessary for the handling and analysis of the data. Her cheerfulness and willingness to help were always appreciated.

Robert Welch was there through most of it (including the worst) and somehow added a bit of sanity to the whole place.

Thanks are in order to Wing Kot who also helped with the chemical separations and to Phil Wilmarth and all the other members of and visitors to the SHEIKS group, past and present.

Many thanks to the crews of the SuperHILAC for their skill and patience in delivering the beams.

I am indebted for the use of the ^{249}Cf target material to the Office of Basic Energy Sciences, U.S. Department of

Energy, through the transplutonium element production facilities at the Oak Ridge National Laboratory.

Darleane Hoffman has provided access to some new areas of research and is half of the reason for the delay in the preparation of this manuscript.

Special thanks to all my family, especially Mom and Dad for their constant enthusiasm and support.

finally, I would like to thank Teresa and "The Chubs" for being the other half of the reason the final stages of this work took so long (that's not a complaint)!

TABLE OF CONTENTS

SECTION 1 INTRODUCTION

In this work the proton number and neutron number distributions of the target-like fragments from transfer reactions between ^{136}Xe projectiles and ^{249}Cf target nuclei were studied. These measurements were made by catching the actinide products which recoiled out of a thin ^{249}Cf target in a metal foil and chemically separating the various actinide elements from this foil. The actinide isotopes were measured by monitoring the separated chemical fractions for their characteristic radiations. These transfer reactions will be arbitrarily divided into two categories called direct interactions and deep inelastic interactions. Before describing the experiments further, a description of these transfer reaction mechanisms is in order.

For more than the past decade there has been much interest in the study of deep inelastic reactions between heavy ions. This type of interaction can most simply be described by picturing a heavy ion projectile nucleus colliding with a heavy target nucleus. Rather than fusing to form a compound nucleus, the two nuclei remain in contact for a time as a dinuclear complex [GAT75]. This dinuclear complex remains together for several times 10^{-23} seconds; a time which is slightly longer than the time it would take the two nuclei to pass each other if there were no collision. The shape of this dinuclear complex can be described as being dumbbell shaped or as two touching, distorted spheres with some amount of overlap between the

two spheres. During the time the two nuclei are in contact, they can exchange nucleons, energy, and angular momentum. At the end of the contact time, the dinuclear complex will separate into a target-like fragment and a projectile-like fragment. Each fragment will have some proton number, neutron number, angular momentum, and excitation energy which is (probably) different from those in the projectile and target. These two fragments will separate with a kinetic energy between that corresponding to a grazing collision and that from a deformed Coulomb barrier. The separated fragments will then deexcite by emission of neutrons, charged particles, or gamma rays, or, in the case of the target-like fragment in the reactions to be studied here, prompt fission. These types of interactions can result in final products with a large net transfer of nucleons from the projectile to the target or vice versa. They usually result in a large amount of damping of the kinetic energy and some equilibration of the nucleons, energy, and angular momentum between the two fragments.

The direct transfer mechanism is much simpler than the deep inelastic transfer mechanism and usually happens in much more peripheral collisions. A few nucleons are transferred from the projectile to the target or from the target to the projectile, or both, with very little actual contact of the two nuclei. There is very little energy damping and these direct transfer reactions usually occur at the grazing angle. The nucleon distributions, the kinetic

energy damping, and the angular momentum distributions between the two fragments are essentially unequilibrated.

The N and Z distributions for the products of these transfer mechanisms have previously been studied [SCH78] [GAG81] [LEE82] [SCH82] [MSC82] [LEE83] [M0083] [SCH84] [WEL85] [HOF85] [GAG85]. As a general description of these distributions, it can be said that the yields peak near the N and Z of both the target and projectile and decrease as the number of nucleons transferred ($|\Delta Z| + |\Delta N|$) increases. This simple distribution is actually skewed to follow the valley of beta stability, so that the cross sections drop off more rapidly along a given mass number than in the direction of the valley of beta stability. In the experiments performed for this work, target-like products in the actinide region were studied. Since these products are in the actinide region, they have relatively low fission barriers and most of the actinide products from the initial distribution described above will undergo prompt fission during their deexcitation. Being able to study only the actinide products which survive fission during deexcitation, we are actually sampling only the low end of the excitation energy distribution of the initial distribution of the target-like fragments.

It was hoped that these heavy ion transfer reactions could be used for the production of new heavy elements and new isotopes of known elements. There were even speculations that the predicted island of superheavy

elements around Z = 114 could be reached via very large transfers from actinide targets [SCH78] [GAG81] [MSC82]. It was found, however, that the production of superheavy elements by transfer reactions is not possible because the distribution of mass and charge, at low excitation energies, does not extend far enough to reach the superheavy elements. It also appears that production of new isotopes with proton numbers greater than that of the target used is very difficult and may only be possible with very exotic targets such as ^{250}Cm and ^{254}Es [MOO83] [GHI84]. It appears, however, that production of new neutron-rich isotopes in the actinide region with fewer protons than the target used is possible with less exotic neutron-rich targets (^{238}U, ^{244}Pu, ^{248}Cm) and neutron-rich heavy ion projectiles (^{48}Ca, ^{86}Kr, ^{136}Xe) [MOO83] [MOO85]. The unknown nuclides accessible by these reactions are predicted to have half lives of one minute or less [KLA84] and new on-line chemical techniques must be developed before these nuclides can be studied [SUM84].

The previous studies of very heavy ion transfer reactions in the actinide region have used the most neutron-rich targets available, so the below-target neutron-rich cross sections were not measurable because the short half lives of the nuclides (many of them unknown) made them inaccessible by the chemical techniques used in the experiments [MOO83] [WEL84] [MSC82] [SCH78] [HOF85]. While the on-line chemical techniques are being developed for the

study of these neutron-rich actinides, it is necessary to measure these below-target neutron-rich cross sections from similar systems in order to be able to better predict the formation cross sections for the new neutron-rich isotopes. This was a major motivation for the study of the ^{136}Xe + ^{249}Cf reaction in this work. ^{249}Cf is relatively neutron-deficient so the neutron-rich below-target nuclides have relatively long half lives. Also, the neutron-rich Bk and Am isotopes are readily detectable using rather standard chemical separation techniques. Knowing the formation cross sections for the neutron-rich below-target isotopes from the ^{136}Xe + ^{249}Cf reaction should be an invaluable aid in predicting the below-target neutron-rich cross sections for new isotopes from reactions such as ^{136}Xe + ^{248}Cm.

The other motivation for studying the ^{136}Xe + ^{249}Cf system was to learn about the effect the position of the target nuclide with respect to beta stability has on the product cross section distribution. Again, since previous studies of very heavy ion bombardments of actinide targets used the most neutron-rich targets available, this effect has not been studied. As an aid in understanding this and in understanding this type of reactions in general, a modeling technique was developed for the prediction of the production cross section distributions.

SECTION 2 EXPERIMENTAL

2.1 OVERVIEW OF EXPERIMENTAL PROCEDURES

The experimental procedures described in sections 2.2 through 2.6 are all aimed toward the detection of the actinide products from the bombardment of a ^{249}Cf target with ^{136}Xe ions at energies just above the Coulomb barrier. The first requirement for such work is an accelerator capable of accelerating ^{136}Xe ions. The SuperHILAC and the principles behind its operation will not be discussed here. It may suffice to say that the choice of the ^{136}Xe projectiles was made with the capabilities of the accelerator being one of the prime considerations. The target system was already in existence and was used with only minor modifications. The procedure for making the target had been tested with the production of many lanthanide targets and some ^{248}Cm targets [ARM85]. The use of ^{249}Cf as the target material, with its much higher specific activity, presented some new challenges in the production and use of the target. Because of the high specific activity of the ^{249}Cf, and because of the different expected production cross section distributions, some new chemical separation procedures had to be developed. The detection of the radiations of the actinide products remained essentially the same as used in previous work, but more use was made of the gamma-ray activities in the trans-Bk elements. There was also a greater number of samples to be counted because of the new chemical procedures which were introduced.

2.2 TARGET PRODUCTION

There are many stringent requirements for a ^{249}Cf target which is made to be bombarded by heavy ions. Because of the relatively short half-life of ^{249}Cf (350.6 years) the californium in a target thick enough for this work will have an alpha decay rate of greater than 10^9dpm. Because of this large amount of activity, even a "minor" problem with this target which resulted in the removal of only a minute fraction of the target material could cause complex contamination and cleanup problems. The target material must have good adhesion to the backing material so that even under the stress of putting a pressure differential across the target, parts of the Cf deposit cannot flake off. The target must also withstand gas turbulence without loss of target material. The target backing and the target material must be physically and chemically stable under temperatures as high as a few hundred °C and under the strongly ionizing conditions which are present due to the passage of the heavy ion beam through the target. The target thickness must be very uniform so that the energy of the beam is well defined within the target and so that all of the reaction products can recoil out of the target. The method for making the target must be very efficient in terms of the use of the ^{249}Cf target material, both because of the rarity of ^{249}Cf and because of radioactive contamination problems.

A discussion of the advantages and disadvantages of the various target making procedures can be found in [MOO83]. It was found that a very satisfactory (and possibly the

best) method for making targets of transplutonium materials is that of molecular plating [AUM74] [MUL75] [EVA72]. This method produces targets with the target material in the oxide form on almost any inert metal backing. Targets made by the molecular plating method are very uniform in thickness and have very good adhesion to the metal backing. The Cf_2O_3 is chemically inert and has a high melting point. It is also very important that the procedure requires relatively simple equipment and can be performed within an enclosed glove box. For these reasons the molecular plating method was chosen and the ^{249}Cf targets were made as outlined in the following paragraphs.

The ^{249}Cf target material was obtained as $CfCl_3$ from the HFIR-TRU facility at Oak Ridge National Laboratory [BIG81]. All the procedures were performed in an enclosed box equipped with sealed gloves for handling the contents. About 1mg of the $CfCl_3$ was dissolved in 2M HNO_3 and the resulting solution was dried by heating in a water bath and gently blowing a clean N_2 jet on the surface of the HNO_3 solution. This process was repeated 2 more times to complete the conversion of the $CfCl_3$ to $Cf(NO_3)_3$. The dry $Cf(NO_3)_3$ was then dissolved in 3ml of isopropanol, forming the californium stock solution.

The plating was carried out in the cell shown in figure 2.2.1. The inside bore of the glass chimney has a diameter of 0.25". The Be backing foil is clamped between the bottom of the chimney and the steel base and an aliquot of the Cf stock solution is added which contains about 20μg of Cf

(enough to produce a layer of 50-75μg/cm2). Isopropanol is added to the cell until the level of solution is between 2 and 3 cm high. The Pt electrode is lowered into the solution to a height of 1cm above the backing foil. The Pt electrode which is connected to an audio speaker is agitated to cause mixing of the solution in the cell. A potential of several hundred volts is applied across the gap between the foil and the Pt electrode with the electrode being positive with respect to the foil. The current across the gap should be kept below 6mA/cm^2 to prevent bubbling in the solution and the poor deposit which results from a higher current density. After 30 minutes the plating is complete and the isopropanol solution in the cell is poured into a receptacle from which any remaining Cf can be recovered later. The cell is rinsed out with isopropanol and this wash is put in the same receptacle. Next the cell is taken apart and the target is removed and dried under a heat lamp. The target is then placed in an oven at 450-500°C for 30 minutes to convert the Cf deposit to the oxide form. The target is now ready for the deposition of another 50-75μg/cm^2 layer. This process is repeated until the target reaches the desired thickness.

The target thickness was measured after each layer of the plating process by measuring the decay rate of the ^{249}Cf with a surface barrier detector in a vacuum chamber with a target to detector geometry which gave an efficiency of 1.446×10^{-4}. The target used for all the bombardments in this work had a Cf thickness of 830±50μg/cm^2. A similar

target of some 650±40μg/cm^2 was also produced as a backup should something have happened to the first target which rendered it unusable. The target held up quite well during more than 100 hours of bombardments with up to 50 particle nanoamperes of ^{136}Xe at energies of about 6 MeV/A and is just now starting to show signs of damage. The thickness of the target was measured after each series of bombardments and it was found that no measurable portion of the target material was lost.

2.3 TARGET SYSTEM

The target system used in these experiments which were performed at the SuperHILAC has been described thoroughly in [MOO83] [MOO81] and will be discussed only briefly here. The Modular Fast Access Target System was designed for very heavy ion irradiations at the SuperHILAC and provides the necessary cooling for the target and isolation foil. It also provides the safety interlock systems necessary for the irradiation of targets made of rare radioactive materials. As implied in the name, this target system also allows fast access to the target and catcher foil.

A schematic of the target system is presented in figure 2.3.1 and an exploded view is presented in figure 2.3.2. The ^{136}Xe beam from the SuperHILAC enters from the left of the schematic and passes through a 6mm graphite collimator. This collimator is clamped in good thermal contact to a water cooled stainless steel flange. An electrical current signal is collected from this collimator assembly (which is electrically insulated from the beam line and the rest of the target system) to aid in the steering and focusing of the beam. The beam next passes through a vacuum isolation foil made of 1.8mg/cm^2 HAVAR. HAVAR is an alloy obtainable from Hamilton Precision Metals, Lancaster Pa. The composition of HAVAR is given in table 2.3.1. Just upstream of the HAVAR foil is a circular magnet which is used to suppress the loss of secondary electrons produced by the passage of the beam through the HAVAR foil in order to get

an accurate measurement of the beam current passing through the target and the isolation foil. Between the HAVAR isolation foil and the Be target backing foil is a small volume through which is passed a flow of N_2. This nitrogen flow is directed by means of jets onto the downstream side of the HAVAR isolation foil and the upstream side of the Be target backing to provide cooling. The nitrogen is then pumped out of this space. The N_2 flow and pumping speed are adjusted so as to keep the N_2 pressure between the isolation foil and the Be target backing at about 0.5 atmosphere. The isolation foil and the target backing are both mounted in good thermal contact to a second stainless steel flange. After passing through the Be target backing, the beam encounters the Cf_2O_3 target material. After passing through the Cf_2O_3 the beam passes through another volume of N_2 before being stopped in a 0.005" Ta beam stop which is cooled by water on the downstream side. Upstream of the target system is a device called a beam wobbler which consists of the outside coils of an electric motor installed around the beam pipe. When running an alternating three phase current through this wobbler the beam profile at the target is spread out so as to eliminate any unusually intense points.

The actinide products which are formed in the Cf_2O_3 layer recoil out of the target and are caught in a two piece gold catcher foil. The first piece is in the shape of a truncated cone to catch the products produced at wide angles to the beam axis. The second piece is a circular piece

which is clamped against the water cooled Ta beam stop and is meant to catch all of the products which recoil through the axial hole in the truncated conical first piece. Even though this second piece of gold catcher foil was in thermal contact with the water cooled Ta beam stop, it was often damaged by the passage of the beam. It was never melted through, however, and even if it were, the 6mm hole which would have been produced subtends only a small solid angle from the target. The gold foil thickness was chosen to be thick enough to stop the actinide products with the highest recoil energies. The kinematic limit on the recoil energy of the target-like fragment can be calculated by assuming that the projectile-like fragment recoils directly backwards with an energy corresponding to the Coulomb separation energy. This kinematic limit for the target-like fragment is 743 MeV for the highest energy bombardments used in this work and corresponds to a range in gold of 28 mg/cm^2 [HUB80], which is only slightly thicker than the 25 mg/cm^2 gold foils used in this work. It is unlikely that any actinide products will be formed with a recoil energy anywhere near this kinematic limit, so all the target-like fragments which enter the catcher foil should be stopped within the foil.

Figure 2.3.3 shows the probability of catching a product versus the angle from the beam axis at which that product recoils from the target (in the lab frame). This curve was calculated for each recoil angle by integrating over all azimuthal angles from all points on the surface of

the 6mm diameter target and finding the fraction which are subtended by the catcher foil. It is expected that all products from this reaction will be formed at, or forward of, the quarter-point angle (it has been found that at low energies, the quarter-point angle from the Fresnel scattering model is more appropriate than the classical grazing angle). Products formed in the most peripheral reactions should recoil at the target-like fragment's complement to the quarter-point angle. Products formed from more central collisions are expected to have more forward momentum transfer and will therefore recoil forward of the quarter-point angle. The heavy fragment's complement to the quarter-point angle for the highest energy reaction used in this work is at 44° in the lab frame and will move to more forward angles at lower bombarding energies [WIL80]. The only mechanism for having actinide products recoil backward of the heavy fragment's complement of the quarter-point angle is where the projectile and the target stick together for at least a large part of a revolution (rotating past a separation along the beam axis). Even for this type of interaction, a kinematic limit to the angle for the heavy fragment can be calculated, assuming that the products separate with their mutual Coulomb separation energy. The kinematic limit for the emission angle of the heavy fragment is at 69° in the lab frame. It would be expected, however, that any dinuclear system which had rotated through this large an angle would separate at a deformed Coulomb barrier energy which is significantly lower than the normal Coulomb

separation energy. This would cause the kinematic limit stated above to also move toward more forward angles. It can be seen from figure 2.3.3 and the above arguments that essentially all of the target-like products from this reaction should be stopped in the two piece combination gold catcher foil.

Several safety interlocks were installed along with this target system to protect the target from damage and to protect the accelerator from radioactive contamination in the case of a target failure. The most important of these is the slammer valve. This is a fast acting valve which will close in a matter of a few milliseconds to isolate the accelerator from the target system in the event of a sudden pressure rise on the accelerator side of the HAVAR isolation foil. The pressure rise is detected in either of two ion gauges near the isolation foil and the fast valve closing is accomplished by an explosive charge which drives a nylon wedge across the beam line about three meters upstream of the target. A vacuum tight seal is made by the nylon wedge within 3-4 milliseconds from the time of a steep pressure rise (as would be the case in the event of an isolation foil failure).

Other safety systems consist of a series of interlocks which can shut off the radiofrequency drivers for the accelerator. These interlocks are :

1) A beam limiting interlock which will activate when the beam current becomes greater than a preset value.

2) An IR interlock which consists of an infrared diode which will activate when the IR radiations from the target itself rise beyond a preset level.

3) A N_2 flow interlock which will activate in the case of interruption of flow of the N_2 cooling gas.

4) A water flow interlock which will activate in the case of an interruption in the flow of water to the beam stop.

5) A wobbler interlock which will activate in the case of an interruption in the operation of the beam wobbler.

The whole target system is contained within a glove box which is kept under negative pressure with respect to the surroundings. This prevents any airborne activity from escaping and is also helpful in preventing ^{249}Cf activity which accumulates on the various target system pieces from contaminating the surrounding equipment and personnel.

2.4 BOMBARDMENTS

^{136}Xe bombardments of the ^{249}Cf target were performed at three energies to outline a rough excitation function for each of the actinide products produced. The maximum ^{136}Xe beam energy available from the SuperHILAC is 8.5 MeV/A or 1156 MeV and was used as the highest bombarding energy for this work. At this incident energy, the energy of the beam after passing through the various parts of the target system was measured. This was done by putting the various parts of the target assembly in front of a low intensity beam of 1156 MeV ^{136}Xe ions and measuring the energy of the degraded beam with a surface barrier detector which was placed on the beam axis in the position of the beam stop. The energy of the undegraded beam was measured with the well calibrated SuperHILAC surface barrier detectors and with the phase probes. This beam was then put on the crystal in the beam stop position and the amplitudes of the pulses were measured with a Pulse Height Analyzer (PHA). This was taken to be 1156 MeV in the energy vs. channel number calibration of the PHA, and it was found that channel zero corresponded to near zero energy by the use of a ^{212}Pb alpha source. The energy vs. channel number curve was assumed to be linear over this range after correction for the pulse-height defect for the ^{136}Xe ions [MOU78] [WIL71]. The undegraded beam typically had a Full Width at Half Maximum (FWHM) of about 20 MeV. After passing through a 1.8Mg/cm^2 HAVAR foil, the beam energy was degraded to 1073 MeV and the FWHM had increased to about 25 MeV. Next a blank Be foil the same thickness as

that used for the ^{249}Cf target backing was inserted in the place normally occupied by the target and the N_2 cooling gas was allowed to flow between the Havar isolation foil and the Be foil. The energy of the beam after passing through these two foils and the N_2 cooling gas was measured to be 884 MeV with a FWHM of 35 MeV. Next the blank Be foil was replaced with the actual ^{249}Cf target and the beam energy measurement was made again. This time, however, because of the intense alpha activity from the target, the surface barrier detector had to be placed several inches away from the target at the end of a pipe in a specially constructed beamstop piece. The beam energy as measured through the target system was 856 MeV with a FWHM of 40 MeV.

All of the beam energy distributions for which the FWHM was given above had essentially Gaussian shapes. The beam energy width broadening is greater than would be calculated by range straggling and is probably due to nonuniformities in the thickness of the HAVAF isolation foil and the Be target backing foil. These energy losses and therefore these energies have been calculated with the range-energy tabulations of Hubert et. al. [HUB80] with the aid of the RANGY code. The RANGY code [MOO83] [WEL85], when given the data for the stopping power of Xe ions in various media from Hubert et. al. [HUB80] and the thickness and composition of the various media through which the beam passes, calculates the energies of the beam at the various points through these media. It was found that these calculations reproduced the experimentally measured energy

losses to within the accuracy of the measurements, so the calculated energy losses for the two lower energy bombardments were determined solely from the RANGY calculations. The results of the RANGY calculations for the three bombarding energies are presented in tabular form in table 2.4.1. The important result from these tables is that the energies in the ^{249}Cf target material corresponded to 1.16, 1.09, and 1.02 times the 736 MeV Coulomb barrier (calculated in the lab frame with r_0 = 1.4 fm).

A plot of the ^{136}Xe energy in the target vs. the incident beam energy is presented in figure 2.4.1. The centroid of the beam energy distribution at the beginning of the Cf_2O_3 target material is given by the upper diagonal line and the centroid of the beam energy distribution as it left the downstream side of the Cf_2O_3 layer is given by the lower diagonal line. It can be seen that at all three of the energies used in this work, the energy loss in the target material is about 28 MeV. The vertical solid lines represent the energy ranges of the centroids of the Gaussian energy distributions as the beam passes through the target. The vertical dotted lines represent this same type of energy range for beam particles whose energy at the beginning of the target system differed from the centroid of the beam energy distribution by 10 MeV, which is a typical Half Width at Half Maximun (HWHM) for the energy distribution of the undegraded beam. The lower horizontal line shows the Coulomb barrier as calculated with a radius parameter of 1.4 fm. The upper horizontal line is the Coulomb barrier

calculated with a radius parameter of 1.35 fm calculated as in [WIL80]. To get a more accurate picture of the actual energy distribution in the target, the Gaussian beam profile with a FWHM of 35-40 MeV at any point in the target was folded with the 28 MeV linear energy loss for the centroid of the distribution as the beam passes through the Cf_2O_3 target layer. The folding integral can be written as

$$P(E)=\frac{1}{\sigma\sqrt{2\pi}}\int_{EL}^{EH}\exp\left[\frac{-(E-C)^2}{2\sigma^2}\right]dC \qquad (2.4.1$$

where P(E) is the relative probability of finding a beam particle with a particular energy E. EH is the centroid of the energy distribution with HWHM=σ at the beginning of the target material and EL is the centroid of the Gaussian energy distribution as the beam leaves the target material. C is the centroid of the Gaussian beam energy distribution at any point in the target. This integral can be expressed as the difference of two error functions and takes the shape of a stretched Gaussian. A typical distribution is plotted on a vertical energy axis in figure 2.4.1.

The previous studies of Xe bombardments of ^{248}Cm targets done at the SuperHILAC were limited to energies from below the Coulomb barrier to just above the Coulomb barrier [MOO83] [WEL85]. The targets used in these ^{248}Cm bombardments were prepared on Be substrates that had thicknesses from 2.3 to 2.6 mg/cm^2. The ^{249}Cf target used in this work was prepared on a much thinner 1.8mg/cm^2 Be backing foil, allowing bombarding energies as high as 1.16

times the Coulomb barrier of 736 MeV in the lab frame (calculated with a radius parameter of 1.4fm). Since the target material is of the oxide form and because the target is thinner than that used in [MOO83] the energy lost by the beam as it passes through the target material itself is smaller, giving a better defined beam energy than in [MOO83].

The lengths of the bombardments were chosen to maximize the production of the nuclides of interest and minimize other products keeping in mind the lengths of the chemical procedures and the minimization of the total beam time required and these considerations will be further discussed in section 2.5. During the bombardments, a history of the beam current was kept by periodically writing down the total accumulated charge of the beam passing through the isolation foil, the target, and the beamstop as measured with a current integrator. In this way the variation of the beam current with time could be reconstructed. This reconstruction is important in calculating the cross sections of the short lived nuclides as described in section 3.5.

2.5 CHEMICAL SEPARATIONS

2.5.1 SEPARATION STRATEGIES

When performing reaction studies in the actinide region, the determination of isotopic yields by monitoring the radiations from chemically separated fractions is often the best technique. Actinide products are formed in heavy ion transfer reactions in relatively small yields: cross sections usually range from several nanobarns to a few millibarns. Unwanted activities are formed by prompt fission of target-like products and by reactions of the projectile with, in this case, the HAVAR isolation foil, the N_2 cooling gas, the Be target backing, the oxygen in the CF_2O_3 target material, and the catcher foil. Without sufficient purification, the characteristic radiations of the actinides are obscured by the radiations from the large number of unwanted activities. One appropriate method of achieving this purification is that of chemical separation. The use of chemical separations is also useful because of the Z identification it affords. Knowing the Z of the nuclides producing a given radiation is often helpful or necessary in identifying those nuclides. The chemical identification also helps in the determination of independent production yields in cases where feeding by radioactive parent activities occurs. Separation of the individual elements is also necessary in cases where two nuclides emit the same radiations and have similar half lives (such as is the case with the gamma-rays from the decay of 2.22h ^{250}Es and 3.22h ^{250}Bk).

There are some special requirements of the chemical separations used in this (and similar) work which are not required for chemical separations in general. The first of these requirements is that the separations and the equipment needed for them be fairly simple. Often the separations must be performed on short notice and/or at odd hours, so the pre-separation setup should be simple and require only a small amount of time. A simple procedure will often tend to be more reproducible. Much of the apparatus will become contaminated with radioactivity and cannot be used in subsequent separations (or possibly ever again). For this reason, the use of expensive equipment is prohibitive. A second requirement is that the separation procedure must be relatively fast. Some of the procedures to be outlined in section 2.5.5 are designed to detect nuclides with half-lives as short as 20m. A large number of the nuclides studied in this work have half lives of a few hours, so separation procedures much longer than this are not useful. High separation factors are the third requirement. Separation factors upwards of 10^6 are needed for a sufficient purification from the large amounts of unwanted activities produced in these bombardments. Separation factors of at least 100 between adjacent actinide elements are also often needed in order to clearly separate mother-daughter chains and to make visible low abundance activities which might be obscured by a very abundant activity from a neighboring element. The last requirement to be mentioned here is that of the production of a final sample which is

suitable for the counting of the radiations from the nuclides contained therein. Thin sources are required for the pulse-height analysis of alpha particles and fission fragments. Such sources were produced by the evaporation of a carrier-free, salt-free solution containing the fraction on to a platinum disc. The source requirements for the fractions to be monitored by gamma-ray pulse height analysis are not so strict. These sources may be produced by the above evaporation method (where it is not so important to have a "massless" sample). Another method for the production of the gamma-ray sources is to co-precipitate the activity with a suitable carrier and collect the precipitate on a filter paper which is then counted. It is also possible to perform gamma-ray spectral measurements on liquid samples in suitable containers, but the efficiency is lowered and is more difficult to determine.

The general strategy for the separation of the actinide elements in this work has been to perform a group separation of the elements of interest and then to separate the individual elements. Performing the group separation first prevents a repetitive clean-up of non-actinide elements from each actinide fraction (this separation order was not used in the fast Am separation in section 2.5.5 for reasons to be discussed there). Other considerations such as elution order and fraction tailing from column chromatography separations, addition and removal of carriers, and the ease of transition between steps dictated separation strategy and will be discussed in the following sections.

2.5.2 GROUP SEPARATIONS

One of the most important group separations used in this work is the separation of the actinides from the lanthanides. The chemical properties of the trans-plutonium actinides are almost identical to those of the +3 lanthanides due to the stability of the +3 ions in aqueous solution and the similarity of the ionic radii of these +3 ions. Lanthanide elements are formed in such large yields from fission of target-like reaction products and from the interactions of the Xe projectiles with the various components of the target system, that a highly efficient separation from them is necessary in order to be able to measure the gamma-ray activities of any of the actinide products. Two methods of performing this lanthanide-actinide separation were tested in this work: the 13M HCl cation column and the HDEHP/DTPA extraction chromatography column.

The 13M HCl cation column method has been found to be a very efficient method for the separation of actinides from lanthanides [HIG60] and was used in most of the separation schemes in this work. The column used was a 2mm diameter x 6cm long glass column fitted with a Pt tip to provide small volume drops (~10μl). The column was filled with Bio-Rad MP-50 cation resin (Macro-Porous) and pre-washed with 0.1M HNO_3 or 0.1M HCl to convert it to the acid form. The activities were loaded onto the column in <0.5M HNO_3 or HCl in a volume of less than 0.5 ml and run into the resin at a flow rate of <6 drops/min by applying pressurized N_2 to the

liquid on top of the column. The glass walls of the column were usually then washed with another small amount of the dilute acid and this was run into the resin. 13M HCl which had been freshly prepared by bubbling HCl gas through 12M HCl was then added to the top of the column and the elution was carried out at about 6 drops/min. the actinides elute ahead of the lanthanides in a broad peak between drops 12 and 30 with the higher Z actinides coming off slightly ahead of the lower Z actinides. Since the higher Z lanthanides elute ahead of the lower Z lanthanides, this procedure was tested with $^{170,171}Tm$ together with ^{241}Am and ^{254}Es (^{250}Bk, ^{250}Cf) tracers. An elution curve for this test is presented in fig. 2.5.1. A similar procedure using HCl-20% ethanol which was freshly saturated with HCl gas was also tried with similar results.

There are limitations inherent in this procedure, as there are with any. One of these limitations is the inconvenience of the production of the 13M HCL. Another is the separation time of about 5 to 20 minutes. The main limitation of this procedure, however, is that when run at speeds necessary for rapid separations,it produces broad elution peaks with strong tailing. Because of this, in order to keep all of the lanthanides out of the actinide fraction, it is necessary to leave some of the actinides (usually <10%) behind in the lanthanide fraction.

Another type of lanthanide-actinide separation was tried without much success. This method is the bis(2-ethylhexyl)orthophosphoric acid (HDEHP) /

diethylenetriaminepentaacetic acid (DTPA) extraction chromatography column [FIL74] [WEA68] [ALI71]. In this procedure, the stationary phase was prepared by coating teflon beads with HDEHP as in [FIL74] and packing these beads in a 2mm x 5mm glass column. The activities were eluted through this column with 0.025M DTPA in a monochloroacetic acid buffer at pH = 3.0. The actinides do elute ahead of the lanthanides, but when this column is run at the speeds necessary for this work, the peaks are so broad that an efficient separation is impossible. Another limitation of this procedure is that the final fraction is in a DTPA complex form and contains the components of the buffer solution used in the mobile phase.

Another group separation used in this work is the adsorption of Th through Pu (in charge states of +4, +5, and +6) on anion exchange resin from a strong HNO_3 solution [COL65]. In the strong HNO_3 solution most all other activities do not adsorb on anion exchange resin. After washing all of the other activities through the column, these high charge state actinides can be selectively removed from the column one at a time. This procedure and its limitations will be discussed in section 2.5.5 and can be found in [MOO83].

The last group separation to be discussed here is the LaF_3 coprecipitation procedure. This is a selective and quantitative coprecipitation for lanthanides, actinides, Sc, and Y from essentially all other elements. In this procedure the solution containing the activity is made up to

be 1-3 M in H^+ and about 1M in HF. Ba^{+2} and Zr^{+4} holdback carriers are added along with about 1 mg of La^{+3} carrier [PEN60]. The resulting solution is allowed to sit for 2-5 minutes to allow the precipitate to form. This precipitation was usually performed as the last step in chemical separations which produced fractions to be monitored for gamma-ray activities so the supernatant and precipitate were filtered through a nitrocellulose filter paper. The precipitate was then washed with a few ml of a 1M HF / 1M HCl solution on the filter. The filter could then be removed and mounted on a standard gamma-ray counting card for measurement of the gamma-ray activities. This procedure gives >95% chemical yield, with the main limitations being the addition of La+3 carrier, and the 2-5 minute time required for the formation of the precipitate.

2.5.3 α-HIBA COLUMN

The +3 ions of the elements from Am through Md have very similar chemical properties (as do all of the +3 lanthanides). Separation is made possible, however, by the decreasing ionic radius of these elements with increasing Z. One of the most efficient methods of separation of these +3 ions from each other is that of eluting from a cation exchange column with α-hydroxyisobutyric acid (α-HIBA) [CHO56] [GRC56] [STE61] [SMI56]. From these columns, the high Z elements elute first with sufficient separation between adjacent elements for an essentially complete separation.

The α-HIBA columns used in this work were Pt tipped

glass columns (2mm x 6cm) which gave a drop size of about 10μl. The columns were packed to a height of 5cm with of Benson BCx12 cation exchange resin (available from the Benson Company, Reno, Nevada). This resin consists of spherical, carefully sized particles (7-10μm). The column was placed in an aluminum heating block which was kept at 70°C and the resin was pretreated with 0.5M NH_4Cl to convert the resin to the ammonium form. The activity was loaded onto the column in about 50μl of a 0.1M HNO_3 solution and run into the resin by applying pressurized N_2 to the top of the liquid. The glass walls of the column were then washed with another 50μl of the 0.1M HNO_3. To remove the acidity from the column, 100-200μl of 0.5M NH_4Cl was passed through the column. Next a volume of 0.5M α-HIBA which had previously been adjusted to a pH of 3.70 by addition of NH_4OH was loaded onto the column and allowed to sit for 2-3 minutes in order to reach thermal equilibrium with the heating block. The actinides were then eluted at a flow rate of about 4 drops/min and the various fractions were collected either directly on Pt discs or in centrifuge cones for further chemical processing or later source preparation.

The above procedure was used to separate the elements from Md through Bk in about 20 minutes. In order to be able to make the sources for counting immediately (without first monitoring the fractions to find the exact elution positions of the various elements as was done in the slower separations of the foils from the long bombardments in this work) the elution positions had to be accurately known and

reproducible. These elution positions and their reproducibility were determined by calibration runs using available actinide and lanthanide tracers. By comparing the actual elution positions of these elements with the published elution positions (p. 16 of [HIG60]), the elution positions of the elements for which tracers were not available (Md and Fm) could be determined. Figure 2.5.2 shows a calibration run in which $^{170,171}Tm$, ^{90}Y (freshly separated from ^{90}Sr by a HNO_3 precipitation and 3M HCl cation exchange column method), ^{254}Es (containing ^{250}Bk and ^{250}Cf daughters), and ^{153}Gd were used. When the peaks of the actual elution positions are plotted against the published elution positions, a straight line results. Since the published elution positions are all the positions minus one free column volume, the free column volume of the column in the calibration run is found at the X-intercept of this straight line. The elution positions of Md and Fm can be found from this plot by reflecting the published positions through the line as is shown in fig. 2.5.2. When the temperature of the column and eluting solutions are carefully controlled, the volumes of the load and the washes are kept to the specified values, and most importantly, the pH of the α-HIBA solution is kept at precisely the right value, the reproducibility of the elution positions was found to be quite good. The positions of the elements coming off the column early were found to vary by no more than one drop and the positions for those coming off the column later were found to vary by no more than a few drops.

This reproducibility along with the distance between the peaks for adjacent elements made the production of sources for each element, without prior monitoring of the radiations, possible. An elution curve for a typical calibration run is presented in fig. 2.5.3. The logarithmic scale on the abscissa should be noted. It should also be noted that the α-HIBA column procedure used in the separation of the actinides from the long bombardments (similar to that used in [LEE82] and [LEE83]), although much slower, gave even better separation of the actinide elements.

The main limitation of this procedure is due to the tailing of the peaks which causes small amounts of the elements which elute from the column early to appear in later fractions. In this work, this tailing was not a problem for the trans-Cf elements because the elements are eluted in order of decreasing Z and the trans-Cf yields increase with decreasing Z. This tailing does become a problem, however, for the elements Am through Bk. In several of the bombardments the aluminum cover foil (see section 2.3) broke either due to a "shrinking effect" observed from thermal interaction with the beam or due to turbulence while pumping down the recoil chamber before the bombardment. This broken cover foil allowed thermal transfer and "knock over" (a process similar to the self-transfer of ^{252}Cf) to deposit up to 10^6 dpm of the ^{249}Cf target material onto the catcher foil. If even a very small fraction of this ^{249}Cf tails into the Bk, Cm, or Am fractions, the monitoring of

low level activities in these fractions becomes impossible.

2.5.4 HDEHP EXTRACTION CHROMATOGRAPHY COLUMN

It was shown as early as 1957 that extractions with bis(2-ethylhexyl)orthophosphoric acid (HDEHP) afforded a separation of lanthanides from each other [PEP57]. The multi-plate method of extraction chromatography used in this work was developed in 1962 [WIN63] and was refined and thoroughly studied several years later [HOR69] [EPH69] [HOR72]. In contrast to the α-HIBA elution, this extraction chromatography method allows the removal of the transplutonium elements from the column in order of increasing Z, thus avoiding the tailing problems for Am through Bk separations mentioned above. The elution order from this technique affords another advantage over the α-HIBA cation exchange column for the separation of the short-lived isotopes of Am through Bk because these elements are eluted from the column early, making these short-lived activities available in a relatively short time.

Before this method could be used, a rather extensive procedure for the preparation of the stationary phase column material was required [EPH69]. About $50cm^3$ of the diatomaceous earth (Celite-535) was washed several times with 0.1M HCl. This washed product was then sized in a simplified version of the settling apparatus used by Aly and Latimer [ALY67]. This apparatus consisted of a single glass tube with an inside diameter of 2cm fixed in a vertical position and fitted on the bottom side to a solvent metering pump. Arrangements were made to collect the solution

exiting from the top of the tube. About $4cm^3$ of the washed Celite-535 was placed in the tube and the solvent metering pump was adjusted to give a vertical flow of 0.1M HCl in the tube of 1.0 cm/min. All of the smallest particles with settling rates of less than 1.0 cm/min were expelled out the top of the tube. It was necessary to occasionally stop the flow and gently mix the contents of the tube because the smaller particles tend to coalesce into larger particles and settle out. Once it was found that only a small number of small particles were coming out the top of the settling tube, the metering pump was adjusted to give a vertical flow rate of 3.8 cm/min. The particles which came out the top of the settling tube at this flow rate were of the desired size with settling rates between 1.0 and 3.8 cm/min [EPH69]. This sized fraction was thoroughly dried and then placed in a desiccator and exposed to dichlorodimethylsilane vapors under vacuum for several days. During this exposure to the dichlorodimethylsilane vapors the celite was occasionally stirred by means of a magnetic stirring bar and the HCl vapors which accumulated were evacuated. After the treatment with dichlorodimethylsilane the now hydrophobic celite was soaked in an acetone solution containing 88 mg of HDEHP per gram of celite. Once the acetone was thoroughly evaporated, the HDEHP coated support was ready for use.

The column used for this procedure was a 2mm inside diameter glass column fitted with a Pt tip which gave a drop size of about 10µl. A small plug of glass wool was packed into the bottom of the column. A 1 cm length of the

hydrophobic celite was placed at the bottom of the column (on top of this first glass wool plug) in order to catch any HDEHP which came off the support above it in the column and keep it out of the chemical fractions. This support (as well as the HDEHP coated support) were added by placing enough of the material in the dry form to the column to fill it about 0.5 mm high. This material was then tightly packed with a glass rod which had been drawn out to a diameter just smaller than the inside diameter of the column. This layering was repeated until the column had the desired height. After the HDEHP-free section of the column was packed, another plug of glass wool was added and on top of that plug 5 cm of the HDEHP coated celite was added. The column was topped off with a final plug of glass wool which aids in the addition of aqueous solutions to the top of the hydrophobic column material. The air was removed from the column by running freshly degassed water through the column under high pressure. This type of column has been used for several kinds of actinide separations which are outlined in the following paragraphs (the first of which was used extensively in this work).

The HDEHP/HNO_3 extraction chromatography system is particularly well suited to the separation of small amounts of Am and moderate amounts of Bk from large amounts of Cf as was required in this work. When .4M HNO3 is used as the eluting solution, Am+3 is removed from the column shortly after the first free column volume. In this procedure, the column is kept at 70°C by means of a thermostated heating

block and the activity is loaded onto the column in about 50ul of a 0.1M HNO_3 solution. The walls of the glass column are washed with another 50ul of the 0.1M HNO_3. Pre warmed 0.4M HNO_3 is then used as the eluting solution. Fractions are collected at a drop rate of up to 10 drops/min. A typical elution curve for this procedure is presented in figure 2.5.4 for Am^{+3}, Bk^{+3}, Cf^{+3}, and Es^{+3}. Some Ba^{+2} was also added and the +2 ions are all eluted during the loading and washing of the column making the separation of a No^{+2}, Ra^{+2} fraction possible as explained in section 2.5.5.

There are a few limitations inherent in this procedure. The first limitation is because the elution positions of Cf^{+3} and Es^{+3} are nearly identical so that a separation of these two elements is impossible with this system. Also, the elution positions of Am^{+3} and Cm^{+3} are so close together that a separation of these two elements requires more precise techniques than are used in this procedure. Again, there is some tailing of the early fractions into the later fractions but this is not important in this work because the yields of Am isotopes are much smaller than those of Bk which are in turn much smaller than those of Cf.

The column from above has also been used for the separation of the elements from Es through Md. These elements can be eluted from the column sooner than in the above procedure by increasing the acid concentration to 0.8M HNO_3 [HOR73] [PHO69]. It has been found that Tb^{+3} should elute between Fm^{+3} and Md^{+3} [HOR75] so a small amount of ^{160}Tb tracer was added at the beginning of the following

procedure. The Es through Md activities were produced in the interaction of 157.4 MeV ^{22}Ne with a ^{254}Es target (the same target and bombarding system which were used in [SCH84]). After an initial cleanup similar to that used in the long bombardment procedure in section 2.5.5, the actinide activities were loaded on the column in 0.1M HNO_3 and run into the support. The walls of the column were washed with another small volume of 0.1M HNO_3 and this was also run into the column. The activity was eluted at 70°C with 0.8M HNO_3 at a flow rate of 5 drops/min. The elution curve from this run is presented in figure 2.5.5. It should be noted that drops 15-20 contain only a small amount of Fm and drops 20-25 contain only a small amount of Es, so the separation between Es^{+3} and Fm^{+3} is essentially complete. The position of the Tb tracer can be used for future calibrations of this procedure when the Fm-Md activities are not available.

The above column has also been used for the separation of Ac^{+3} from +1 and +2 ions and from the other +3 actinides in the following procedure in which several μg of ^{227}Ac of unknown origin was separated from its daughters and from other actinide impurities. The activity is loaded on the column (which had previously been prepared with water) in 0.050M HNO_3 and the +1 and +2 ions are washed through. A volume of 0.1M HNO_3 is added to the top of the column and run through at a flow rate of 1-2 drops/min. Actinium is eluted well ahead of the other +3 actinides.

A fast separation procedure for No^{+2} from heavy ion

bombardments using a similar column has also been developed making use of the chemical properties of No [HUL83]. This separation uses a 2mm x 2cm column of the HDEHP coated celite. The No is produced in light-heavy ion bombardments of ^{249}Cf, ^{249}Bk, and ^{254}Es targets and is quickly transported to the chemistry laboratory by means of a KCl aerosol loaded He gas transport system [WOL76]. The KCl containing the activities is collected on an Al disc kept in vacuum at the end of the gas jet capillary. At the end of the collection time, the Al disc is removed and the KCl + activity is picked up in 20 l of water. This is loaded on the top of the HDEHP column (which had been previously prepared with water and is kept at 70°C) and passed into the column. 100μl of water is added to the top of the column and is run through, removing all of the +1 ions. 0.1M HNO_3 is then added to the top of the column and run through. The +2 fraction containing the No^{+2} is collected in 2-4 drops at the end of the first free column volume on a heated Pt disc and dried. The No fraction can be ready for counting by alpha particle pulse height analysis in as little as 2 min. The main limitation of this procedure is the presence of Ra^{+2} in the No^{+2} fraction.

The HDEHP/HNO_3 extraction chromatography column system has been found to be a useful and versatile system for actinide separations. The simplicity and speed of the procedure make it preferable to α-HIBA cation exchange column and other systems for the separation of actinides in many cases. Individual columns used in this work have been

reused for upwards of 20 separations without much degradation in the results. The only major drawback to this system is the lack of separation between Cf and Es and the poor separation between Am and Cm.

2.5.5 SEPARATION SCHEMES

The chemical separation procedures from the preceding sections have been combined with other standard techniques for efficient separation schemes. These separations schemes were optimized to obtain the greatest amount of information about the actinide production in these bombardments with a reasonable number of bombardments and a minimization of accelerator time. These considerations called for four bombardments at each bombarding energy.

The first of these bombardments was used to normalize the chemical yields of the +3 actinide fractions from the other bombardments. A group separation of the +3 actinides was performed after a bombardment of 3-4 hours. The addition of ^{241}Am and ^{254}Es tracers at the beginning of the separation allowed accurate determination of the chemical yield of this fraction. The cross sections for one or more nuclides for each of the elements in this fraction allowed the normalization of the chemical yield for fractions from other bombardments where radioactive tracers could not be used because they would interfere with the determination of some of the nuclides of interest.

This separation was performed by dissolving a gold catcher foil in hot aqua regia, cooling the resulting solution, and extracting the gold into diethyl ether. The

aqueous solution left from the extraction was then dried at about 100°C in an oil bath with nitrogen gas blowing on the top of the solution to cool it and speed the evaporation. The resulting deposit was then picked up in 0.1M HNO_3 and run through the 13M HCl cation exchange column as explained in section 2.5.2. The actinide fraction from this column was diluted and a LaF_3 precipitation was performed as described in Section 2.5.2. This LaF_3 precipitate contained essentially only the +3 actinides and was counted for the characteristic gamma-rays of the elements therein. The production cross sections for ^{244}Am, ^{246}Bk, and 8.6h ^{250}Es were used for normalization of the chemical yields of the respective elements in subsequent bombardments at the same bombarding energy. A flow diagram of this separation scheme is presented in figure 2.5.6.

The second chemical separation was performed after a 2-3 hour bombardment and was meant to measure the production cross sections for the short lived isotopes of Cf through Md which decay by alpha particle emission. In this separation, a gold catcher foil is dissolved in hot aqua regia, the gold is extracted into diethyl ether and the resulting aqueous solution is dried as above. This activity is washed with 50ul of water and dried again to remove any residual acidity. The activity is then picked up in 0.1M HNO_3 and loaded onto the α-HIBA cation exchange column which is run as in section 2.5.3. The resulting actinide fractions are immediately dried on Pt discs and counted for alpha and spontaneous fission decays. If any of the fractions are to

be counted for gamma-rays, the 13M HCl cation column procedure can be inserted before the α-HIBA column. In this case, the activity, after drying the aqueous phase from the ether extraction, would be picked up in 0.1M HNO_3 and run through the 13M HCl cation column. The resulting actinide fraction in saturated HCl is then dried. The residue is washed with 50ul of water and dried to remove any residual acidity. The activity is then picked up in 0.1M HNO_3 and run through the α-HIBA column as above. The total separation time for the first fractions eluting from the α-HIBA column is about 40 min for the procedure without the 13M HCl cation column. Inserting the 13M HCl cation column adds about 15 minutes to the procedure. A flow diagram of this separation scheme is presented in figure 2.5.7. Nuclides such as 30 min ^{250}Fm, 43.6 min ^{245}Cf, 19.7 min ^{244}Cf and 28 min ^{254}Md have been detected by this method, the identification of the latter two nuclides being somewhat questionable because in the case of an identification based on only a few events it could not be proven that a small Fm contamination could not account for the events. This procedure also provided another measurement of the production cross sections of nuclides with half lives less than a few days which were also measured in the long bombardment described below. This procedure also provided the best information on the production of nuclides with half lives shorter than a few hours such as ^{249}Es, 2.2 hr ^{250}Es, and ^{247}Cf.

The third bombardment was again a 2-3 hour bombardment

in which the catcher foil was processed to detect the gamma radiations from the short-lived neutron-rich Am and Bk isotopes. A separation for No and Ra was also worked into this scheme. In this procedure, the gold catcher foil was dissolved in hot aqua regia, the gold was extracted, and the aqueous phase was dried as above. The residue was washed with 50μl of water and dried again. This was then picked up and loaded on the top of the HDEHP/HNO_3 extraction chromatography column. The column was run as described in section 2.5.4 except that the wash with 0.1M HNO_3 was extended until the +2 fraction was removed from the column. This fraction was put aside for later processing. The Am fraction was collected directly on to the top of a cation exchange column as used with the 13M HCl separation. While the Bk fraction was collecting, the Am fraction was immediately run through the 13M HCl cation column as described in section 2.5.2. The Am fraction from this column was then diluted and a LaF_3 coprecipitation was performed as in section 2.5.2. The Am fraction was ready for gamma-ray counting within 35 min from the end of bombardment and was clean enough to allow identification of 39 min ^{246}Am and 25 min ^{246}Am on the basis of only a small number of counts. The Bk fraction was run through a 13M HCl cation column and coprecipitated with LaF_3 in a manner similar to that for the Am fraction and was ready for counting within one hour after the end of the bombardment. This allowed detection of 56 min ^{251}Bk and provided the best information on the production of ^{250}Bk. The Ra, No fraction

had to be cleaned of residual gold by passing it through an anion exchange column in 2M HCl. An alpha source was made by drying the eluate from this anion column on a Pt disc. The No, Ra fraction was ready for counting within 1.5 hours after the end of bombardment. No ^{259}No was ever observed: some isotopes of Ra were seen but in most cases it is not clear if they were produced directly or if they are radioactive daughters of other activities, so the Ra results will not be presented in this work. A flow diagram of this separation scheme is presented in figure 2.5.8.

The last bombardment at each bombarding energy was a long bombardment (>24 hours) meant to determine the production cross sections of all the long-lived (>2-3 hours) actinide isotopes produced. The separation procedure used for this bombardment was a more comprehensive scheme capable of separating all elements from Ac through Md. The main features of this separation scheme are an α-HIBA cation column separation for the transplutonium elements and an anion exchange column procedure for the separation of the Th through Pu elements. A flow diagram of the separation scheme for the foils from the long bombardments is presented in figure 2.5.9 and a similar procedure is described in [MOO83] and in [WEL85]. The procedure is presented briefly here making special note of the differences from the procedures in the above references.

The gold catcher foil from the long bombardment was dissolved in aqua regia and the resulting solution was run through an anion exchange column. The transplutonium

actinides were washed through the column with 9M HCl. It is at this point that the procedure splits: the processing of the transplutonium fraction will be explained later and the processing of the Th through Pu elements treated here. The Th through Pu elements are stripped from this anion column with a series of solutions including 3M HCl, H_2O, $FeCl_2$, Zn^{+2}, and HCl/HF. Metallic Zinc is added to this solution to reduce the U and a LaF_3 coprecipitation is performed. The precipitate is dissolved in H_3BO_3/HNO_3 and the resulting solution is loaded on a second anion column. This column is washed with 8M HNO_3 and then 9M HCl. The Pu is reduced and removed from the column in 1:10 HI/HCl. Next, the Np is removed with 4M HCl/0.1M HF. The Th is removed with dilute HCl and the U is removed with water. Each of these fractions is prepared for alpha and gamma counting by drying on a Pt disc.

The transplutonium fraction was then treated in a fashion similar to that used by Hoffman et. al. [HOF85]. The solution containing the transplutonium activities from above was then run through an anion exchange column in 2M HCl to get rid of any residual gold, and then dried. The activity was picked up in 0.1M HNO_3 and run through a 13M HCl column as in section 2.5.2 to remove the lanthanide activities. The transplutonium fraction was then dried, washed with a small volume of water and dried again. The resulting fraction was picked up in 0.1M HNO_3 and loaded on a cation exchange column similar to the one mentioned in section 2.5.3. After several washes with water and 0.5M

NH_4Cl, the actinides from Md through Cf were eluted sequentially with 0.5M α-HIBA at a pH of 3.7. After the Cf was removed from the column, Bk, Cm, and Am were each eluted with 0.5M α-HIBA at a pH of 3.9. The eluate from the α-HIBA column was collected in many fractions of a few drops apiece which were monitored for alpha and spontaneous fission activity to locate the exact elution positions of each of these elements. The appropriate fractions were combined to produce fractions containing each of the elements from Md through Am. These elemental fractions were then dried on Pt discs and flamed before being counted for alpha, spontaneous fission and gamma radiations.

This procedure yielded suitable sources for the elements from Np through Md. The Th and U sources were too thick for alpha pulse height analysis measurements and for this reason were only counted for gamma-rays. The Pa usually ended up in the Np fraction, but its chemical yield was not reproducible. The Am through Cf fractions contained appreciable amounts of the ^{249}Cf target material which hindered some of the alpha measurements. All fractions became ready for counting between 4 and 8 hours after the end of the irradiation. After gamma counting was essentially finished on the Bk fractions, they were reseparated with the HDEHP/HNO_3 extraction chromatography column procedure to rid them of essentially all the ^{249}Cf activity. It was then possible to measure the production cross section of ^{249}Bk by monitoring the growth of the ^{249}Cf alpha group over the next several months.

2.6 DETECTION OF RADIATIONS

The gamma and K x-ray radiations of the actinide nuclides contained in the chemically separated fractions were monitored by taping the final chemical samples to standard counting cards and placing them in well calibrated positions (see section 3.4) in front of Ge(Li) and high purity germanium gamma-ray detectors. Five gamma-ray detectors were used varying in volume from 30 cm^3 to 70cm^3. The FWHM for the 1332 keV peak of ^{60}Co for these detectors varied from 1.8 to 2.1 keV. Spectra were collected with a system of 4096 channel multichannel analyzers. The fractions which were to be counted for their alpha radiations were all made by drying a small volume of solution containing the activity in as small an area as possible on Pt discs. These Pt discs were then placed within 4mm of surface barrier detectors with a 100mm^2 sensitive area (23±3% efficiency). There were two systems of four surface barrier detectors each. In each system, the four signals were multiplexed so that four 1024 channel spectra could be collected simultaneously. The analyzer systems for the alpha measurements were equipped with fission discriminators which, when a pulse occurred in the one of the surface barrier detectors which corresponded to an energy above 25 MeV, would put a count in the first channel of the corresponding spectrum. In all cases a series of histogrammed spectra was collected, so that the decay curves of the activities could be reconstructed later (sections 3.3,3.4). The strategies of choosing counting

intervals etc. to maximize the information gained on the nuclides of interest will be discussed in section 3.2.

SECTION 3 DATA ANALYSIS

3.1 OVERVIEW OF DATA ANALYSIS

The goal of the data analysis for this work is to calculate the production cross sections for the various actinides produced in the interaction of ^{136}Xe ions with the ^{249}Cf target at energies near the Coulomb barrier. The data are collected as a series of alpha and gamma spectra. The intensities of the various peaks in the series of spectra for a given chemical fraction are measured from the spectra by numerically integrating them and making background corrections where appropriate. From these integrations a decay curve is constructed which contains the decay rate vs. time information for the particular radiation of interest. This decay curve is fit with the appropriate exponential decay function (or combination of such functions). This fit provides both a more certain identification of the source of the activity by checking the half-life of the activity and it allows the extrapolation of the activity to the time at the end of bombardment or to the chemical separation time, whichever is appropriate. This initial activity is corrected for detection efficiency and for the abundance of the radiation (number of this type of radiation per decay) to give a decay rate at the end of bombardment. A cross section is calculated by taking into account the irradiation history for the particular bombardment. These cross sections are then corrected for chemical yield by normalizing the cross sections for some of the nuclides to the cross sections from a similar run in which a radioactive

tracer of that element was added at the start of the chemical procedure. There was usually more than one measurement of the cross section for a given nuclide, so a weighted average of the independent measurements was then taken for each nuclide that had more than one determination of its cross section at any given bombarding energy.

3.2 OPTIMIZATION OF COUNTING

In order to get the most production cross section information from the chemically separated fractions from a series of bombardments, the use of surface barrier and gamma-ray detectors and the counting of the fractions had to be carefully planned. All of the bombardments and separations described in section 2.5.5 were carried out within a 48 hour period for each bombarding energy, so the number of samples to be counted far exceeded the number of detectors . Usually every attempt was made to keep the counting intervals used for a given fraction smaller than about half of the half-life of the shortest-lived nuclide of interest within the fraction. This was done to lessen the need for corrections for non-linear decay rates during the counting intervals (see section 3.4 and appendix A). As the short-lived nuclides in the samples decayed away, the counting intervals could be increased.

The shorter bombardments were performed at the beginning of the run because the most important cross section information to be gained from them was from the shorter-lived isotopes. The counting of the fractions from the shorter bombardments could be ended when the fractions from the long bombardment became ready. In this way the fractions from the shorter bombardments were usually counted for more than 24 hours before the detectors were needed for other fractions. After the fractions from the long bombardment had been counted for several hours, they were occasionally removed to allow counting of the longer-lived

products in the other fractions.

The counting of the gamma-ray activities usually continued for two weeks, until the longest lived observable gamma-ray emitting actinides had decayed to non-detectable levels. The counting of the alpha particle activities continued for several months. Many of the alpha activities were observable for months or years, and often, extended counting was necessary to resolve activities with similar alpha particle eneregies by their different half-lives.

The Cf fractions from the long bombardments contained as much as 10^6 dpm of the ^{249}Cf target material. Because of the possibility of contaminating equipment in the "clean" counting room, these Cf fractions were counted in a separate detector chamber which was set up in the chemistry laboratory.

3.3 PEAK INTEGRATIONS

3.3.1 SIMPLE ALPHA PEAK INTEGRATIONS

In order to determine the activities of the various radiations seen in the spectra the areas of the peaks were determined by numerical integration procedures. These peak integrals were then arranged chronologically to form a decay curve.

Because of the low background in the alpha spectra, the numerical integration procedure was relatively simple. The computer code HALFA was written to carry out this procedure. HALFA would sum up the counts in various ranges of channels (chosen to contain the peaks of interest) in a series of spectra from a single chemical fraction and store this peak area as the average counts per time unit. The time from the end of the bombardment would be determined for each of the peak areas and a statistical error in the count rate would be calculated. This statistical error was calculated by taking the square root of the total number of counts in the peak and dividing by the length of the counting interval. In cases where the total number of counts in the peak was zero, the statistical error in the peak area was stored as -1 to signify some special error handling in the decay curve fitting program (the error usually used was that which would have resulted had there been one count in the integrated peak). These average count rates with their associated statistical errors and times for each energy peak in each fraction were arranged chronologically and the format was adjusted to be compatible with the decay curve fitting

program to be used.

3.3.2 FITTING OF ALPHA MULTIPLETS

For some of the more complicated alpha spectra where the activities overlapped and were long lived enough so that they could not be separated by multicomponent decay curve analysis, an alpha multiplet peak fitting code ALFIT3 was developed. The peak shape parameterization in ALFIT3 is a combination of the peak shapes used in SAMPO [ROU69] and ALFUN [WAT78]. It is a Gaussian smoothly joined to an exponential on the low-energy side with an additional additive exponential tail on the low-energy side. This additive exponential tail has been folded with the Gaussian part of the peak shape, the effect being that it is rounded by an error function at the peak centroid. (It may have been better to fold the additive exponential tail with the full Gaussian + exponential shape, but the folding integral was sufficiently complicated that the computation time would have increased by several times). The peak shape parameterization can be written:

$$F_1(x) = A\exp\left[\frac{B_1^2}{4B_2^2} + B_1(x-c)\right] + T(x)$$

$$; x < x_j = c - \frac{B_1}{2B_2} \qquad (3.3.1$$

$$F_2(x) = A\exp\left[-B_2(x-c)^2\right] + T(x) \quad ; \quad x \geq x_j \qquad (3.3.2$$

$$T(x) = \frac{AD}{2}\exp\left[B_3(x-c)\right]$$

$$\left(1 - \mathrm{erf}\left(\sqrt{B_2}\left(x - c + \frac{B_3}{2B_2}\right)\right)\right) \qquad (3.3.3$$

Where $F_1(x)$ and $F_2(x)$ are the exponential and Gaussian, respectively which are smoothly joined at x_j. The centroid of the Gaussian part is c and is taken as the exact energy of the peak. A is the amplitude of the Gaussian part of the peak at x=c. B_1 is the slope of the smoothly joined exponential and B_2 is related to the width of the Gaussian. B_3 is the slope of the additive exponential tail and D is the ratio of the height of the unfolded additive exponential tail to the height of the Gaussian at x=c. The area of the additive exponential is conserved by the folding procedure, so the total area of the peak can be found by integrating equations 3.3.1, 3.3.2, and the unfolded additive tail and is

$$\mathrm{AREA} = A\left(\exp\left[\frac{-B_1^2}{4B_2}\right] B_1^{-1} + \frac{\sqrt{\pi}}{2\sqrt{B_2}}\right.$$

$$\left.\left(1 + \mathrm{erf}\left(\frac{B_1}{2B_2}\right)\right) + \frac{D}{B_3}\right) \qquad (3.3.4$$

where erf is the error function. The derivatives of $F_1(x)$, $F_2(x)$, and T(x) can be taken with respect to each of A, B_1, B_2, B_3, c, and D, and a least-squares formalism can be used for the fitting. The equations to be solved for an error weighted least-squares solution can be found by starting

with Bevington's eq. 11-2 [BEV69] and following the derivation starting on page 44 of [SHO74]. In ALFIT3 the amplitudes of all the peaks belonging to a given nuclide are constrained to vary together i.e. the amplitudes of all of the peaks of ^{249}Cf are varied together in the midst of peaks due to other Cf isotopes. To keep matters simpler and to avoid more possibilities of erroneous fits, the centroids of all the peaks due to a single nuclide are also constrained to vary together. Any or all of the parameters above can be allowed to vary during the iterative least squares fitting allowing control of, for example, a calibrated peak shape.

ALFIT3, as the name implies is the third in a series of alpha multiplet fitting codes. ALFIT, the first of the series has a peak parameterization that consisted of a Gaussian smoothly joined to an exponential tail with no additive exponential tail. The parameterization in ALFIT2 is a pseudo-Gaussian smoothly joined to a pseudo-exponential tail, where the powers of the (x-c) terms in the equations similar to 3.3.1 and 3.3.2 are nonintegral and variable. It has been found that in most cases ALFIT3 gives the most satisfactory fits. ALFIT3 is a self-contained program written in FORTRAN77 which is capable of running on a micro-computer with at least 128k x 16 bits of memory.

A sample output file from ALFIT3 for the fitting of a ^{244}Cm spectrum is presented in figure 3.3.1 and figure 3.3.2. The output file begins with a summary of the activities used in the fit. In the example, a ^{244}Cm spectrum was considered to be due to two nuclides: the

5.806 MeV and the 5.6670 MeV peaks being due to the first nuclide and the 5.7640 MeV peak being due to the second nuclide. Next comes a record of how the various parameters varied during the iterative fit. In this case, all parameters were allowed to vary and they were found to converge after 7 iterations. A summary of the final parameters follows. Last is a channel by channel summary of the fit.

3.3.3 PEAK INTEGRATIONS FOR GAMMA-RAY SPECTRA

The peaks in the gamma-ray spectra, which were often too small to be found and accurately fit by automated peak search and fitting codes, were integrated in a way similar to that used for the simple alpha spectra in section 3.3.1. The main difference here is in the need for a subtraction of background. The NIBFW code was used for this purpose. For each peak in a series of spectra from a given fraction three regions are chosen in the spectrum. One region of channels is chosen which contains the peak. On the high and low energy sides of the peak, regions are chosen, as near as possible to the peak region, which are representative of the background in this portion of the spectra. for each of the background regions, a weighted average of the counts per channel is taken by the following formula:

$$\bar{A} = \frac{\sum_i a_i/\sigma_i^2}{\sum_i 1/\sigma_i^2} \quad ; \quad \overline{\sigma^2} = \left(\sum_i 1/\sigma_i^2\right)^{-1} \qquad (3.3.5$$

where a_i is the number of counts in channel i with i constrained to be in the background region and σ_i is the

statistical error in a_i or $a_i^{1/2}$. This value of the weighted average is put at the center of the background region for each of the background regions and the equation for the line connecting these two points is calculated. The gross area within the peak region is calculated by numerically summing the values in each of the channels within the peak region and subtracting the area under the line determined by the background regions within this peak region. This gives the net counts in the peak above background. A statistical uncertainty in this area is calculated and the peak area and the uncertainty are converted to count rates by dividing by the live time of the count interval. These average count rates with their associated statistical errors and the times of the beginnings of the count intervals were arranged chronologically for each peak in each fraction and the format was adjusted to be compatible with the decay curve fitting program to be used.

3.3.4 UPPER LIMITS ON AREAS OF NONEXISTENT PEAKS

Often, when an activity is not visible in a spectrum, a statistical upper limit on the activity which could exist and not be detected is desired. For the gamma-ray spectra in this work a straightforward formalism for determining these upper limits on undetected activities was developed. This formalism is based only on the definition of chi squared.

$$\chi^2 = \sum_{i=1,N} \frac{\Delta y_i}{\sigma_i^2} \qquad (3.3.6$$

Where N, in this case is the number of measurements (spectra) where the peak could have been expected to be seen had it been larger. Now assume that each spectrum has $0 \pm \sigma_i$ counts/minute. A single component of $A_0 \exp(-\lambda t)$ with $A_0=0$. will give $X^2=0$. Increasing A_0 by one standard deviation will increase X^2 by 1 so that $X^2=1$. Writing equation 3.3.6 out explicitly for this case where t is the time from the end of the bombardment gives:

$$X^2 = A_0^2 \sum_{i=1,N} \frac{\exp[-2\lambda t_i]}{\sigma_i^2} = 1 \qquad (3.3.7$$

and solving for A_0:

$$A_0 = \left(\sum_{i=1,N} \frac{\exp[-2\lambda t_i]}{\sigma_i^2} \right)^{-1/2} \qquad (3.3.8$$

Table 3.3.1 shows the result of this calculation for the calculation of the upper limit for the count rate of the 285 kev gamma-ray from ^{247}Am in the HDEHP extraction chromatography column separation for the highest energy run. It should be noted that this procedure gives the count rate for t=0, the time of the end of the bombardment, so the decay curve fitting procedure of section 3.4 is not used for these upper limits.

3.3.5 COUNT RATES FOR VERY WEAK GAMMA-RAY ACTIVITIES

Occasionally, the count rate for a gamma-ray activity is large enough to be significant if several spectra are summed together, but the count rates in the individual spectra are erratic or insignificant because of poor statistics. A method was used in this work for a few of the

gamma-ray activities which took the statistically significant peak area from a sum of several spectra and calculated the count rate at the time of the end of the bombardment. The total number of counts T during any one of the counting intervals can be written as

$$T = \frac{A}{\lambda}\left(\exp[-\lambda t_i] - \exp[-\lambda t_f]\right) \qquad (3.3.9$$

where t_i and t_f are the times of the beginning and end of the count interval (both are referred to the time of the end of bombardment). Summing over j spectra and solving for A_0, the activity at the end of the bombardment:

$$A_0 = T\lambda\left(\sum_j\left(\exp[-\lambda t_{ij}] - \exp[-\lambda t_{fj}]\right)\right)^{-1} \qquad (3.3.10$$

A typical result of this type of calculation is presented in table 3.3.2 for the count rate of the ^{239}Am from the long bombardment at the highest energy. Care should be used when employing this procedure to prevent the interpretation of statistical fluctuations in the background as peaks. For the few times when the procedure was used in this work, the nuclides were identified by more than one gamma peak. Again, this procedure gives the count rate at the end of the bombardment so the decay curve fitting procedure of section 3.4 is omitted.

3.4 DECAY CURVE FITTING

All decay curves were fit by an error weighted non linear least squares procedure. One of two computer codes was used. Again, the equations for the fits can be derived by starting with Bevington's equation 11-2 [BEV69] and following the derivation in [SGS74] as is done in [MOO83]. The first of these codes HOPELES is actually a modification of the FUTILE code of [MOO83]. The FUTILE code was modified by adjusting the average activity during each counting interval to correct for the non-linear decay during the counting interval and to correct for the dead time accumulated during the interval. This newly corrected activity is expressed as the activity at the beginning of the interval rather than the average activity during the interval. These corrections are explained further and listed in appendix A. The activities are adjusted in such a way during each iteration of the fitting procedure. The second decay curve fitting code used in this work is the EXFIT code. EXFIT is based on the same principles as HOPELES but is a self contained code for use on a microcomputer and is slightly more versatile than HOPELES in that it can fit more types of decay curves than can HOPELES. Both codes allow the user to vary any combination of or all of the half-lives and initial activities of the various components in the decay curve. Both codes have corrections for non-linear decay during the counting interval as an option during the running of the program. The output files of both of these codes give a history of the values of the

variable parameters during the iterations, a final listing of the parameters after convergence, along with their statistical uncertainties (calculated as the square root of the diagonal elements of the inverse matrix as in [BEV69]). Next a point by point by point listing of the fit is given, and finally comes a plot of the data and the fit. An example of a typical output file from EXFIT is given in figure 3.4.1 and 3.4.2.

3.5 EFFICIENCY AND ABUNDANCE CORRECTIONS

The initial activities from the decay curve fits had to be corrected for the efficiency of the detector for the specific radiation and for the abundance of that specific radiation. All of the fractions which were counted for alpha and spontaneous fission decays were counted on surface barrier detectors with active surface areas of 100mm^2 at a very close geometry. The efficiency for alpha particles of all energies was found to be 23±3% by measuring the count rate from standardized sources. The efficiency for the detection of one of the fission fragments due to a spontaneous fission event was taken to be twice that for alpha particles. Some error in this simple assumption for the efficiency for detecting alpha particles is present due to the varying areas of the alpha sources. Every attempt was made, however to keep the source areas small; they were usually 2 to 3 mm in diameter. It was assumed that the variation in the efficiency due to the source size was encompassed by the 3% error limit given to the alpha particle efficiency.

The determination of the efficiencies of the gamma-ray detectors is more complicated. In order to determine the efficiency vs. energy curve for each of the gamma-ray detectors, they were calibrated by counting a mixed radionuclide gamma-ray calibration source. The sources used for this calibration are available from Amersham Inc. and contain a series of well separated gamma lines with energies between 0 and 2 MeV. All fractions in this work were

counted from the closest geometry obtainable for each detector, so only a single efficiency vs. energy curve for each detector was needed. The areas of each of the peaks in the calibration spectrum was calculated as in section 3.3. when these areas were compared with the gamma-ray emission rate from the source (calculated by correcting for decay of the nuclides within the source since the source standardization date), a set of efficiencies for 11 energies between 0 and 2 MeV were obtained. This set of efficiencies were fit with the following functional form with the EFFITDO option of the SAMPO code [ROU69]

$$eff(E) = P_1(E^{P_2} + P_3 exp[P_4 E]) \qquad (3.5.1$$

The EFFITDO option of the SAMPO code performs a least squares fit of the data to determine the best values of the four parameters (P_1, P_2, P_3, P_4) in equation 3.5.1. This functional form is essentially an exponentially decreasing function in which the second term imitates the low energy absorption in the front end window of the detector. The statistical uncertainties in the efficiencies determined this way were usually taken to be ±5% which is meant to account for the uncertainties in the decay rate of the activities in the mixed radionuclide source (~4%), the uncertainties in the peak areas in the calibration spectrum due to counting statistics (<<1%), and the differences between the actual efficiencies and the functional fit (~2%).

All the initial activities were also corrected for the abundance of the particular radiation. These abundances and the uncertainties in these abundances were usually taken from [TOI77], except where more recent work turned up significant differences from these values.

When more than one radiation for a given isotope was measured, the decay-curve fitting and the efficiency and abundance corrections were performed as above. A weighted average of the resulting initial decay rates was then taken. In an effort to treat the published uncertainties in the radiation abundances as correctly as possible, in these cases, the relative intensities (and the corresponding uncertainties) for the individual radiations were used, and final adjustment for the absolute abundance (and the uncertainty in this normalization) was made after the weighted average was taken.

All the initial activities were also corrected for the abundance of the particular radiation. These abundances and the uncertainties in these abundances were usually taken from [TOI77], except where more recent work turned up significant differences from these values.

When more than one radiation for a given isotope was measured, the decay-curve fitting and the efficiency and abundance corrections were performed as above. A weighted average of the resulting initial decay rates was then taken. In an effort to treat the published uncertainties in the radiation abundances as correctly as possible, in these cases, the relative intensities (and the corresponding uncertainties) for the individual radiations were used, and final adjustment for the absolute abundance (and the uncertainty in this normalization) was made after the weighted average was taken.

3.7 CHEMICAL YIELD CORRECTIONS

The last step in the calculation of the cross sections was the correction for the chemical yields. The chemical yields for the Th through Am fractions were determined by the addition of the following tracers: ^{235}U (^{231}Th), ^{237}Np (^{233}Pa), ^{238}Pu, and ^{241}Am. The activity of these tracers after the chemical separation was compared with with that in an aliquot of the same volume of the tracer solution. Tracers could not be added to most of the other fractions because the tracer activities would have interfered with the determination of the activities produced in the bombardments. Since these activities are produced in the bombardments, often in relatively large yields, the chemical yield determination by the addition of tracer activities would be unreliable unless a large amount of the tracer activities were added. The other chemical yields were determined by normalizing the cross sections for a given isotope of an element whose cross section and chemical yield were also determined in the bombardment where a group separation of the +3 actinides was performed with ^{241}Am and ^{254}Es (^{250}Bk, ^{250}Cf) tracers. Chemical yields which were not determined by either of the above methods were estimated based on the chemical yields of the surrounding elements from the same separation procedure.

SECTION 4 RESULTS

4.1 OVERVIEW OF RESULTS

The results of the experiments and procedures presented in the previous sections are presented here in the form of production cross sections. These cross sections will be presented as a function of the N and Z of the target-like product and also as excitation functions for each of these nuclides. These results will be compared with those from the $^{136}Xe + ^{248}Cm$ system and the prospects for discovery of new isotopes in similar reaction systems will be discussed. Finally, comparisons will be made with other reaction systems.

4.2 PRESENTATION OF CROSS SECTIONS

4.2.1 THE CROSS SECTIONS

The cross sections for the production of actinide products in ^{136}Xe bombardments of ^{249}Cf are presented in table 4.2.1. The identification of the nuclide is given in the first column. If there is more than one isomer of a particular nuclide, the half-life of the isomer of interest is given in the second column. The following nine columns contain the cross sections, three columns for each of the three bombarding energies. For each bombarding energy, the cross section and the uncertainty in the cross section (one standard deviation) appear in two columns and in the third is a comment about the cross section values, when necessary. A dash indicates that the value was not measured. In the comment columns, "UL" indicates that the preceding value is an upper limit for an activity which was not observed (see section 3.3.4). "LL" in the comment columns indicates that the preceding cross section is a lower limit because the absolute intensities of the radiations measured are not known. These lower limits were determined by assuming that the absolute abundance of the most intense radiation observed for this nuclide is 100%. The upper limits given for ^{248}Es were calculated with the assumption that the 550.7 keV gamma-ray [LI 85] has an absolute abundance of 100% and are therefore probably too low.

None of the cross sections presented here have been corrected for feeding by radioactive parent activities during the bombardment and during the time between the end

of the bombardment and the time the chemical separations were performed. By looking at the values of the cross sections and the decay modes and half-lives of all the isotopes in this region, it can be seen that these corrections are not important (accounting for less than 10% of the measured cross section). Feeding during the bombardment is important only for the curium isotopes with masses of 255 or less. Because of the feeding of these isotopes by the alpha decay of the neutron-deficient californium isotopes, these Cm cross sections are not presented in this work.

These cross sections are also presented as a function of mass number for each Z in figures 4.2.1, 4.2.2, and 4.2.3 (748 MeV, 813 MeV, and 876 MeV bombardments respectively). In these figures, the open points refer to nuclides in which only one half of an isomer pair was measured. The lines through the points are are meant only to guide the eye and have no other significance.

Perhaps a better way to visualize the cross sections from these bombardments is a contour plot of the cross sections as a function of Z and A. Such a contour plot appears in figure 4.2.4 for the data from the highest energy bombardment (876 MeV). This plot was constructed by interpolating along smooth curves drawn between the data of figure 4.2.3 for each Z. The contour plots for the lower energy bombardments are very similar to that in figure 4.2.4 except for the much lower overall cross sections for the lowest energy bombardment and a very slight shift toward

more neutron-rich nuclides with decreasing bombarding energy.

4.2.2 CORRECTIONS DUE TO ^{245}Cm IN THE TARGET

The alpha decay daughter of ^{249}Cf is ^{245}Cm. Since the half-life of ^{249}Cf is 350.6 years, there is a small but possibly significant amount of the ^{245}Cm daughter present in the target. The target preparation procedures (section 2.2.1) did not separate Cf from other trivalent actinides. Final separation of the ^{249}Cf from ^{245}Cm and other actinides was made on June 3, 1981 [BIG81]. The fraction of the target material which was ^{245}Cm was calculated to be 0.0044 and 0.0047 for the 876 MeV bombardments, 0.0049 for the 813 MeV bombardments, and 0.0061 for the 748 MeV bombardments. Since the cross sections for below-target products drop off sharply with decreasing Z, it is possible that, for example, a significant fraction of the Am yields is due to a dZ=-1 transfer (with a correspondingly large cross section) from the small ^{245}Cm component in the target as compared to the dZ=-3 transfer (with a small cross section) from the major component (^{249}Cf) of the target.

Table 4.2.2 illustrates the magnitude of this effect for the bombardments contained in this work. In this table, it was assumed that the cross sections for analogous transfers (to form products with the same dZ and dA) are the same from target materials of ^{249}Cf and ^{245}Cm. In first column of table 4.2.2 is the nuclide for which the cross section contribution due to ^{245}Cm in the target is being calculated. The production cross section for this nuclide

from the 813 MeV ^{136}Xe bombardments of ^{249}Cf is given in the second column. The product nuclide of the analogous transfer from ^{249}Cf is in the third column. The fourth column contains the production cross section for the nuclide in column two from a 813 MeV bombardment of ^{249}Cf with ^{136}Xe ions. The fifth column contains the apparent contribution to the cross section listed in column 2 from the ^{245}Cm component in the target (taken to be 0.50%). Finally, the last column contains the fraction of the measured cross section which has been calculated to be due to the ^{245}Cm component in the target (column 4 / column 2).

From this table it can be seen that in all cases (except for ^{245}Am) the cross section contributions from the ^{245}Cm component in the target is less than 15.% of the measured cross section. For the rest of this work these contributions will be ignored. The calculated contribution for ^{245}Am is probably too high due to the measured cross section for ^{249}Bk which, when the trends in the Bk cross sections are compared, also appears to be too high in the 813 MeV bombardment.

4.2.3 EXCITATION FUNCTIONS

As mentioned earlier, these experiments were carried out with ^{136}Xe beams of three energies. These energies, after passing through the target system to the ^{249}Cf target material had energies of 748 MeV, 813 MeV, and 876 MeV, corresponding to 1.00, 1.08, and 1.16 times the Coulomb barrier. The excitation functions for Am and Bk isotopes appear in figure 4.2.5, and those for Cf, Es, and Fm

isotopes appear in figure 4.2.6. It can be seen, from these figures, that the cross sections from the lowest energy bombardments are much lower than the others, and that a maximum in the production cross sections was reached between the two highest bombarding energies, and the cross sections are, in general, dropping off at the highest energy. The curves in figures 4.2.5 and 4.2.6 are drawn through the points as plotted at the centroid of the energy distribution for the respective bombardment. Since, especially in the lowest energy bombardment, the cross section is not constant over the energy interval, to plot a more accurate representation of the cross section for a monoenergetic bombardment, the points would have to be plotted at some corrected energy value. For example, when weighting an exponential approximation to the cross section vs. energy curve between the lowest two energies by the energy distribution given by equation 2.4.1, it is found that the low energy ends of the curves in figures 4.2.5 and 4.2.6 should cross through a point about 12 MeV higher than the centroid of the energy distribution for the lowest energy points. This energy weighting procedure is illustrated in figure 4.2.7.

Looking at the excitation functions in more detail, the cross sections for larger transfers tend to have a stronger energy dependence. The Fm ($\Delta Z=+2$) cross sections are dropping off at the highest energy much more than are the Es ($\Delta Z=+1$) cross sections. A similar result can be seen in the below-target excitation functions, where the Am ($\Delta Z=-3$)

cross sections are dropping off faster than are the Bk ($\Delta Z = -1$) cross sections at the highest energy. It is expected that in damped collisions, the amount of kinetic energy damping is at least roughly correlated with the number of nucleons (or protons) transferred. This would cause the excitation energy, and therefore, the prompt fission of the products from larger transfers to be more sensitive to the bombarding energy than those from smaller transfers. This energy dependence may also be due to the larger contribution from direct transfer reactions (with a small kinetic energy damping) for small transfers. A larger fraction of the large transfers are produced in deep inelastic reactions which have a large amount of kinetic energy damping. The reactions with less energy damping (small transfers from direct interactions) will form products with lower excitation energies, and therefore, the prompt fission of these products will be less dependent on the bombarding energy.

Another feature evident from the excitation functions is that the actinide products which survive prompt fission from higher energy bombardments are in general slightly more neutron-deficient those from lower energy bombardments. In figures 4.3.1 and 4.3.2 it can be seen that the cross sections for the most neutron-rich nuclides of each element tend to drop off with increasing energy more quickly than do the cross sections for the less neutron-rich nuclides. This indicates that, in the nuclides which survived prompt fission, the average number of neutrons evaporated during

the deexcitation of the initial products is higher in the highest energy bombardments, which, in turn, indicates a higher average initial excitation energy.

4.3 COMPARISON WITH THE ^{136}Xe + ^{248}Cm SYSTEM

4.3.1 THE ^{136}Xe + ^{248}Cm CROSS SECTIONS

One of the main motivations for studying the ^{136}Xe + ^{249}Cf system was to compare the resulting cross section distributions with those from the ^{136}Xe + ^{248}Cm system [MOOS3]. A contour plot of the production cross section distribution from ^{136}Xe + ^{248}Cm at a bombarding energy of 1.02 times the Coulomb barrier is presented in figure 4.3.1. One of the features of interest in the comparison of this plot with the similar plot from ^{136}Xe + ^{249}Cf (figure 4.2.4) is the effect the position of the target with respect to beta stability has on the cross section distribution. since ^{249}Cf is on the neutron-deficient side of the line of beta stability and ^{248}Cm is on the neutron-rich side of beta stability, some differences in the cross section distributions are expected because of the beta stability energetics. As expected, the cross sections for transfer reactions to the neutron-deficient side of the target are higher from the ^{248}Cm target than are the cross sections for the analogous transfers from the ^{249}Cf target. Also, as expected, the opposite relation seems to be true in the comparison of the neutron-rich sides of the two cross section distributions. These effects will be made more quantitative in the section on potential energy surfaces (section 5.3).

4.3.2 ABOVE-TARGET DIFFERENCES

A very striking difference between the two contour plots is the much lower yields of neutron-deficient above-

target nuclides from the $^{136}Xe + ^{249}Cf$ reaction when compared with the yields of the analogous products from the $^{136}Xe + ^{248}Cm$ reaction. A possible reason for this difference is that the Γ_n/Γ_f values for the neutron-deficient isotopes of Fm and Md are smaller than those for the analogous products from the $^{136}Xe + ^{248}Cm$ reaction. This is due mainly to the higher neutron binding energies in the more neutron-deficient isotopes. These lowered Γ_n/Γ_f values would cause more of the neutron-deficient above-target products from Cf bombardments to fission during deexcitation than from the ^{248}Cm target. Another possible explanation for the reduced above-target neutron-deficient yields is that from the ^{249}Cf target, these products are particularly high up the neutron-deficient side of the valley of beta stability compared to the analogous products from the ^{248}Cm target. This difference in the beta stability energy would tend to hinder the production of the neutron-deficient above-target yields and enhance the neutron-rich above-target yields from the ^{249}Cf target compared to the analogous yields from the ^{248}Cm target. Again, these effects will be discussed in a more quantitative manner in section 5.

4.3.3 BELOW-TARGET CROSS SECTIONS AND PROSPECTS FOR NEW ISOTOPE PRODUCTION

As can be seen in figure 4.3.1, since the ^{248}Cm target lies on the neutron-rich edge of the known isotopes, few of the neutron-rich below-target cross sections could be measured because they are unknown isotopes with (presumably)

short half-lives and are therefore not detectable with the chemical techniques used in this type of work. Another motivation for the study of the ^{136}Xe + ^{249}Cf reaction system was to measure these neutron-rich below-target yields. Except for the Cm (ΔZ=-2) isotopes, the below-target nuclides are well suited for detection with the experimental techniques described in section 2. In figure 4.2.4 the neutron-rich below-target cross section is fairly complete.

In all but a few cases, the prospects for producing new neutron-rich above-target isotopes with heavy ion transfer reactions are not good (except possibly when using very exotic targets such as ^{250}Cm or ^{254}Es) [GHI84]. It should be possible, however, using less exotic targets, to produce new below-target neutron-rich isotopes. Looking again at figure 4.2.4 and making the crude assumption that the yields for analogous transfers from any actinide target will be the same as those from the ^{249}Cf target, it appears that if a more neutron-rich target was used, some neutron-rich below-target transfers would result in new isotopes in yields large enough for detection. For example, if a ^{248}Cm target were used, the cross sections for the production of ^{248}Am and ^{247}Pu should be about 300 and 30 microbarns, respectively. If the half-lives of these isotopes are at least on the order of one minute, these isotopes could be detected with fast on-line chemistry and related detection systems. This type of experiment has been performed with the ^{136}Xe + ^{244}Pu reaction and it appears that the two new

isotopes, ^{243}Np and ^{244}Np have been identified [MOO85].

4.3.4 COMPARISON WITH OTHER SYSTEMS

Further insights into the reaction mechanisms involved in heavy ions transfer mechanisms can be gained by comparing the ^{136}Xe + ^{249}Cf cross section distributions with those of other reaction systems. Of particular interest is the comparison with the light heavy ion systems such as $^{16,18}O$ and $^{20,22}Ne$ projectiles interacting with targets of ^{248}Cm, ^{249}Bk, ^{249}Cf, and ^{254}Es [LEE82] [LEE83] [SCH82] [SCH84]. In these systems, for a single projectile, it has been found that for a given transfer (with a given ΔZ and ΔN) the cross sections are essentially independent of the identity of the target. This indicates that there is less equilibration of energy and nucleons during the transfer process with light-heavy ions than there is with the very heavy ions such as ^{136}Xe.

The cross section distributions from the ^{136}Xe + ^{249}Cf reaction can also be compared with the cross section distributions from other very heavy ion reactions. Of interest are the interactions of actinide targets with the heaviest ions available. These distributions are available from the ^{238}U + ^{238}U reaction and from the ^{238}U + ^{248}Cm reaction [SCH78] [MSC82] [GAG81]. As is the case with the ^{136}Xe + ^{248}Cm reaction, the targets used in these reactions were the most neutron-rich isotopes of U and Cm available. For this reason, the cross section distributions will compare with the distributions from this work in much the same way as the ^{136}Xe + ^{248}Cm cross section distributions

did (with some minor differences due to the identity of the projectile).

SECTION 5 MODELING

5.1 OVERVIEW OF MODELING

This section contains the presentation of a simple model for a theoretical determination of the cross section distributions from heavy ion bombardments of actinide targets. It assumes a binary reaction mechanism (two particles in the entrance and exit channels). When the projectile and the target collide, they remain in contact, as a dinuclear complex, for a time on the order of the nuclear transit time (several times 10^{-23} seconds) and exchange nucleons, energy, and angular momentum. The exchange of angular momentum will be ignored in this model and the effects of this omission will be noted in the following sections. It has been found that while the target and projectile are in contact that the charge (or mass) distribution between the target-like fragment and the projectile-like fragment equilibrates relatively slowly, with a relaxation time on the order of 60×10^{-23}s. It has also been found that equilibration of the N/Z distribution and the kinetic energy damping happen relatively quickly, with relaxation times of about 1.2×10^{-23}s and 3×10^{-23}s respectively [MOR80]. In this model, it will be assumed that the charge distribution is totally unequilibrated and it will be described by an empirical procedure outlined in section 5.2. It is also assumed that all of the kinetic energy loss appears as excitation energy in the dinuclear complex and eventually in the separated target-like and projectile-like fragments. This excitation energy of the

dinuclear complex is treated as if it were totally equilibrated between the two participants. This is reasonable in the light of the fact that the kinetic energy damping is relatively fast and the equilibration of the resulting excitation energy should be even faster. A final major assumption is that the N/Z distribution in the dinuclear complex is totally equilibrated. In this model, the N/Z equilibration is treated as if it occurred via the transfer of neutrons between both parts of the dinuclear complex [LUC83]. This method of N/Z equilibration is reasonable in the light of the fact that while the two participants are remaining near the interaction radius, there is still a Coulomb barrier to inhibit the transfer of protons while no such barrier exists toward the transfer of neutrons. Some recent results of the study of the equilibration of the N/Z ratio suggest that the equilibration of the N/Z ratio occurs at approximately constant mass, rather than by the exchange of neutrons. This N/Z equilibration is assumed to occur by anticorrelated proton and neutron flow or by some other form of isospin transfer without the transfer of nucleons [GRO81]. Equilibrating the N/Z ratio by transfer of isospin at constant mass would increase the calculational complexity in this model by several times, so the N/Z ratio was assumed to equilibrate by neutron exchange only. It can be shown that different isotopic distributions will result from equilibration by exchanging neutrons at a fixed Z distribution when compared to equilibrating by isospin

transfer subject to the restriction of a final $d\sigma/dZ$ distribution, but it is expected that these differences are small.

An empirical description of the $d^2\sigma/dZdE$ distribution is used as the starting point for this model, where E is the kinetic energy of the target-like and projectile-like products in the exit channel in the center of mass frame of reference. For each Z the neutrons and excitation energy are distributed between the two participants in the dinuclear complex by a statistical procedure based on the calculated level densities of the dinuclear complex. This yields a triple differential cross section distribution, $d^3\sigma/dZdNdE^*$, where E^* is the excitation energy of the target-like fragment. This distribution is then deexcited by neutron emission and fission using a simple Γ_n/Γ_f theory to give a final $d^2\sigma/dZdN$ distribution. This final distribution will be presented and the differences between this calculated distribution and the experimental distribution will be discussed. Finally, some possible improvements to the model will be discussed. It should be noted that this model treats only the damped collisions and ignores the products formed by quasi-elastic transfers.

5.2 CHARGE AND ENERGY DISTRIBUTION

As mentioned above, in this model, the charge distribution is assumed to be essentially unequilibrated since the relaxation time for this mode is large compared with the reaction time. Because of this, an empirical description of the $d^2\sigma/dZdE$ distribution is used. It is assumed that at some time time during the interaction, the charge distribution takes on the features as described by H. J. Wollersheim [WOL84]. It is then assumed that the neutron and excitation energy distributions subsequently equilibrate around this charge distribution.

The $d^2\sigma/dZdE$ distribution is given in [WOL84] as a Gaussian function

$$\frac{d^2\sigma}{dZdE} = N(E)\exp\left[\frac{-(Z - Z_0)^2}{2\sigma_Z^2(E)}\right] \qquad (5.2.1$$

where the Gaussian width is given by

$$\sigma_Z^2(E) = \exp\left[-6.07\ \frac{(E - E_0)}{l_g}\right] \qquad (5.2.2$$

where l_g is the grazing angular momentum (calculated for products which will recoil at the quarter point angle [WIL80]). Z_0 is the centroid of the Z distribution of the target-like fragments (taken to be one unit less than the target Z as done in [WOL84]), and E_0 is the incident energy in the center of mass system. The normalization factor N(E) is empirically given by the relation

$$N(E) = a\left(E - V_C^{DEF}\right) \qquad (5.2.3$$

where a is given in units of fm^2 by

$$a = 0.00324\left(\frac{R_{INT}^2}{E_0} - 0.190\right) \qquad (5.2.4$$

The deformed Coulomb barrier V_C^{def} can be calculated by integrating equation 5.2.2 over all Z and over E from the deformed Coulomb barrier V_C^{def} to the incident energy E_0 and setting this equal to the total classical geometric cross section. V_C^{def} was found to be 362 MeV for the 876 MeV $^{136}XE + ^{249}Cf$ system.

A plot of $d\sigma/dZ$ for various values of E between V_C^{def} and E_0 is presented in figure 5.2.1. As expected, at lower separation energies (higher energy damping) the cross section distributions become wider. The distributions for the collisions with only a small amount of energy damping (presumably more peripheral collisions with a shorter interaction time and less overlap of the two nuclei) have a much narrower Z distribution.

This empirical description for the $d^2\sigma/dZdE$ distribution for heavy ion transfer reactions was developed using data from several bombardments with projectiles ranging from Kr to Sm on targets ranging from Sm to Bi. Especially since the landmark reaction used by Wollersheim is the $^{136}Xe + ^{209}Bi$ system it seems logical to assume that the extrapolation to the $^{136}Xe + ^{249}Cf$ system will give

reasonable results.

5.3 POTENTIAL ENERGY SURFACES

5.3.1 DESCRIPTION OF POTENTIAL ENERGY SURFACES

After the determination of the $d^2\sigma/dZdE$ distribution, the next step is to distribute the neutrons and the excitation energy within the dinuclear complex between the two participants. It is assumed that all of the kinetic energy loss appears as excitation energy, but there is another source of excitation energy. This other source of excitation energy can be most easily described in terms of a potential energy surface similar to those used in [WEL85] and [GAG85]. This potential energy surface determines the potential energy of a dinuclear complex reaction intermediate consisting of two spheroidal nuclei at some separation distance associated with the various possible combinations of Z and N in the exit channel of a binary reaction. The zero point in energy of such a surface is taken to be the energy of the reaction which would result in no change in the identities of the target and projectile during the interaction.

The typical potential surface is calculated with energies which arise from four different sources. The first and most important of these energies is the additive inverse of the ground state to ground state Q value for the binary reaction (Q_{gg}) which is determined by subtracting the masses of the products in the exit channel from the sum of the masses of the target and projectile. In this work, the masses were calculated according to the droplet model of Myers and Swiatecki [MYE80] [MYE77]. The odd even effect in

the mass formula was left out because in the dinuclear system there is usually an excitation energy of several MeV and it is, therefore, not expected that the nucleons near the Fermi surface are paired. Also because of the high excitation energy, and the tendency it has to break up the pairing, the effect of the Wigner term should be reduced, but this is a minor effect and will be ignored in the rest of this presentation. The excitation energy in the dinuclear complex also causes problems with the use of the shell effects and the ground state deformation energies because they are also expected to reduce with increasing excitation energy. These effects will be discussed further in sections 5.3.2 and 5.4.

The other major term in the calculation of these potential energy surfaces is the Coulomb separation energy. this is determined by subtracting the Coulomb energy of the product nuclei from the Coulomb energy of the target and the projectile calculated at some minimum radius, which in this work was taken to be the interaction radius of the target and projectile [WIL80]. This Coulomb separation energy was used in the potential energy surfaces presented in section 5.3.2, but was not used in the calculation of the excitation energy of the dinuclear complex because this effect is already included in the $d^2\sigma/dZdE$ distribution described above in section 5.2. It should be noted that in the potential energy surfaces which use this Coulomb separation energy, this separation energy is only an approximation because the final products are actually separating with

energies anywhere from the incident energy to the deformed Coulomb barrier.

The third term in the potential energy surface calculation is the nuclear potential energy term. This is determined by a proximity potential [BLO76]. This is a minor effect because the curvatures of the nuclear surfaces change very little during the exchange of several nucleons and because, in the calculation, the interaction radius is being held constant at the value associated with the entrance channel products. This term is used in the calculation of the excitation energy of the dinuclear complex which is in turn used in the distribution of the excitation energy and the neutrons. It should, however, be subtracted in some way from the excitation energy of the separated fragments in the exit channel before the deexcitation calculation because the proximity potential between the separated fragments is zero.

The last term in the potential energy calculation is a centrifugal potential term. This term has only a minor effect on the potential energy surface. In order to avoid the complexity of describing the potential energy surface along a third coordinate (ℓ as well as Z and N), the centrifugal term was taken to be zero which corresponds to central collisions between the target and projectile.

5.3.2 THE POTENTIAL ENERGY SURFACE AND SHELL EFFECTS

The potential energy surface for 870 MeV (lab frame) ^{136}Xe ions bombarding a ^{249}Cf target is given in figure 5.3.1. In this plot the contours are of the potential

energy as calculated in section 5.3.1 as a function of the Z and N of the target-like fragment in the exit channel. In this surface, the shell effects and ground state deformation energies were included in the masses. The odd-even term in the masses was left out to give a smooth surface. The injection point (^{249}Cf) can be seen to be near a local minimum in the surface. A discernible kink in the surface can be seen in the surface at 151 neutrons. This is due to the strong shell effects due to the N=82 shell in the projectile-like fragment. A saddle point appears at ^{239}Np and the surface is headed toward a second minimum at the doubly magic ^{208}Pb.

Figure 5.3.2 contains the same potential energy surface as in figure 5.3.1 with the shell effects and the ground state deformation energies removed. The saddle point has totally disappeared and the whole surface has shifted slightly toward higher neutron numbers. It is apparent that the shell effects in the projectile-like fragment are strong enough to change even the most general features of the potential energy surface. Since these shell effects should disappear at some intermediate excitation energy, some combination of these surfaces should be used to describe the distributions from these binary heavy ion collisions. The combination of these surfaces used in this work will be described in section 5.4.

5.4 DISTRIBUTION OF NEUTRONS AND EXCITATION ENERGY

5.4.1 EXCITATION ENERGY OF THE DINUCLEAR COMPLEX

Starting with the $d^2\sigma/dZdE$ distribution calculated in section 5.2, it is now necessary to calculate the triple differential distribution $d^3\sigma/dZdNdE^*$ where E^* is the excitation energy of the target-like fragment after separation from the dinuclear complex. This will be accomplished separately for each Z of the $d^2\sigma/dZdE$ distribution. For each Z and E in the distribution, the level density of the dinuclear complex for every possible distribution of neutrons and excitation energy between the two participants must be calculated. The first step in this calculation is to determine the excitation energy of the dinuclear complex as a function of the Z and N of the target-like fragment and E of the reaction. For a given Z, the excitation energy of the dinuclear complex is taken to be the sum of the kinetic energy loss, E_0-E, less the value of the potential energy surface (with the Coulomb separation energy subtracted off) at each possible value of N. In order to preserve the total reaction cross section, when this excitation energy was calculated to be negative, it was set at zero, but this should be only a small fraction of the total reaction cross section. In order to account for the damping of the shell effects in an approximate way, the shell effects were made to decrease linearly with increasing excitation energy of the dinuclear complex, starting at their full value at an excitation energy of zero and decreasing linearly up to dinuclear complex excitation

energy of some preset value. The best fits to the experimental cross sections were obtained when this energy for the full damping of shell effects was set at about 40 MeV, which is consistent with the measurements of the damping of shell effects with excitation energy in compound nucleus reactions [VER84] [KSC82].

5.4.2 DINUCLEAR COMPLEX LEVEL DENSITIES

The level density of the dinuclear complex is calculated as the product of the level densities of each of the fragments where the level density of each of the fragments is given by the simple Fermi gas level density formula

$$\rho(E) \propto \exp\left[2(aE^*)^{1/2}\right] \qquad (5.4.1$$

where the fermi gas constant is given by [SEG77].

$$a = \frac{A}{8} \qquad (5.4.2$$

For each value of the energy damping in the dinuclear complex, E, the neutron numbers of the target-like fragment, N_{TLF} and the projectile-like fragment, N_{PLF}, are varied over all reasonable combinations subject to the restriction that the total number of neutrons remains constant at the number of neutrons in the entrance channel. For each value of N_{TLF}, the excitation energy of the dinuclear complex is calculated as above and this excitation energy is distributed among the two fragments in the dinuclear complex

in discrete steps covering all possible combinations subject to the restriction that $E^*=E^*_{TLF}+E^*_{PLF}$; where E^*_{TLF} and E^*_{PLF} are the excitation energy of the target-like fragment and of the projectile-like fragment respectively. The level density of the dinuclear complex can be written as

$$\rho_{DNC}(E) \quad \alpha \quad \exp\left[2(a_{TLF}E^*_{TLF})^{1/2}\right] \quad \exp\left[2(a_{PLF}E^*_{PLF})^{1/2}\right] \qquad (5.4.3$$

5.4.3 CALCULATION OF THE $d^3\sigma/dZdNdE^*$ DISTRIBUTION

The distribution of E^*_{TLF}, E^*_{PLF}, and N_{TLF}, and N_{PLF} were assumed to be proportional to the level densities associated with each possible distribution. For each Z and E the level densities were calculated for every combination of E^*_{TLF}, E^*_{PLF}, N_{TLF}, and N_{PLF} and these level densities were changed to cross section distribution contributions by normalizing by the magnitude of the $d^2\sigma/dZdE$ distribution at the appropriate Z and E. These normalized cross section contributions are then added to a large three dimensional matrix containing the triple differential distribution $d^3\sigma/dZ_{TLF}dN_{TLF}dE^*_{TLF}$, which is the calculated initial distribution of target-like fragments before deexcitation. A contour plot of this initial distribution summed over all excitation energies is presented in figure 5.4.1. The shell effects were made to damp out completely by 40 MeV for the calculation depicted in figure 5.4.1.

A $d^3\sigma/dZ_{TLF}dN_{TLF}dE^*_{TLF}$ distribution was also calculated using the more complicated level density formalism of Gilbert and Cameron [GIL65]. This level density calculation

includes pairing effects and shell effects on the level density. It was found, however, that these shell effects were too strong especially at higher excitation energies where they are expected to weaken. The initial distribution calculated with these level densities showed strong minima at N=82 in the projectile-like fragment which are not at all consistent with the experimental results.

5.5 DEEXCITATION OF THE INITIAL DISTRIBUTION

5.5.1 MODES OF DEEXCITATION

The initial distribution of target-like fragments with respect to proton number, neutron number and excitation energy has been calculated in section 5.4. In order to reach the final cross section distribution, it is necessary to remove the excitation energy from the initial distribution. In this model it was assumed that the deexcitation occurs by only neutron emission in competition with fission. Deexcitation by emission of charged particles is ignored here because it will skew the distribution of products with respect to Z and because the emission of charged particles is expected to be unimportant relative to the emission of neutrons except in the most neutron deficient isotopes.

To perform the deexcitation, each element of the $d^3\sigma/dZdNdE^*_{TLF}$ distribution (starting with the highest E^*)was allowed to "fission". This was accomplished by multiplying the element of the distribution by the appropriate $(\Gamma_n/\Gamma_f)/(\Gamma_n/\Gamma_f+1)$ to obtain the amount of that element surviving fission at this step in the deexcitation. A neutron was then "evaporated" from this distribution. This was accomplished by distributing the contents of this element among those elements with one fewer neutron and with excitation energies corresponding to the energy of the element being deexcited less the binding of the last neutron and a Boltzmann energy distribution [HAR62]. This procedure was repeated for all elements in the initial distribution.

If at any point in the deexcitation process, the excitation energy was less than both the fission threshold and the neutron binding energy, the contents of the array element was assumed to decay the rest of the way to the ground state by gamma emission, and the contents of that array element were put into the array element with the same Z and N with zero excitation energy. If the excitation energy was less than the neutron binding energy and greater than the fission threshold, all the contents of that array element were assumed to decay by fission and were not treated further in the deexcitation process. If the excitation energy was higher than the neutron bonding energy and less than the fission threshold, the "fission" step was skipped and the neutron emission was carried out as above [VAN58].

5.5.2 CALCULATION OF NEUTRON BINDING ENERGIES AND FISSION THRESHOLDS

In order to perform the above calculations it was necessary to calculate the neutron binding energies and fission thresholds for the actinide elements. The neutron binding energies are used in the calculation of the Γ_n/Γ_f values and in determining the energies of the evaporated neutrons. The fission thresholds are also used in the calculation of Γ_n/Γ_f values. Calculated rather than experimental values were used in this work because it was important to have a set of values which was consistent for all nuclides considered whether they are known nuclides or not.

The neutron binding energies were calculated by

subtracting the appropriate droplet model masses [MYE80]. The neutron binding energies used at high excitation energies (>30 MeV) contained neither the shell effect nor the odd-even corrections to the masses energy. This is appropriate for the nuclides at high excitation energies because these are effects which depend on the nucleons near the Fermi surface being in their ground states, which is not the case at high excitation energies. Below 30 MeV the neutron binding energies with shell and odd-even effects were used.

The fission thresholds used in this work also came from [MYE80]. They are obtained by subtracting an experimental ground state shell correction from a calculated saddle point energy. Since there are some problems with this mass formula in predicting the actinide masses, there is sometimes a discontinuity in the fission barriers when crossing from known nuclides with experimental ground state shell corrections to unknown nuclei with calculated ground state shell corrections. These discontinuities in the fission barriers were considered not important in this work, because they happen at nuclides which are on the wings of the cross section distributions and have little effect on the main part of the distribution.

5.5.3 Γ_n/Γ_f CALCULATIONS

The Γ_n/Γ_f values used in the deexcitation procedure were calculated based on the treatment by Vandenbosch [RVA58]. A calculation of Γ_n/Γ_f values gives the theoretical estimate of

$$\Gamma_n / \Gamma_f = \frac{TA^{2/3}}{10} \exp\left[(E_f - B_n)/T\right] \qquad (5.5.1$$

where T is the nuclear temperature and E_f and B_n are the fission threshold and the neutron binding energy, respectively. The authors in [VAN80] make an argument for the following formula for the calculation of Γ_n/Γ_f.

$$\Gamma_n / \Gamma_f = 3.5\exp\left[(E_f' - B_n')/T\right] \qquad (5.5.2$$

Where T is taken to be 0.6 MeV and E_f' and B_n' are the fission threshold and the neutron binding energy which have been corrected for the effects that the odd nucleons have on the level densities at the fission barrier and at the neutron binding energies. Again, these odd-even effects should only be applicable at relatively low excitation energies (Γ_n/Γ_f measurements are usually only available up to excitation energies of about 20 Mev). In this work, for excitation energies below 30 MeV, equation 5.5.2 was used for the Γ_n/Γ_f values with the odd-even energies included in the neutron binding energies. For excitation energies above 30 MeV, the odd-even effects and the shell effects were removed from the neutron binding energies and the corrections for the level densities at the neutron binding energy and at the fission threshold were also removed.

5.6 RESULTS OF THE MODELING CALCULATIONS

The calculated cross section distributions for the target-like fragments from 870 MeV ^{136}Xe + ^{249}Cf reaction are presented in figure 5.6.1 as a series of production cross section vs. N curves for each Z. The closed neutron shell at N = 82 in the projectile (N = 151 in the target-like fragment) has a very striking effect on the calculated cross section distributions. All of the curves drop off rapidly at neutron numbers above N=151. This may suggest that a neutron-rich projectile with a neutron number away from a closed shell may be preferable for the production of neutron-rich target-like fragments. It is also interesting to note the minimum in the elemental cross sections at Z=92. When these elemental cross sections are compared with the elemental cross sections in the initial distribution (see figure 5.4.1) it can be inferred that the increase in the cross sections in the final distribution for elements with Z<91 is due to the increased fission barriers in these elements. A similar trend has been measured experimentally for the lightest target-like fragments from the ^{48}Ca + ^{248}Cm reaction [GAG85]. A contour plot of the production cross sections in this final distribution is presented in figure 5.6.2.

Some of the results from the calculation as described above are plotted in figure 5.6.3 along with the experimental data from the ^{136}Xe + ^{249}Cf reaction at the highest bombarding energy. The circles indicate the experimental cross sections with the open points being the

cross section for when only half of an isomer pair was measured. The calculated cross sections are indicated by the squares. Only the highest bombarding energy was modeled because the $d^2\sigma/dZdE$ distribution is only accurate for energies well above the Coulomb barrier [WOL84]. This calculation was performed with the shell effects damping out totally when the excitation energy of the dinuclear complex reaches 40 MeV.

The calculated near target cross sections (Es and Bk $\Delta Z=+1,-1$) reproduce the experimental data fairly well. The centroids of the calculated cross section distributions for these elements are correct and the calculated widths of the distributions are close to the experimental widths. The fits to the experimental data for the Fm and Am ($\Delta Z=+2$ and $\Delta Z=-3$) are not as good. The widths of the calculated cross section distributions are too wide. The centroid of the calculated Fm distribution is correct, but the centroid of the calculated Am distribution is about 2 mass units too low.

The low-mass tail in the calculated Am distribution could be due to the neglect of the angular momentum effects in the deexcitation calculation. It is expected that there is a large angular momentum transfer in the $\Delta Z=-3$ reactions which would lead to Am isotopes at relatively high excitation energies. Deexcitation by neutron emission occurs mainly by emission of s-wave neutrons, so the angular momentum of the Am products are not reduced much by neutron emission. Eventually, during the deexcitation process,

these nuclides will reach the yrast band where emission of s-wave neutrons is impossible, and deexcitation must proceed by the slow emission of gamma-rays. If this is the case, it is expected that many of the highly excited Am isotopes will fission instead of deexciting by gamma emission along along the yrast band. Another possible explanation for the wider calculated cross section distributions for these larger transfers is that the equilibration of neutrons within the dinuclear complex is not complete as is postulated in the model.

Looking at the cross section distributions for the elements even further from the target Z, it can be seen that the calculated cross section distributions become even wider. The predicted Md cross sections appear to be an order of magnitude too high and the predicted Np cross sections appear to be too low by almost an order of magnitude. Making further comparisons for these elements is difficult because of the incompleteness of the experimental cross section distributions.

Even with this rough calculation, much has been learned about the role of shell effects in these damped transfer reactions. The calculation was also run with the shell effects in the ground state massed omitted. This resulted in significantly wider cross section distributions for each element and the centroids shifted away from N=151 (82 neutrons in the projectile-like fragment). When the shell effects were included in such a way that they did not decrease in magnitude with increasing excitation energy of

the dinuclear complex, the cross section distributions for each element seen to shift even more strongly toward N=151.

It appears that this calculation does a fair job of recreating the cross section distributions for these damped transfer reactions. This may show that our understanding of these reaction mechanisms is essentially correct. It appears, however, that this model is not accurate enough for the prediction of the cross sections for the products of the transfer of a large number of nucleons. Modifications to the model which may enhance the accuracy of the calculation are discussed in the next section.

5.7 POSSIBLE IMPROVEMENTS TO THE MODEL

The calculations outlined in section 5 are only rough calculations and are meant as a demonstration of the theoretical technique. There are several improvements to the model which may make the comparison between the experimental and calculated cross sections better. Some of these improvements are outlined in the following paragraphs.

It seems that it would be better to equilibrate the N/Z ratio in the dinuclear complex by exchanging isospin among the fragments rather than exchanging neutrons. It is theoretically possible to perform an isospin equilibration subject to the restriction of a final $d\sigma/dZ$ distribution, but this is mathematically very complex and there are some more practical problems that may even make the calculation impossible. One way of simplifying the calculation would be to start with a $d^2\sigma/dAdE$ distribution rather than a $d^2\sigma/dZdE$ distribution. This would allow the simple equilibration of the N/Z ratio at constant mass by equilibrating the isospin. At this time, however there are no descriptions of the $d^2\sigma/dZdA$ distribution available for this type of reaction mechanism.

It is also possible to use a better set of masses when calculating the Q_{gg} values to be used in the potential energy surface and in the calculation of the excitation energy used in the distribution of the neutrons and the excitation energy between the two participants in the dinuclear complex. The values used in this work did not correctly predict the position of the valley of beta

stability in the actinide region. A set of masses for the actinides which was optimized for that region would be preferable.

In this model, the simplest form of the nuclear level densities were used in the calculation of the level density of the dinuclear complex for the distribution of neutrons and excitation energy. When a more complex form of the nuclear level density was used [GIL65], which accounted for shell effects and odd even effects, unreasonable results were obtained. These unreasonable results were due to the fact that the shell effects in this level density formalism were in some way too strong. There are other formalisms for including shell effects in the nuclear level density such as that contained in [KSC82] and [VER84]. This model should be tested using one of these level density formalisms which has shell effects that disappear at higher excitation energies.

The last major change to be suggested here is the improvement of the deexcitation calculation. The deexcitation method used in this model is a simple Γ_n/Γ_f calculation which does not account for the angular momentum of the deexciting nucleus. Accounting for the angular momentum will in some cases greatly reduce the Γ_n/Γ_f values and cause more of the target-like products to fission during the deexcitation. Including the angular momentum in the model would also change the shape of the potential energy surface slightly, and therefore change the initial distribution which is the result of the equilibration of the neutrons and the excitation energy in the dinuclear complex.

The main problem in including the angular momentum in the calculation is that it would greatly increase the calculational complexity. for example, the three dimensional initial distribution, $d^3\sigma/dZdNdE^*$, would become a four dimensional distribution, $d^4\sigma/dZdNdE^*d\ell$, where ℓ is the angular momentum of the target-like fragment. A simpler modification to the deexcitation calculation is to use a better set of fission barriers in the calculation of the Γ_n/Γ_f values. Such a set exists for part of the actinide region [HOW80] in which the fission barriers were calculated for a combination of deformation coordinates rather than the single coordinate fission barriers used in this work.

SECTION 6 CONCLUSION

The actinide production cross sections have been measured for the reaction of ^{136}Xe + ^{249}Cf at energies from the Coulomb barrier to 1.16 times the Coulomb barrier. The cross section distribution for the actinide products appears similar to those from other heavy ion reactions with actinide targets. A major difference between the distribution from this reaction and the cross section distribution from the ^{136}Xe + ^{248}Cm reaction is the lower cross sections for the $\Delta Z \geq +2$ nuclides from the ^{249}Cf target. The cross sections for below-target neutron-rich products have been measured for the first time in a reaction between an actinide target and a very heavy ion projectile. These below-target neutron-rich cross sections look favorable for the production of new neutron-rich isotopes from reactions such as ^{136}Xe + ^{248}Cm and ^{136}Xe + ^{244}Pu.

It has been found that the excitation functions of most of the actinide products peak between the two highest energies used in this work (1.09 and 1.16 times the Coulomb barrier). Previous investigations using projectiles of Xe or heavier projectiles did not directly measure these excitation functions, either because they used thick targets [MSC82] [GAG81] [SCH78] or because (in experiments at the SuperHILAC) the beam energy was limited to energies very near the Coulomb barrier because of the limitations of the machine and the thicker target backing materials used [MOO83] [WEL85].

In order to help understand the effect of the position

of the target nuclide with respect to beta stability and to understand the deep inelastic reactions in general, a modeling procedure was developed. In this model, the initial charge and kinetic energy loss distribution is given by the empirical formalism of [WOL84]. The distribution of neutrons and excitation energy between the two fragments while in the dinuclear complex is assumed to be totally equilibrated and is calculated by means of the Fermi gas level densities of the dinuclear complex. The resulting initial distribution of target-like fragments is deexcited by neutron emission in competition with fission to give a final actinide cross section distribution. From this model it has been found that:

1) The shell effects in the ground state masses of the target-like and projectile-like fragments are important. These shell effects in the dinuclear complex tend to die out at an excitation energy of the dinuclear complex of about 40 MeV.

2) The neutron distributions of the elements more than 2 Z units from the target are not fully equilibrated.

OR

The lowering of the Γ_n/Γ_f by the deexcitation along the yrast band of nuclides with a high angular momentum is important (the angular momentum of the actinide products was not considered in this model).

3) Our understanding of the mechanism of these damped collisions, as described in this model, is approximately correct but is not accurate enough to

predict the cross sections for the transfer of a large number of nucleons.

APPENDIX A CORRECTIONS FOR NON-LINEAR DECAY DURING THE COUNTING INTERVAL

A.1 DEFINITION OF THE PROBLEM

Radioactive decay curves are usually measured by collecting counts in a detector over a series of intervals. Most often, when fitting these curves, the average count rate for each interval is assumed to occur at the time of the center of the interval. When the counting interval is a sizeable fraction of the half-life of (one of) the nuclide(s) of interest, this assumption can lead to appreciable error. Figure A1 shows a schematic of a single counting interval with appreciable non-linearity in the decay rate during the interval. t_i is the time of the start of interval i, and c_i is the length of this interval. The heavy curve represents the actual decay rate, which is appreciably non-linear, between t_i and $t_i + c_i$. When the average decay rate during the interval, denoted by the shaded area, is plotted at the center of the interval, it appears at point A. The actual activity at this time should, however, be at point B. The average activity actually occurs at some other time to as shown by point C. The method for correction of this discrepancy used in this work is to take the measured average count rate during this interval and multiply it by some correction factor based only on the parameters of the decay curve itself and the times associated with the interval to calculate the decay rate at the beginning of the interval, t_i. This corrected activity is denoted in the figure by the point D.

A.2 DERIVATION METHOD FOR THE CORRECTION FACTORS

The correction factor for a single component decay curve can be derived in a straight forward manner. The decay curve itself is given by

$$A(t) = A_0 e^{-\lambda t} \qquad \text{(A1}$$

where A(t) is the activity at time t, A_0 is the activity at time t=0, and λ is the decay constant for the activity in question. When measuring over an interval i from t_i to t_i+c_i the average activity, $\overline{A_i}$, can be expressed as follows:

$$\overline{A}_i = \frac{A_0}{c_i} \int_{t_i}^{t_i+c_i} e^{-\lambda t} dt = \frac{A_i}{c_i} \int_0^{c_i} e^{-\lambda t} dt \qquad \text{(A2}$$

where A_i is the activity at the start of the interval i which we wish to determine by multiplying the $\overline{A_i}$ by some appropriate factor. Performing the above integration and solving for A_i, we get:

$$A_i = \overline{A}_i \left(\frac{c_i \lambda}{1 - e^{-\lambda c_i}} \right) \qquad \text{(A3}$$

and equation A3 is in the desired form.

The correction factors for multicomponent decay curves, growth and decay of daughter activities, and combinations of these cannot be determined in such a straight forward manner. The correction factor for a two component curve will be derived here and the correction factors for other types of decay curves can be derived in an analogous manner.

The equation for a two component decay curve can be written as:

$$A_1(t) + A_2(t) = A_{10}e^{-\lambda_1 t} + A_{20}e^{-\lambda_2 t} \qquad \text{(A4}$$

where $A_1(t)+A_2(t)$ is the activity at time t, A_{10} and A_{20} are the activities of the first and second components at t=0, and λ_1 and λ_2 are the decay constants for the first and second components, respectively. Integrating this equation over the ith interval:

$$\bar{A}_{1i} + \bar{A}_{2i} = \overline{A_{1i} + A_{2i}} = \frac{1}{c_i}\left(A_{1i}\int_0^{c_1} e^{-\lambda_1 t}dt + A_{2i}\int_0^{c_1} e^{-\lambda_2 t}dt\right) \qquad \text{(A5}$$

$$\overline{A_{1i} + A_{2i}} = \frac{A_{1i}}{c_i\lambda_1}\left(1 - e^{-\lambda_1 c_i}\right) + \frac{A_{2i}}{c_i\lambda_2}\left(1 - e^{-\lambda_2 c_i}\right) \qquad \text{(A6}$$

where $\overline{A_1+A_2}$ is the measured average activity during the ith interval and A_{1i} and A_{2i} are the activities of the two components at the start of this interval. In order to solve for $(A_{1i}+A_{2i})$

$$\frac{A_{2i}}{c_i\lambda_1}\left(1 - e^{-\lambda_1 c_i}\right) \qquad \text{(A7}$$

must be added and subtracted from the right hand side of equation A6.

$$\overline{A_{1i} + A_{2i}} = \frac{A_{1i} + A_{2i}}{c_i\lambda_1}\left(1 - e^{-\lambda_1 c_i}\right) + \frac{A_{2i}}{c_i\lambda_2}\left(1 - e^{-\lambda_2 c_i}\right)$$

$$- \frac{A_{2i}}{c_i\lambda_1}\left(1 - e^{-\lambda_1 c_i}\right) \qquad \text{(A8}$$

solving this for $(A_{1i}+A_{2i})$ gives:

$$A_{1i} + A_{2i} = \frac{\overline{A_{1i} + A_{2i}}\lambda_1 c_i}{\left(1 - e^{-\lambda_1 c_i}\right)} + A_{2i}\left(1 - \frac{\lambda_1\left(1 - e^{-\lambda_2 c_i}\right)}{\lambda_2\left(1 - e^{-\lambda_1 c_i}\right)}\right) \qquad \text{(A9}$$

At this point, some explanation is necessary. The A_{2i} on the right hand side of equation A9 is not equivalent to the A_{2i} on the left hand side. The A_{2i} on the right hand side is to be calculated from from the decay curve parameters as $A_{20}\exp(-\lambda_2 t_i)$ as A_{20} and λ_2 are parameters which are available during each iteration of a least squares fit. From first appearances, it appears that we now have an acceptable form, but this is not the correction factor form required. The first term on the right hand side is sensitive to statistical fluctuations in the measured $\overline{A_{1i}+A_{2i}}$ while the second term is not. Because of this, equation A9 is not valid when statistical fluctuations in the average count rate become important. In order to alleviate this problem, we must create the correction factor form in which the measured average activity, $\overline{A_{1i}+A_{2i}}$ is multiplied by this correction factor which depends only on the parameters of the decay curve itself. To do this, we first calculate the expected average count rate during the interval using the decay curve parameters.

$$\overline{A_{iCALC}} = \frac{A_{10}e^{-\lambda_1 t_i}\left(1 - e^{-\lambda_1 c_i}\right)}{\lambda_1 c_i} + \frac{A_{20}e^{-\lambda_2 c_i}\left(1 - e^{-\lambda_2 c_i}\right)}{\lambda_2 c_i} \qquad \text{(A10}$$

and rewrite equation 10 in the desired correction factor form:

$$A_{1i} + A_{2i} = \overline{A_{1i} + A_{2i}}\left\{\frac{c_i\lambda_1}{\left(1 - e^{-\lambda_1 c_i}\right)}\right.$$

$$\left. + \frac{A_{20}e^{-\lambda_2 t_i}}{\overline{A_{iCALC}}}\left(1 - \frac{\lambda_1\left(1 - e^{-\lambda_2 c_i}\right)}{\lambda_2\left(1 - e^{-\lambda_1 c_i}\right)}\right)\right\} \qquad \text{(A11}$$

The correction factors for 3,4, and 5 component decay curves can be written almost by inspection and are presented in the next section. The correction factors for growth and decay curves for daughter activities can be derived in a similar manner in the next section also.

SECTION A3 THE EQUATIONS

All i subscripts refer to the count interval and all j subscripts refer to the radioactive component.

SINGLE COMPONENT

$$A_{1i} = \overline{A_{1i}}\left(\frac{\lambda_1 c_i}{\left(1 - e^{-\lambda_1 c_i}\right)}\right) \qquad \text{(A12}$$

TWO COMPONENTS

SEE EQUATION A11 (A13

SEE EQUATION A10

(A14

THREE COMPONENTS

$$A_{1i} + A_{2i} + A_{3i} = \overline{A_{1i} + A_{2i} + A_{3i}} \left\{ \left(\begin{array}{c} \text{THE PART OF A11} \\ \text{IN BRACES} \end{array} \right) \right.$$

$$\left. + \frac{A_{30} e^{-\lambda_3 t_i}}{A_{iCALC}} \left(1 - \frac{\lambda_1 \left(1 - e^{-\lambda_3 c_i} \right)}{\lambda_3 \left(1 - e^{-\lambda_1 c_i} \right)} \right) \right\} \qquad \text{(A15}$$

$$\overline{A_{iCALC}} = \left(\begin{array}{c} \text{LEFT HAND SIDE} \\ \text{OF EQUA. A10} \end{array} \right) + \frac{A_{30} e^{-\lambda_3 t_i} \left(1 - e^{-\lambda_3 c_i} \right)}{\lambda_3 c_i} \qquad \text{(A16}$$

The equations for more components can be written by inspection

GROWTH AND DECAY

$$A_{2i} = \overline{A_{2i}} \left\{ \frac{\lambda_2 c_i}{\left(1 - e^{-\lambda_2 c_i} \right)} + \frac{A_{10} \lambda_2 e^{-\lambda_1 t_i}}{(\lambda_2 - \lambda_1) \overline{A_{iCALC}}} \left(1 - \frac{\lambda_2 \left(1 - e^{-\lambda_1 c_i} \right)}{\lambda_1 \left(1 - e^{-\lambda_2 c_i} \right)} \right) \right\} \qquad \text{(A17}$$

$$\overline{A_{iCALC}} = \frac{\lambda_2 A_{10} e^{-\lambda_1 t_i} \left(1 - e^{-\lambda_1 c_i} \right)}{\lambda_1 (\lambda_2 - \lambda_1) c_i} - \frac{A_{10} e^{-\lambda_2 t_i} \left(1 - e^{-\lambda_2 c_i} \right)}{(\lambda_2 - \lambda_1) c_i}$$

$$+ \frac{A_{20} e^{-\lambda_2 t_i} \left(1 - e^{-\lambda_2 c_i} \right)}{\lambda_2 c_i} \qquad \text{(A18}$$

GROWTH AND DECAY + ONE COMPONENT

$$A_{2i} + A_{3i} = \overline{A_{2i} + A_{3i}} \left\{ \left(\begin{array}{c} \text{THE PART OF A17} \\ \text{IN BRACES} \end{array} \right) + \frac{A_{30} e^{-\lambda_3 t_i}}{\overline{A_{iCALC}}} \left(1 - \frac{\lambda_2 \left(1 - e^{-\lambda_3 c_i} \right)}{\lambda_3 \left(1 - e^{-\lambda_2 c_i} \right)} \right) \right\} \quad \text{(A19}$$

$$\overline{A_{iCALC}} = \left(\begin{array}{c} \text{LEFT HAND SIDE OF} \\ \text{EQ. A18} \end{array} \right) + \frac{A_{30} e^{-\lambda_3 t_i} \left(1 - e^{-\lambda_3 c_i} \right)}{\lambda_3 c_i} \quad \text{(A20}$$

The equations for growth and decay + more components can be written by inspection

GROWTH AND DECAY + GROWTH AND DECAY

$$A_{2i} + A_{4i} = \overline{A_{2i} + A_{4i}} \left\{ \left(\begin{array}{c} \text{THE PART OF A17} \\ \text{IN BRACES} \end{array} \right) + \frac{\lambda_4 A_{30} e^{-\lambda_3 t_i}}{(\lambda_4 - \lambda_3)\, \overline{A_{iCALC}}} \left(\frac{\lambda_2 \left(1 - e^{-\lambda_4 c_i} \right)}{\lambda_4 \left(1 - e^{-\lambda_2 c_i} \right)} - \frac{\lambda_2 \left(1 - e^{-\lambda_3 c_i} \right)}{\lambda_3 \left(1 - e^{-\lambda_2 c_i} \right)} \right) + \frac{A_{40} e^{-\lambda_4 t_i}}{\overline{A_{iCALC}}} \left(1 - \frac{\lambda_2 \left(1 - e^{-\lambda_4 c_i} \right)}{\lambda_4 \left(1 - e^{-\lambda_2 c_i} \right)} \right) \right\} \quad \text{(A21}$$

$$\overline{A_{iCALC}} = \left(\begin{array}{c} \text{LEFT HAND SIDE} \\ \text{OF EQ. A18} \end{array} \right) + \frac{\lambda_4 A_{30} e^{-\lambda_3 t_i} \left(1 - e^{-\lambda_3 c_i} \right)}{\lambda_3 (\lambda_4 - \lambda_3) c_i} - \frac{A_{30} e^{-\lambda_4 t_i} \left(1 - e^{-\lambda_4 c_i} \right)}{(\lambda_4 - \lambda_3) c_i} + \frac{A_{40} e^{-\lambda_4 t_i} \left(1 - e^{-\lambda_4 c_i} \right)}{\lambda_4 c_i} \quad \text{(A22}$$

The equations for growth and decay + growth and decay + individual components can also now be written by inspection.

REFERENCES

[ALI71] S. A. Ali, S. H. Eberle; Inorg. Nucl. Chem. Lett. 7 153 (1971)

[ALY67] H. F. Aly, R. M. Latimer; JINC 29 2041 (1967)

[ARM85] P. Armbruster, Y. K. Agarwal, W. Brüchle, M. Brügger, J. P. Dufour, H. Gäggeler, F. P. Hessberger, S. Hofmann, P. Lemertz, G. Münzenberg, K. Poppenseiker, W. Reisdorf, M. Schädel, K.-H. Schmidt, J. H. R. Schneider, V. F. W. Schneider, K. Sümmerer, D. Vermeulen, G. Wirth, A. Ghiorso, K. E. Gregorich, D. Lee, M. Leino, K. J. Moody, G. T. Seaborg, R. B. Welch, P. Wilmarth, S. Yashita, C. Frink, N. Gruelich, G. Herrmann, N. Hildebrand, J. V. Kratz, N. Trautmann, M. M. Fowler, D. C. Hoffman, W. R. Daniels, H. R. von Gunten, H. Dörnhofer; Phys. Rev. Lett. 54 406 (1985)

[AUM74] D. C. Aumann, G. Müllen; NIM 115 75 (1974)

[BEV69] P. R. Bevington; Data Reduction and Error Analysis for the Physical Sciences; McGraw-Hill inc., (1969)

[BIG81] J. E. Bigelow; Private communication; TRU Shipment No. 1130

[BLO76] J. Blocki, J. Randrup, W. J. Swiatecki, C. F. Tsang; Annals of Physics 105 427 (1977)

[CHO56] G. R. Choppin, R. J. Silva; JINC 3 153 (1956)

[COL65] G. H. Coleman; The Radiochemistry of Plutonium; National Academy of Sciences - National Research Council, NAS-NS 3058

[EPH69] E. P. Horwitz,C. A. A. Bloomquist, D. J. Henderson; JINC 31 1149 (1969)

[EVA72] J. E. Evans, R. W. Lougheed, M. S. Coops, R. W. Hoff, E. K. Hulet; NIM 102 389 (1972)

[FIL74] T. D. Filer; Analytical Chem. 46 608 (1974)

[GAG81] H. Gäggeler, M. Schädel, W. Brüchle, J. V. Kratz, G. Wirth, N. Trautmann, P. Peuser, G. Tittel, R. Stakemann, G. Herrmann, E. K. Hulet, R. W. Lougheed, J. M. Nitschke, R. L. Hahn, R. L. Ferguson; Internat. Conf. on Nuclei Far From Stability, Helsignor, June (1981)

[GAG85] H. Gäggeler, W. Brüchle, M. Schädel, K. Sümmerer, G. Wirth, K. J. Moody, D. Lee, K. Gregorich, R. Welch, G. T. Seaborg, M. Lerch, Th, Blaich, G. Herrmann, N. Hildebrand, J. V. Kratz, N, Trautmann, H. R. von Gunten, W. R. Daniels, M. M. Fowler, D. C. Hoffman; Below-Target Yields from the Reactions of 40Ca and 48Ca Ions With 248 Cm; To be published.

[GAT75] B. Gatty, D. Guerreau, M. Lefort, J. Pouthas, X. Tarrago, J. Galin, B. Cauvin, J. Girard, H. Nifenecker; Z. Physik A273 65 (1975)

[GHI84] A. Ghiorso, D. Hoffman, E. K. Hulet, O. L. Keller, G. T. Seaborg; Large Einsteinium Accelerator Program; LBL pub-5118 (1984)

[GIL65] A. Gilbert, A. G. W. Cameron; Canadian J. of Physics 43 1446 (1965)

[GRC56] G. R. Choppin, B. G. Harvey, S. G. Thompson; JINC 2 66 (1956)

[GRO81] D. H. E. Gross, K. M. Hartmann; PR C24 2526 (1981)

[HAR62] B. G. Harvey; Introduction to Nuclear Physics and

Chemistry; Prentice-Hall, London (1962)

[HIG60] G. H. Higgins; The Radiochemistry of the Transcurium Elements; National Academy of Sciences - National Research Council, NAS-NS 3031

[HOF85] D. C. Hoffman, M. M. Fowler, W. R. Daniels, H. R. von Gunten, D. Lee, K, J, Moody, K. Gregorich, R. Welch, G. T. Seaborg, W. Brüchle, M. Brügger, H. Gäggeler, M. Schädel, K. Sümmerer, G. Wirth, Th. Blaich, G. Herrmann, N. Hildebrand, J. V. Kratz, M. Lerch, N, Trautmann; PR C31 1763 (1985)

[HOR69] E. P. Horwitz, C. A. A. Bloomquist, D. J. Henderson, D. E. Nelson; JINC 31 3255 (1969)

[HOR72] E. H. Horwitz, C. A. A. Bloomquist; JINC 34 3851 (1972)

[HOR73] E. P. Horwitz, C. A. A. Bloomquist; JINC 35 271 (1973)

[HOR75] E. P. Horwitz, C. A. A. Bloomquist; JINC 37 425 (1975)

[HOW80] W. M. Howard, P. Möller; ANDT 25 219 (1980)

[HUB80] F. Hubert, A. Fleury, R. Bimbot, D. Gardes; Annales de Physique, supplement, 5 1 (1980)

[HUL83] E. K. Hulet; Radiochimica Acta 32 7 (1983)

[KLA84] H. V. Klapdor, J. Metzinger, T. Oda; ANDT 34 81 (1984)

[KSC82] K.-H. Schmidt, H. Delagrange, J. P. Dufour, N. Carjan, A. Fleury; Z. Phys. A308 215 (1982)

[LEE82] D. Lee, H. R. von Gunten, B. Jacak, M. Nurmia, Yuan-fang Liu, Cheng Luo, G. T. Seaborg, D. C. Hoffman; PR

C25 286 (1982)

[LEE83] D. Lee, K. J. Moody, M. J. Nurmia, G. T. Seaborg, H. R. von Gunten, D. C. Hoffman; PR C27 2656 (1983)

[LI 85] Wen Xin Li, K. E. Gregorich, R. B. Welch, W. Kot, D. Lee, G. T. Seaborg; LBL Nuclear Science Division Annual Report 1983-1984, LBL-18635 pg. 52 (1985)

[LUC83] R. Lucas, C. Gregoire, C. Ngo, J. Poitou, E. Tomasi, A. Gobbi, A. Olmi, H. Sann, G. Wirth, J. V. Kratz, U. Lynen; NP A413 516 (1983)

[MOO81] K. Moody, M. Nurmia, G. Seaborg; LBL Ann. Rept., LBL-11588 pg. 188 (1981)

[MOO83] K. J. Moody; Actinide Production in the Reaction of Heavy Ions With Curium-248; PhD Thesis, LBL-16249 (1983)

[MOO85] K. J. Moody; private communication

[MOR81] L. G. Moretto, R. P. Schmidt; Reports on Progress in Physics 44 533 (1981)

[MOU78] J. B. Moulton, J. E. Stephenson, R. P. Schmidt, G. J. Wozniak; NIM 157 325 (1978)

[MSC82] M. Schädel, W. Brüchle, H. Gäggeler, J. V. Kratz, K. Sümmerer, G. Wirth, G. Herrmann, R. Stakemann, G. Tittle, N. Trautmann, J. M. Nitschke, E. K. Hulet, R. W. Lougheed, R. L. Hahn, R. L. Ferguson; Phys. Rev. Lett. 48 852 (1982)

[MUL75] G. Müllen, D. C. Aumann; NIM 128 425 (1975)

[MYE80] W. D. Myers; Droplet Model of Atomic Nuclei; IFI/Plenum, New York (1977)

[MYE74] W. D. Myers, W. J. Swiatecki; Ann. Phys. 84 186

(1974)

[PEN60] R. A. Penneman, T. K. Keenan; The Radiochemistry of Americum and Curium; National Academy of Sciences - National Research Council, NAS-NS 3006 (1960)

[PHO69] E. P. Horwitz, C. A. A. Bloomquist; Inorg. Nucl. Chem. Lett. 5 753 (1969)

[PEP57] P. F. Peppard, G. W. Mason J. L. Maier, W. J. Driscoll; JINC 4 334 (1957)

[RVA58] R. Vaandenbosch, J. R. Huizenga; Proc. Int. Conf. Peaceful Uses At. Energy, 2nd; 15 pg. 284 United Nations, Geneva (1958)

[ROU69] J. T. Routti, S. G. Prussin; NIM 72 125 (1969)

[SCH78] M. Schädel, J. V. Kratz, H. Ahrens, W. Brüchle, G. Franz, H. Gäggeler, I. Warnecke, G. Wirth, G. Herrmann, N. Trautmann, M. Weis; Phys. Rev. Lett. 41 469 (1978)

[SCH82] M. Schädel, R. W. Lougheed, J. H. Landrum, J. F. Wild, R. J. Dougan, A. D. Hoover, E. K. Hulet, G. R. Bethune, A. Ghiorso, M. J. Nurmia, L. P. Somerville, K. J. Moody, G. T. Seaborg; LLL Annual Report, UCAR 1006 2-82/1 pg.100 (1982)

[SCH84] M. Schädel, D. Schärdt, K. Sümmerer, H. Gäggeler, W. Brüchle, M. Brügger, K. J. Moody, E. K. Hulet, A, D, Dougan, R. W. Lougheed, J. H. Landrum, R. J. Dougan, J. F. Wild, G. D. O'Kelley; LLL Annual Report, UCAR 10062-84/1 pg.6-26 (1984)

[SEG77] Emilio Segre; Nuclei and Particles; Second edition; W. A. Benjamin Inc., Reading Mass.

[SHO74] D. P. Shoemaker, C. W. Garland, J. I. Steinfeld;

Experiments in Physical Chemistry; third edition; McGraw-Hill inc., (1974)

[SMI56] H. L. Smith, D. C. Hoffmann; JINC 3 243 (1956)

[STE61] P. C. Stevenson, W. E. Nervik; The Radiochemistry of the Rare Earths, Scandium, Yttrium, and Actinium; National Academy of sciences - National Research Council, NAS-NS 3020 (1961)

[SUM84] K. Sümmerer, W. Brüchle, M. Brügger, H. Gäggeler, M. Schädel, D. Schardt, G. Wirth, C. Frink, N. Greulich, G. Hermann, N. Hildebrand, U, Hickmann, J. V. Kratz, P, Peuser, N. Trautmann, A. Ghiorso, K. E. Gregorich, D. Lee, K. J. Moody, G. T. Seaborg, R. B. Welch, P. Wilmarth, E. K. Hulet, A. D. Dougan, R. J. Dougan, J. H. Landrum, R. W. Lougheed, J. F. Wild, W. R. Daniels, M. Fowler, D. C. Hoffman, R. L. Hahn, R. C. Ferguson, D. O'Kelley, H. R. von Gunten, H. Dornhofer; GSI Preprint GSI-84-17 (1984)

[VAN58] R. Vandenbosch, T. D. Thomas, S. E. Vandenbosch, R. A. Glass, G. T. Seaborg; PR 111 1358 (1958)

[VER84] D. Vermeulen, H.-G. Clerc, C. C. Sahm, K.-H. Schmidt, J. G. Keller, G. Munzenberg, W. Reisdorf; Z. Phys. A318 157 (1984)

[WAT78] W. Wätzig, W. Westmeier; NIM 153 517 (1978)

[WEA68] B. Weaver, F. A. Kappelmann; JINC 30 263 (1968)

[WEL85] R. B. Welch, Actinide Production From Xenon Bombardments of Curium-248; PhD Thesis, LBL-19010 (1985)

[WIL80] W. W. Wilcke, J. R. Birkelund, H. J. Wollersheim, A.

D. Hoover, J. R. Huizenga, W. U. Schroder, L. E. Tubbs; Atomic Data and Nuclear Data Tables 25 389 (1980)

[WIL83] J. F. Wild, E. K. Hulet, R. W. Lougheed, J. H. Landrum, R. J. Dougan, A. D. Dougan, H. Gäggeler, M. Schädel, K. J. Moody, G. T. Seaborg; LLL Annual Report, UCAR 10062-83/1 pg.144 (1983)

[WIL71] B. D. Wilkins, M. J. Fluss, S. B. Kaufman, C. E. Gross, E. P. Steinberg; NIM 92 381 (1971)

[WIN63] J. W. Winchester; J Chromatog. 10 502 (1963)

[WOL84] H. J. Wollersheim; GSI Preprint GSI-84-34; submitted to Phys. Rev. C (1984)

[WOL76] H. Wollnik; NIM 139 311 (1976)

TABLE 2.3.1 THE COMPOSITION OF HAVAR

COMPONENT	WEIGHT %
Co	42.5
Cr	20.0
Fe	17.9
Ni	13.0
W	2.8
Mo	2.0
Mn	1.6
C	0.2
Be	0.04

TABLE 2.4.1 ENERGY LOSS THROUGH THE TARGET SYSTEM

	BEAM ENERGY (MeV)	ΔE (MeV)	BEAM ENERGY (MeV)	ΔE (MeV)	BEAM ENERGY (MeV)	ΔE (MeV)
ENTERING HAVAR	1036	85	1096	84	1156	83
ENTERING NITROGEN	951	14	1012	16	1073	16
ENTERING BERYLLIUM	934	171	996	169	1057	167
ENTERING CF_2O_3	763	29	827	28	890	28
LEAVING CF_2O_3	734		799		862	
AVERAGE ENERGY IN TARGET	748		813		876	

TABLE 3.3.1 CALCULATION OF UPPER LIMIT ON ^{247}Am COUNT RATE

n (SPECTRUM NUMBER)	MID TIME OF COUNT (HOURS)	UNCER. IN CNT. RATE (dpm)	$\frac{e^{-2\lambda t}}{\sigma_i^2}$	A_{0n}
1	0.666	0.6	0.276	1.90
2	0.873	0.6	0.135	1.56
3	1.096	0.6	0.062	1.45
4	1.387	0.4	0.051	1.38
5	1.760	0.4	0.014	1.36
6	2.229	0.4	0.002	1.36
7	2.604	0.4	0.001	1.36

UPPER LIMIT ON ^{247}Am ACTIVITY = 1.36 COUNTS/MINUTE

TABLE 3.3.2 CALCULATION OF INITIAL ACTIVITY OF ^{239}Am

When summed, the first five spectra gave:

Net counts @ 277.6 keV = 104 ± 62 counts

Net counts @ 226.4 keV = 128 ± 74 counts

Correcting for detector efficiency and radiation abundance:

$$\frac{104 \pm 62}{(0.097 \pm 0.005)(0.15 \pm 0.03)} = 7150 \pm 4510 \text{ decays}$$

$$\frac{128 \pm 74}{(0.119 \pm 0.006)(0.15 \pm 0.03)} = 7170 \pm 4400 \text{ decays}$$

The relative sizes of the two peaks agree . . . adding confidence to the identification as ^{239}Am.

A weighted average of these activities = 7160 ± 3150 = T

COUNT INTERVAL	TIME AT START	TIME AT END	$(\exp[-t_i]-\exp[-t_f])/\lambda$
1	7.448	9.448	1.223
2	9.491	13.491	2.053
3	13.536	17.536	1.622
4	21.707	25.707	1.008
5	25.745	29.745	0.797
		SUM =	6.703

A_0 = T / 6.703 = 1068 ± 470 decays/hour = 18 ± 8 decays/minute

TABLE 4.2.1 CROSS SECTIONS FROM ^{136}Xe + ^{249}Cf BOMBARDMENTS

NUCLIDE	HALF-LIFE	748 MeV CROSS SECTION	748 MeV ERROR	748 MeV COM	813 MeV CROSS SECTION	813 MeV ERROR	813 MeV COM	876 MeV CROSS SECTION	876 MeV ERROR	876 MeV COM
234-Np		8.	-	UL	7.	-	UL	6.	-	UL
236-Np	22.5h	130.	-	UL	110.	-	UL	65.	-	UL
238-Np		5.	-	UL	49.	6.		22.	3.	
239-Np		5.	-	UL	30.	5.		19.	3.	
240-Np	65.m	-	-		-	-		20.	-	UL
243-Pu		-	-		-	-		2.	-	UL
245-Pu		-	-		7.	-	UL	2.	-	UL
246-Pu		-	-		35.	-	UL	14.	-	UL
239-Am		1.4	-	UL	14.	6.		7.	3.	
240-Am		6.6	0.9		43.	4.		39.	4.	
242-Am	16.h	61.	10.		100.	18.		140.	30.	
244-Am	10.1h	59.	5.		155.	12.		132.	9.	
245-Am		25.	18.		98.	16.		86.	15.	
246-Am	25.m	17.	-	UL	36.	10.		8.	5.	
246-Am	39.m	21.	5.		34.	6.		20.	4.	
247-Am		14.	-	UL	9.	-	UL	4.	-	UL
249-Cm		170.	-	UL	35.	-	UL	85.	-	UL
244-Bk		6.	1.	LL	29.	3.	LL	60.	9.	LL
245-Bk		75.	9.		430.	70.		680.	70.	
246-Bk		390.	40.		1870.	170.		2400.	300.	
248-Bk	21.7h	2600.	300.		4600.	500.		4300.	600.	
249-Bk		1400.	600.		4200.	1400.		1100.	300.	

250-Bk	117.	11.		370.	30.	360.	30.	
251-Bk	29.	-	UL	40.	20.	20.	-	UL
245-Cf	2.5	0.8		21.	6.	44.	20.	
246-Cf	29.	4.		260.	60.	360.	80.	
247-Cf	400.	80.		3000.	500.	3100.	500.	
248-Cf	8000.	2000.		27000.	7000.	28000.	7000.	
253-Cf	6.1	0.8		28.	6.	18.	6.	
248-Es	11.	-	UL	51.	-	UL	58.	-	UL
249-Es	64.	8.		530.	90.	560.	90.	
250-Es 2.22h	165.	20.		870.	140.	750.	140.	
250-Es 8.6h	270.	30.		890.	140.	1140.	140.	
251-Es	250.	90.		1600.	600.	1400.	500.	
252-Es	69.	10.		470.	100.	490.	100.	
253-Es	9.6	1.3		68.	13.	53.	10.	
254-Es 39.3h	0.55	0.12		4.6	0.9	4.8	0.9	
255-Es	0.030	0.009		0.61	0.13	0.48	0.10	
256-Es 7.6h	-	-		0.05	0.04	-	-	
250-Fm	3.3	0.9		31.	8.	12.	3.	
251-Fm	44.	9.		200.	50.	90.	30.	
252-Fm	25.	4.		130.	20.	77.	10.	
253-Fm	12.	2.		49.	12.	22.	5.	
254-Fm	2.0	0.3		24.	4.	7.	2.	
256-Fm	0.10	0.03		1.1	0.2	0.75	0.21	
256-Md	0.04	0.04		0.21	0.08	0.15	0.10	

TABLE 4.2.2 CROSS SECTION CONTRIBUTIONS FROM ^{245}Cm IN THE TARGET

NUCLIDE	CROSS SECTION	ANALOGOUS PRODUCT	CROSS SECTION	APPARENT CONTRIB.	FRAC. DUE TO 245-CM
238-Np	49.	242-Am	~100.	0.50	0.010
239-Np	30.	243-Am	~150.	0.75	0.025
240-Am	43.	244-Bk	~50.	0.25	0.006
242-Am	100.	246-Bk	1870.	9.35	0.093
244-Am	155.	248-Bk	4600.	23.0	0.148
245-Am	98.	249-Bk	4200.	21.0	0.214
246-Am	70.	250-Bk	370.	1.85	0.026

FIGURE CAPTIONS

Figure 2.2.1 The plating cell used in the molecular plating technique for making the ^{249}Cf targets.

Figure 2.3.1 A schematic of the Modular Fast Access Target System as used for ^{136}Xe + ^{249}Cf irradiations.

Figure 2.3.2 A exploded view of the Modular Fast Access Target System. The beam enters from the upper left hand side of the figure and the endpiece shown at the lower left fits against the o-ring at the lower right. Some modifications were made in the Catcher Foil Holder and the End Piece Clamp to accommodate the two piece catcher foil used in these experiments.

Figure 2.3.3 A plot of the probability of catching products vs. the recoil angle with respect to the beam axis for the two piece catcher foil.

Figure 2.4.1 The results of the RANGY code calculations. The ^{136}Xe energy in the ^{249}Cf target material vs. the incident energy from the SuperHILAC. The upper and lower diagonal lines are the centroids of the beam energy distributions at the beginning and end of the ^{249}Cf target material, respectively. The solid vertical lines indicate the centroids of the energies used in this work. The vertical dashed lines indicate the energies in the target for beam particles whose incident energy differed from the centroid energy by 10 MeV (a typical HWHM of the undegraded beam). The two horizontal lines represent the Coulomb barrier for this reaction assuming r_0 = 1.40 and 1.35 fm. The curve

plotted at the center of the figure indicates a more realistic energy distribution throughout the Cf target material, calculated by folding a Gaussian beam distribution with a FWHM of 35-40 MeV with a 28 MeV linear energy loss of the centroid of the distribution as it passes through the Cf_2O_3.

Figure 2.5.1 A typical elution curve for a test run of the 13M HCl cation exchange column for the separation of actinides from lanthanides. The activities measured by detection of alpha particles are shaded and the activity measured by detection of beta radiation are unshaded.

Figure 2.5.2 In the upper left are the elution positions of the actinides, lanthanides, and Y from a cation exchange column with α-HIBA as the elutriant. The lower part of the figure is a plot of these published elution positions vs. the position from the column used in this work for a typical calibration run. The predicted elution positions for Md and Fm are indicated by the crosses.

Figure 2.5.3 A typical elution curve for a calibration run of the α-HIBA cation exchange column. The beta activities are indicated by the unshaded regions and the alpha activities are indicated by the shaded regions (the beta detector was sensitive to alpha particles).

Figure 2.5.4 A typical elution curve from a calibration run with the HDEHP/0.4M HNO_3 extraction chromatography

curve fitting code. This fit was to a simulated three component decay curve. The contents of the file are explained in the text (section 3.4).

Figure 3.4.2 Continuation of figure 3.4.1.

Figure 4.2.1 The cross sections from the 1036 MeV ^{136}Xe + ^{249}Cf bombardments (748 MeV in the target). Open circles indicate the cross section for one half of an isomer pair. Points with downward arrows indicate that the cross section is an upper limit on an activity which was not observed. Points with upward arrows indicate that the cross section is a lower limit based on he assumption that the most abundant gamma-ray activity has an absolute abundance of 100%. The lines are drawn to connect the points and have no other significance.

Figure 4.2.2 The cross sections from the 1096 Mev ^{136}XE + ^{249}Cf bombardments (813 MeV in the target). The symbols have the same meaning as in figure 4.2.1.

Figure 4.2.3 The cross sections from the 1156 MeV ^{136}Xe + ^{249}Cf bombardments (876 MeV in the target). The symbols have the same meaning as in figure 4.2.1.

Figure 4.2.4 A contour plot of the actinide production cross sections from the 1156 Mev ^{136}Xe + ^{249}Cf bombardments (876 MeV in the target). the contours are labeled in units of microbarns.

Figure 4.2.5 The excitation functions for the production of Am and Bk isotopes. Open points refer to cross sections for one half of an isomer pair. The FWHM of

the energy distributions (see fig. 2.4.1) are indicated along the energy axis. The lines are drawn through the points and for reasons explained in section 4.2.3 and figure 4.2.7 do not represent the true cross section vs. energy relation.

Figure 4.2.6 the excitation functions for the production of Cf, Es, and Fm isotopes (the excitation function for 256Md is also given). The symbols have the same meanings as in figure 4.2.5.

Figure 4.2.7 An example of the corrections to the excitation functions necessary because the cross sections are not constant over the energy widths of each of the bombardments. This is an example of n approximate correction which could be applied to all of the lowest energy points on the excitation function curves of figures 4.2.5 and 4.2.6. It can be seen that the mean of the folded distribution is about 12 MeV higher than the centroid of the beam energy distribution.

Figure 4.3.1 A contour plot of the actinide production cross sections from the 745 MeV ^{136}Xe + ^{248}Cm bombardments [MOO83]. The cross section contours are labeled in microbarns.

Figure 5.2.1 A plot of the ds/dZ distribution for different E bins the highest energy ^{136}Xe + ^{249}Cf bombardments as calculated by the methods in [WOL84].

Figure 5.3.1 A contour plot of the potential energy surface for ^{136}Xe + ^{249}Cf reactions. This surface was

calculated at the interaction radius (15.52 fm) and at 0 h. the contours are 5 MeV apart except for the dashed contour at +2.5 MeV. The injection point is labelled with a cross and the saddle point can be seen at Z=93 and N=145.

Figure 5.3.2 The same contour plot as in figure 5.3.1 with the shell effects removed from the ground state masses. The contours are spaced 5 MeV apart.

Figure 5.4.1 A contour plot of the initial cross section distribution (before deexcitation) for the ^{136}Xe + ^{249}Cf reaction as calculated by the methods in section 5. Contours are labelled in mitrobarns.

Figure 5.6.1 A plot of the calculated cross sections vs. N for various values of the Z of the target-like fragment from the ^{136}Xe + ^{249}Cf reaction at 870 MeV.

Figure 5.6.2 A contour plot of the calcualted cross sections persented in figure 5.6.1. contours are labelled in microbarns

Figure 5.6.3 The results of this calculation for the Am, Bk, Es, and Fm isotopes plotted with the experimental cross sections. The calculated cross sections are represented by squares and the experimental cross sections are represented by circles . Open circles represent the cross section for one half of an isomer pair. Downward and upward pointing arrows indicate that the experimental cross section is an upper or lower limit, respectively.

Figure A.1 An illustration of the corrections for non-linear decay during the counting interval corrections to decay curves explained in appendix A. The significance of the curves and the points are explained in the text of appendix A.

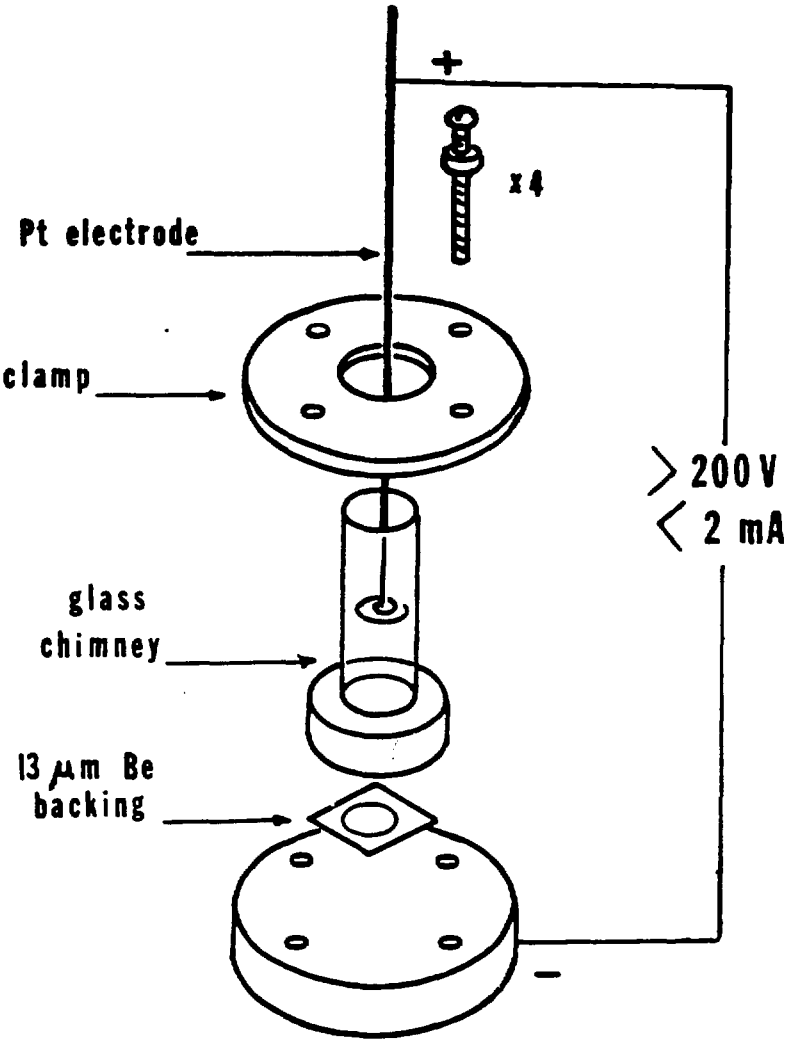

Target Fabrication

XBL 858-3246

Figure 2.2.1

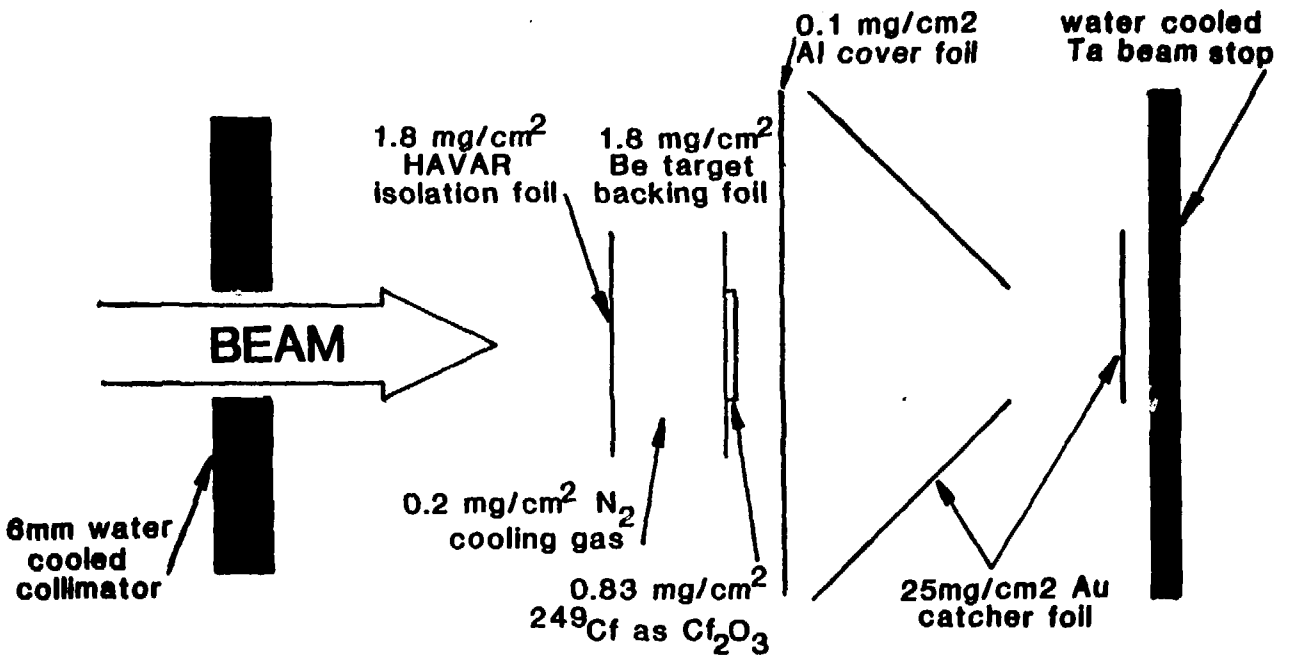
0.1 mg/cm2
Al cover foil
water cooled
Ta beam stop
1.8 mg/cm2
HAVAR
isolation foil
1.8 mg/cm2
Be target
backing foil
BEAM
6mm water
cooled
collimator
0.2 mg/cm2 N2
cooling gas
0.83 mg/cm2
249Cf as Cf2O3
25mg/cm2 Au
catcher foil
XBL 857-3001

Figure 2.3.1

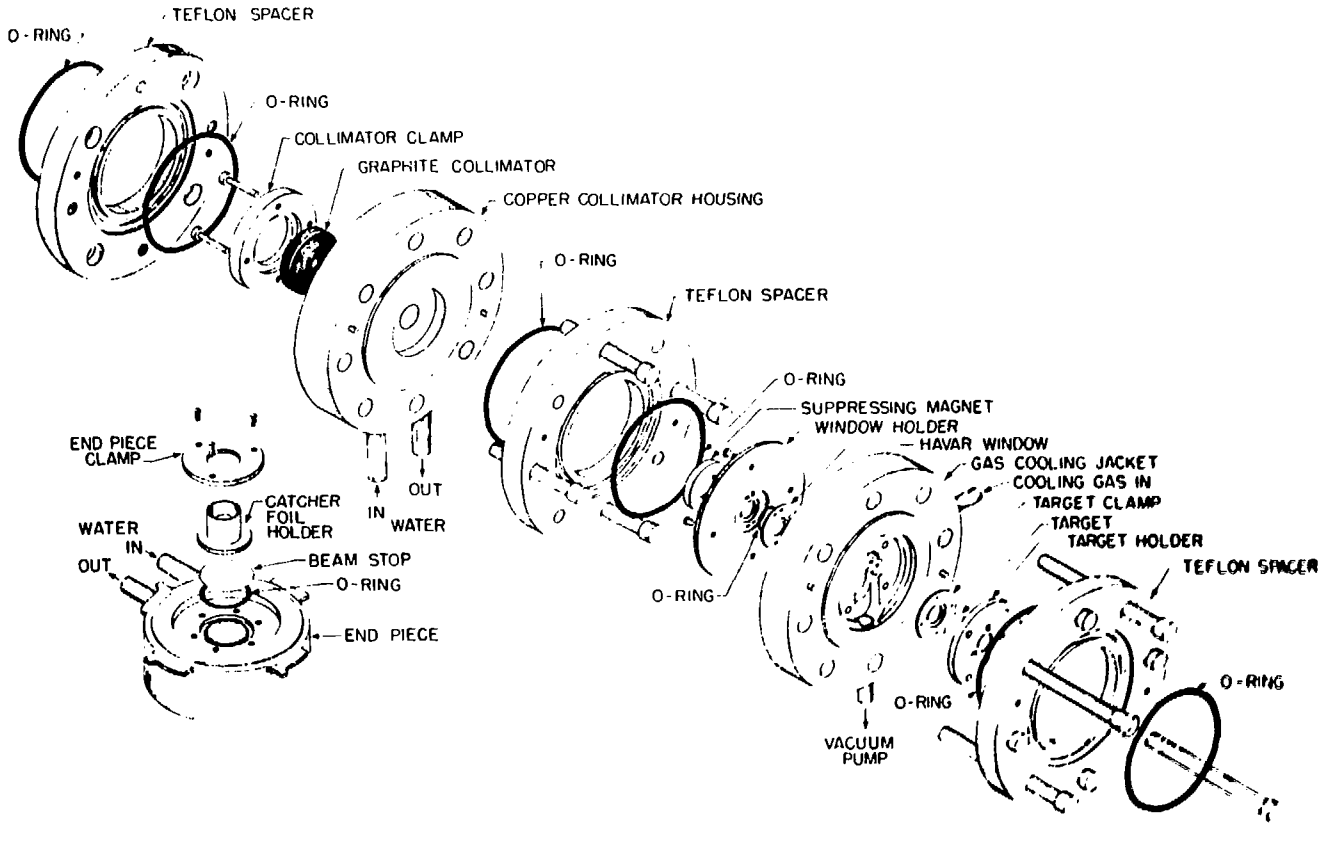
O-RING
TEFLON SPACER
O-RING
COLLIMATOR CLAMP
GRAPHITE COLLIMATOR
COPPER COLLIMATOR HOUSING
O-RING
TEFLON SPACER
O-RING
SUPPRESSING MAGNET
WINDOW HOLDER
HAVAR WINDOW
GAS COOLING JACKET
COOLING GAS IN
TARGET CLAMP
TARGET
TARGET HOLDER
TEFLON SPACER
O-RING
O-RING
END PIECE CLAMP
CATCHER FOIL HOLDER
WATER IN
OUT
BEAM STOP
O-RING
END PIECE
OUT
IN
WATER
O-RING
VACUUM PUMP

Figure 2.3.2

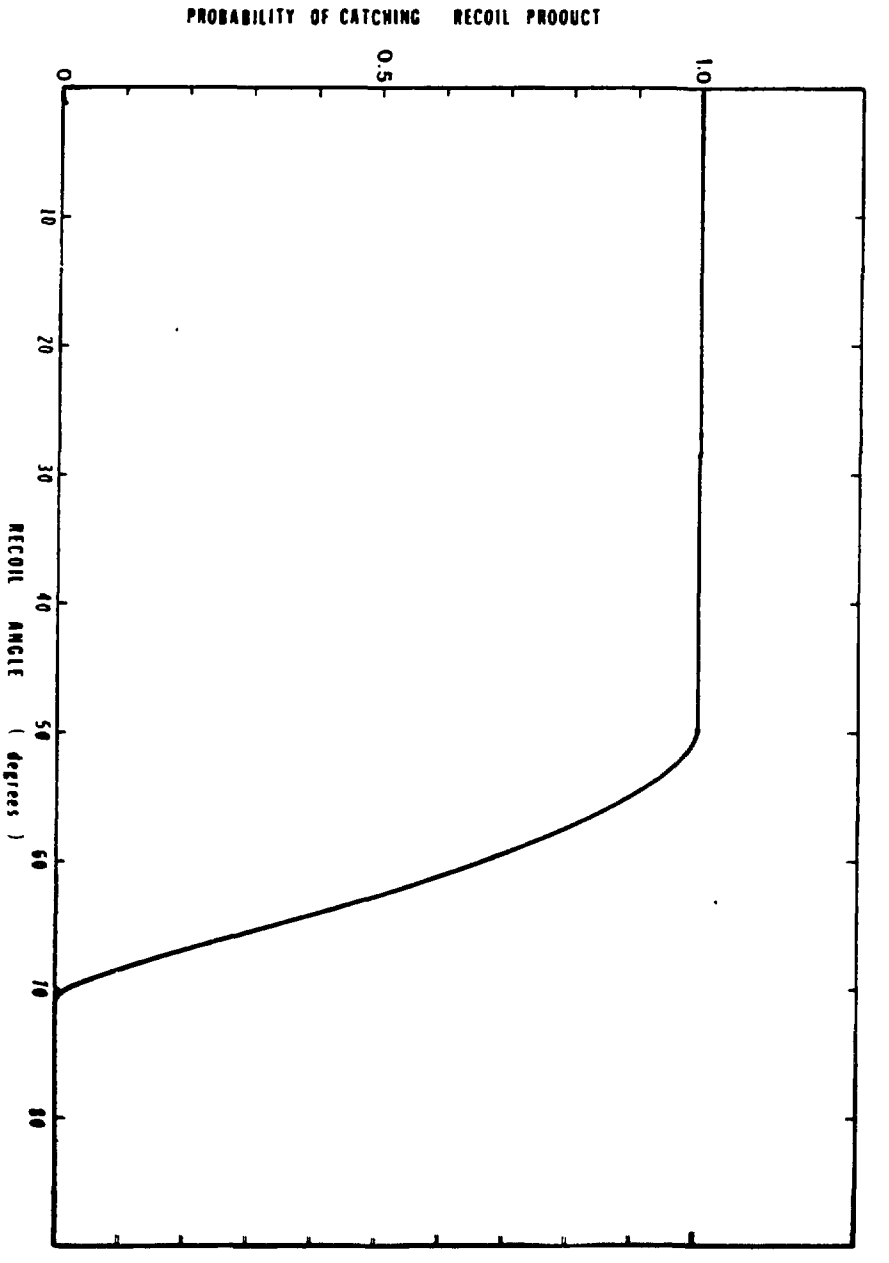

XBL 858-3245

Figure 2.3.3

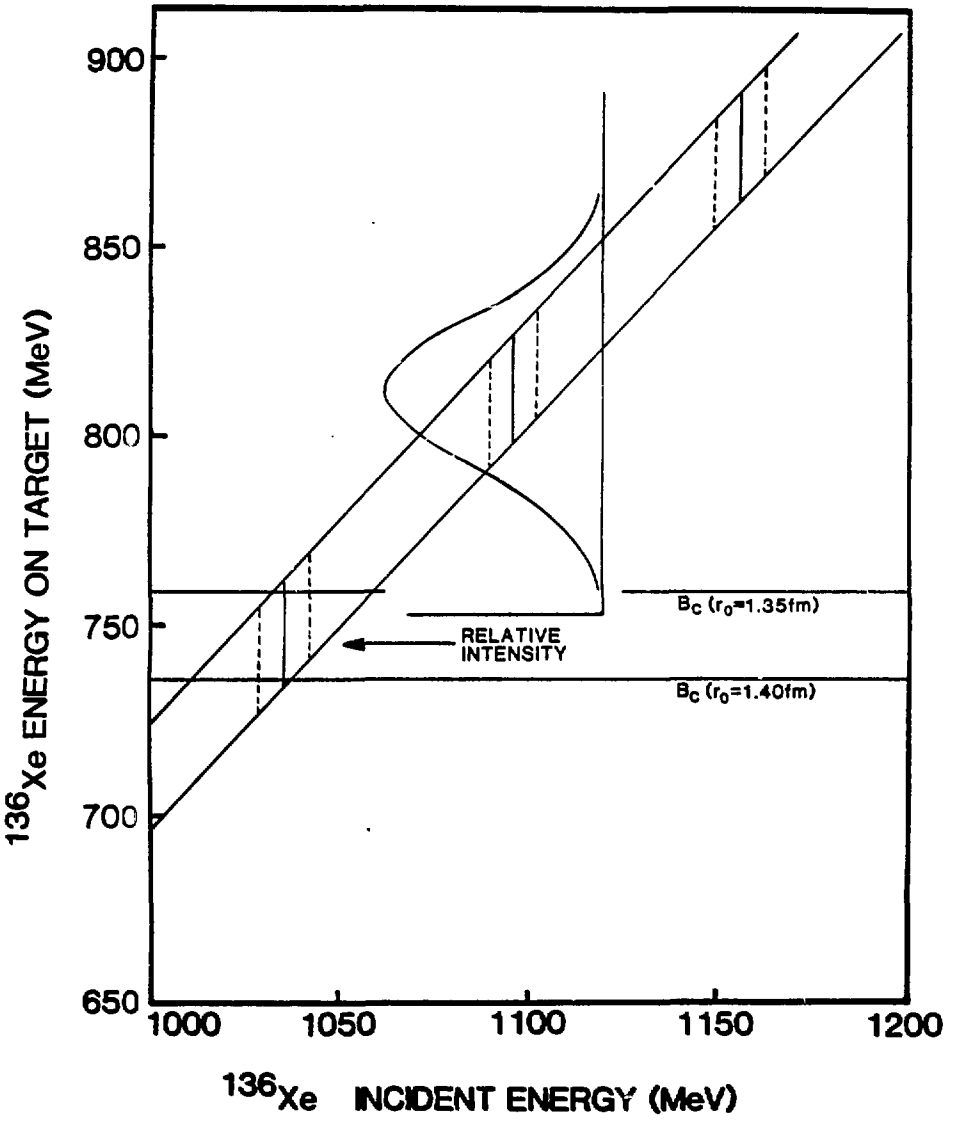

XBL 857-3107

Figure 2.4.1

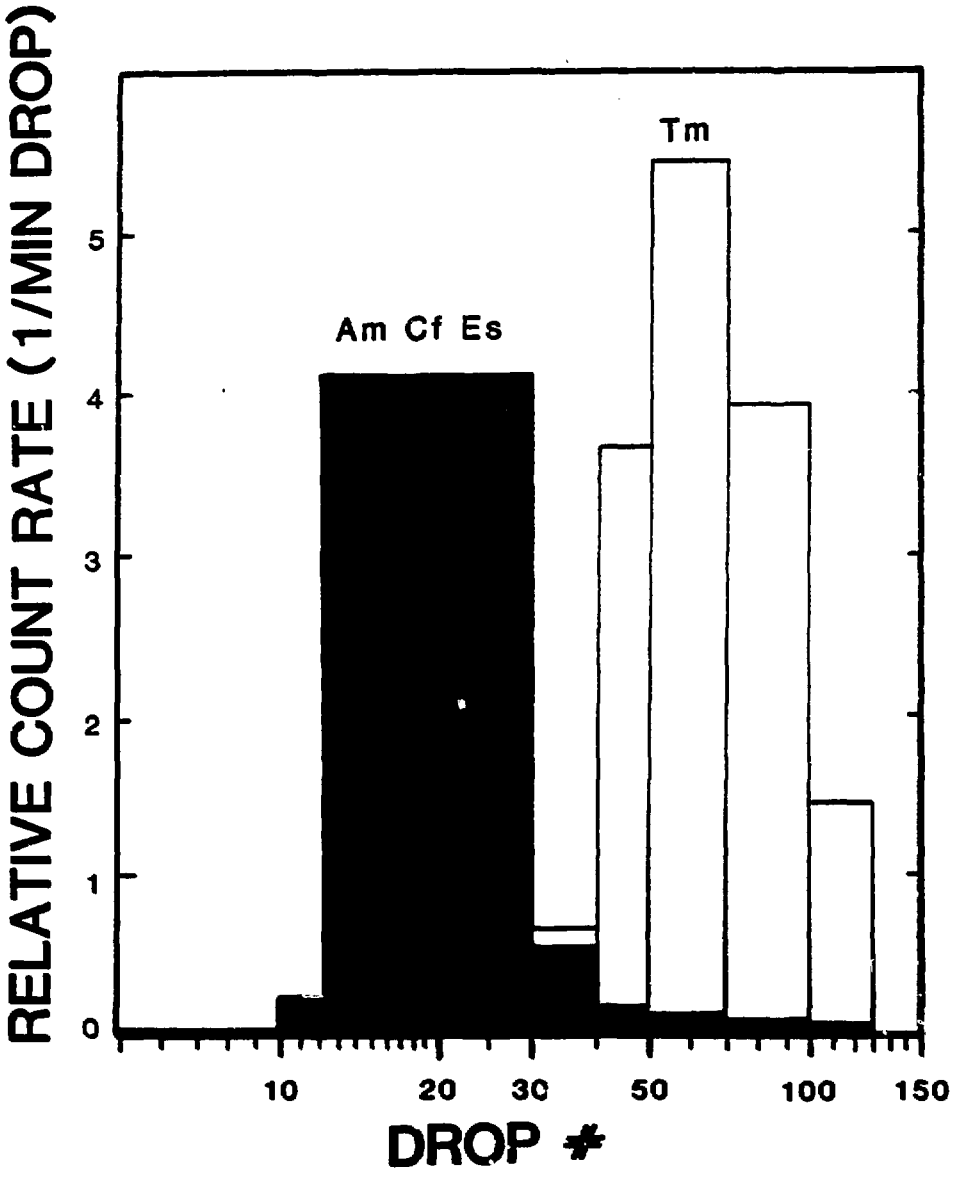

XBL 857-3004

Figure 2.5.1

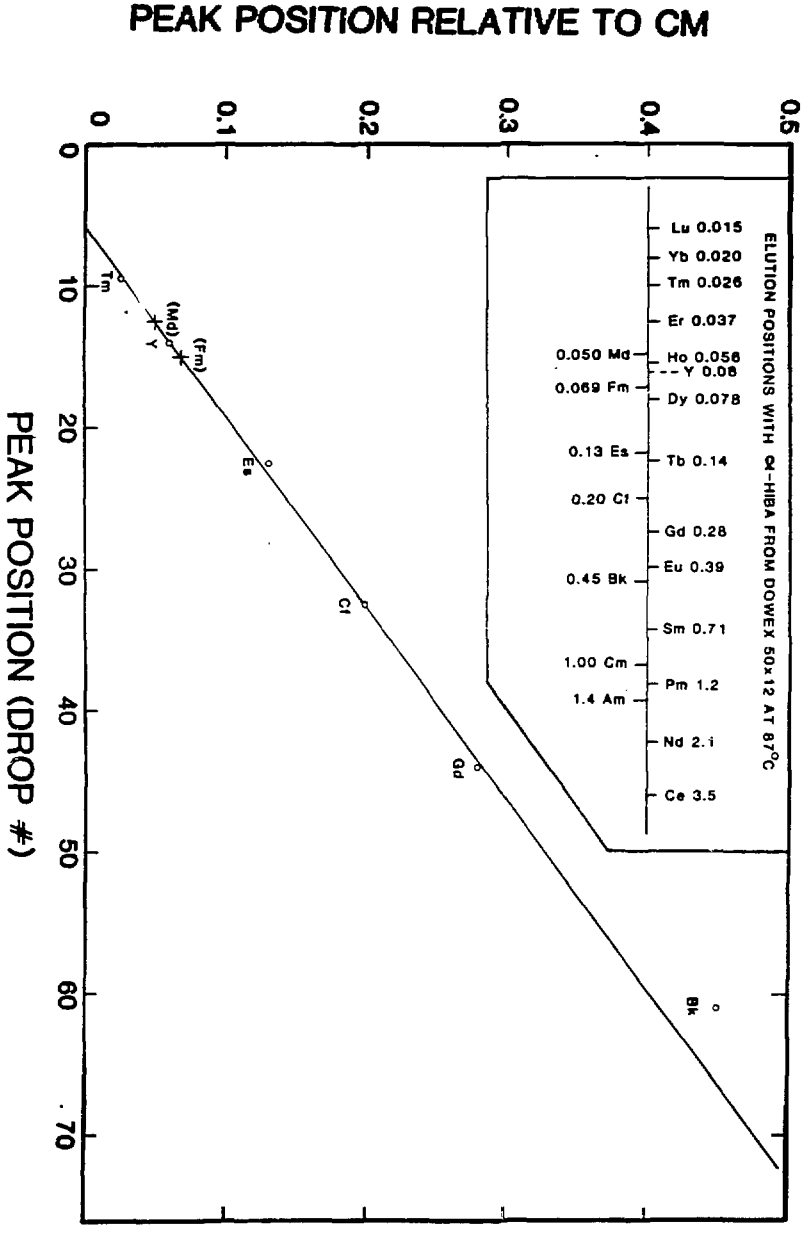

Figure 2.5.2

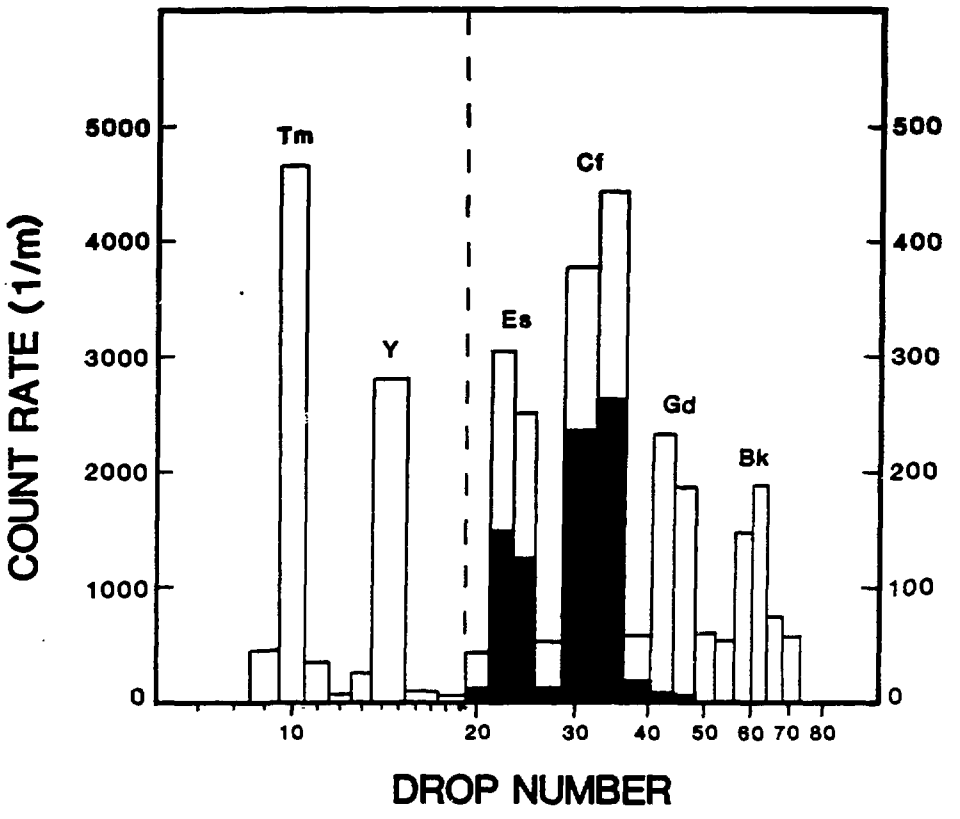

XBL 847-3019

Figure 2.5.3

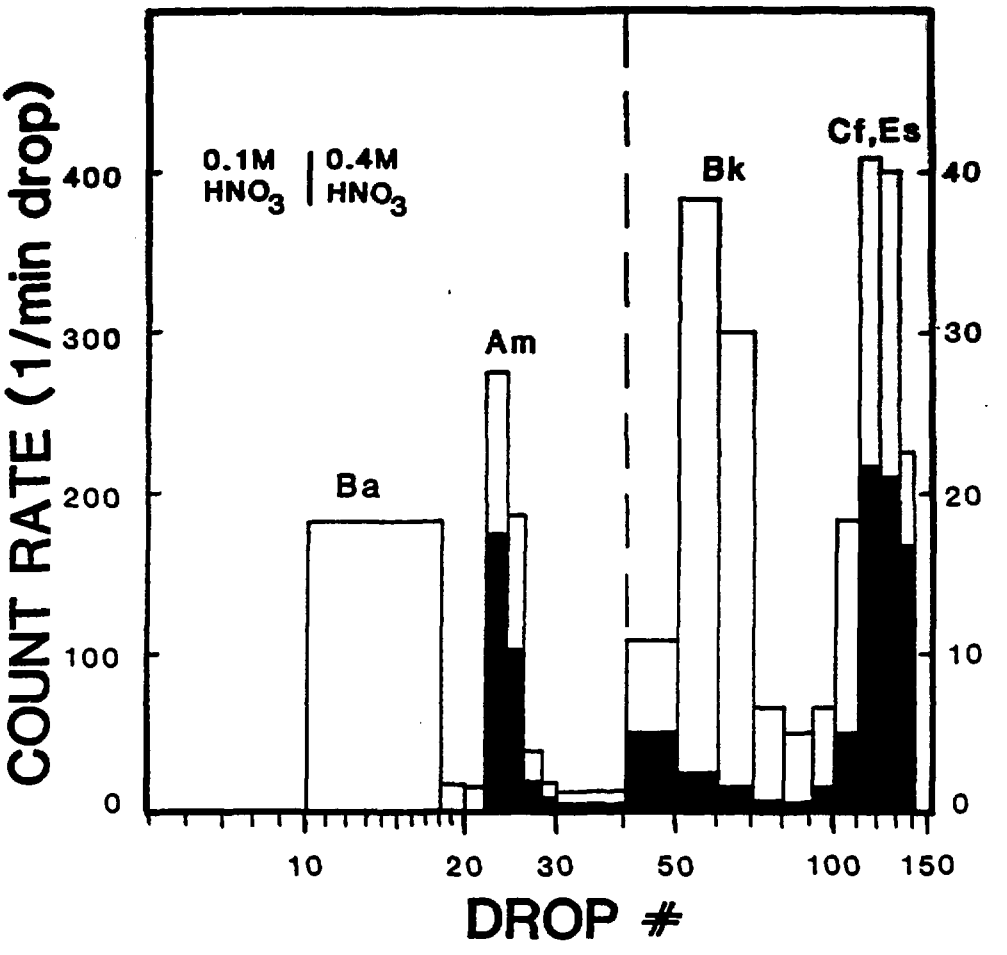

XBL 857-3003

Figure 2.5.4

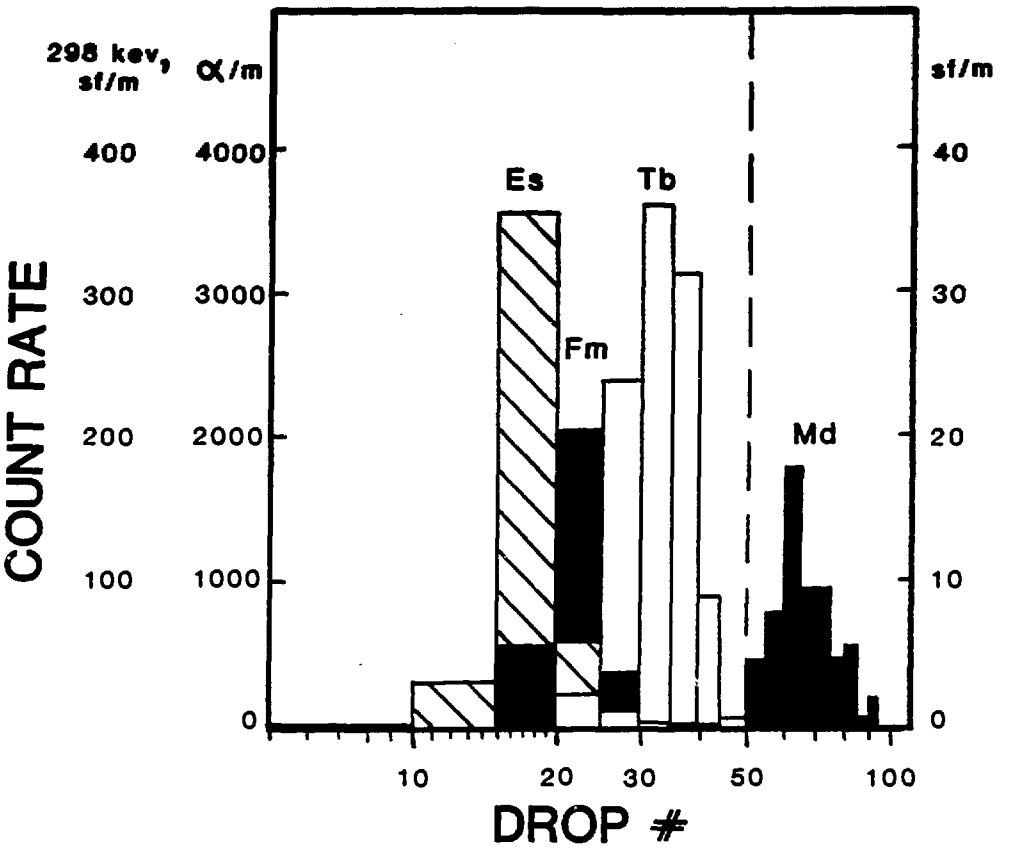

XBL 857-3002

Figure 2.5.5

+3 ACTINIDE GROUP SEPARATION

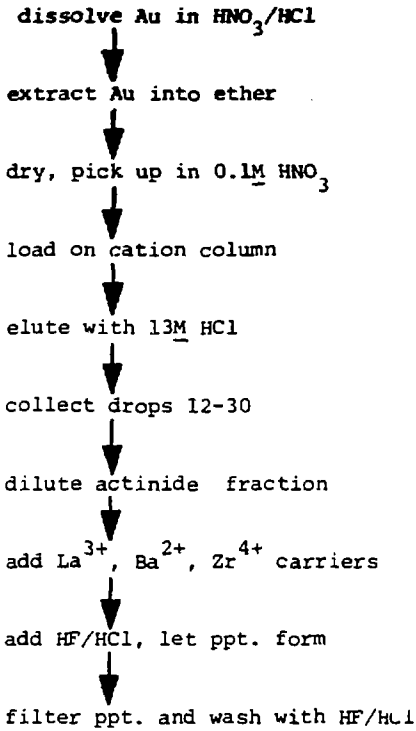

XBL 858-3242

Figure 2.5.6

FAST α-HIBA SEPARATION

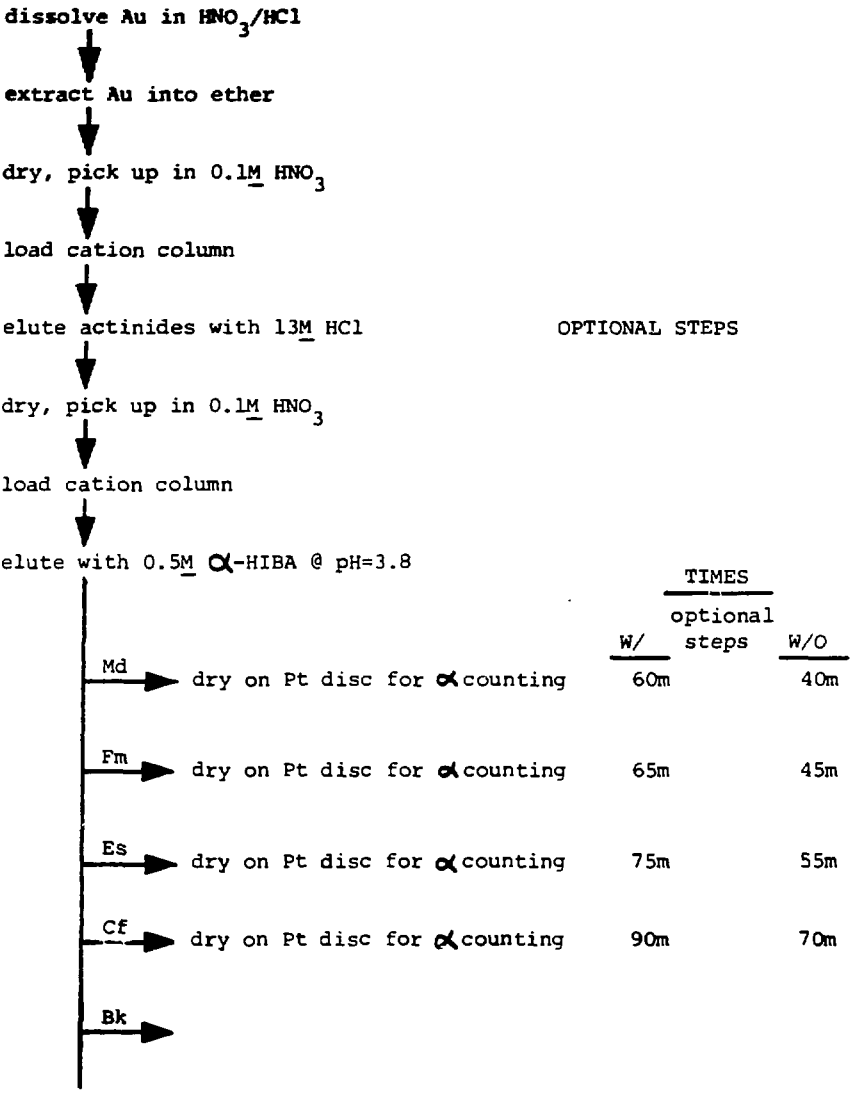

XBL 858-3239

Figure 2.5.7

FAST HDEHP/HNO_3 SEPARATION

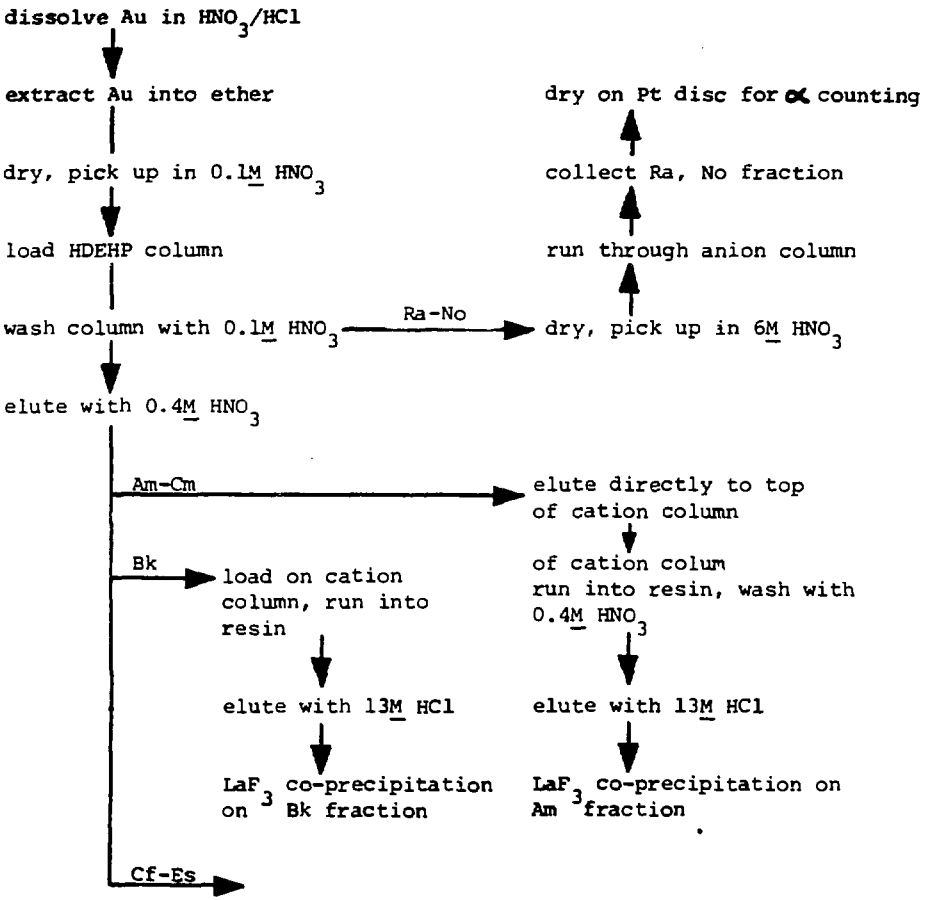

XBL 858-3241

Figure 2.5.8

LONG BOMBARDMENT SEPARATION

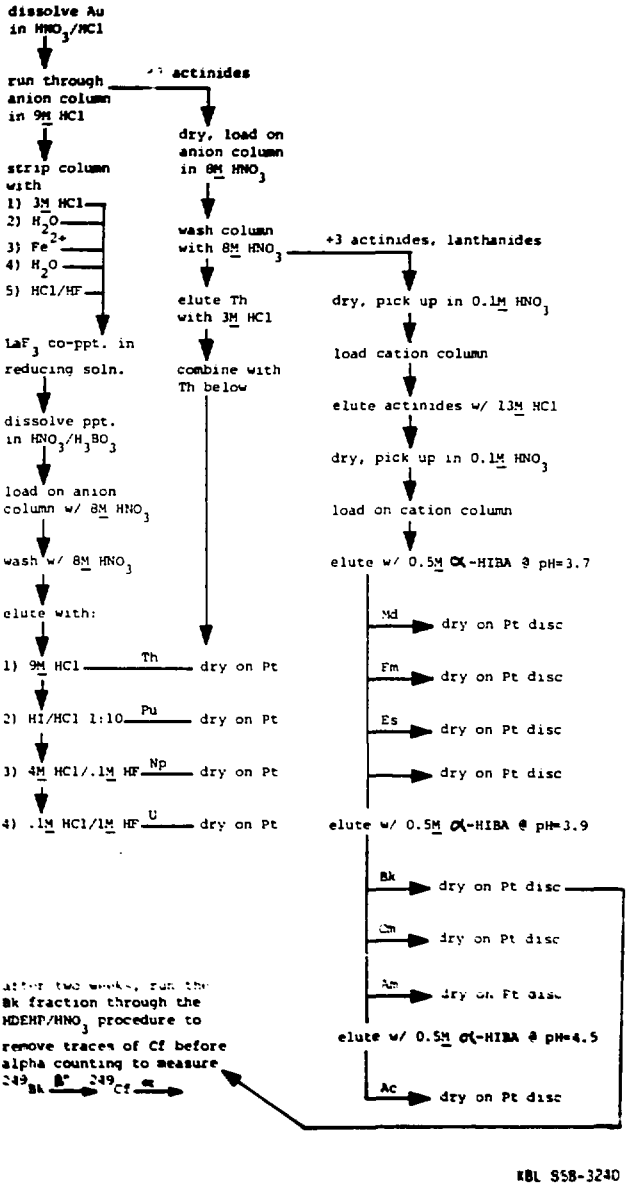

XBL 858-3240

Figure 2.5.9

```
TEST WITH 244CM SPECTRUM THAT IT HAS TWO SEPARATE NUCLIDES
CM_44 1 HAS THE FOLLOWING  2 PEAKS
CM_44 1 PEAK  # 1 AT    5.805+ MeV HAS I-  **.*7*****%
CM_44 1 PEAK  # 2 AT    5.867+ MeV HAS I-  ***.7****%
CM_44 2 HAS THE FOLLOWING  1 PEAKS
CM_44 2 PEAK  # 1 AT    5.764+ MeV HAS I-**********%
RESULTS FOR CHANNELS     1 TO  200
```

ITER	GAUSS WIDTH	EXP SLOPE	TAIL SLOPE	TAIL AMP	AMPLITUDE 1	CENTROID 1	AMPLITUDE 2	CENTROID 2
INIT	.500000E+01	.500000E+01	.200000E+02	.250000E-01	.120000E+04	.738986E+02	.300000E+04	.565802E+02
1	.497605E+01	.292608E+01	.184443E+02	.254687E-01	.117380E+04	.743620E+02	.294249E+03	.566747E+02
2	.496426E+01	.246893E+01	.154645E+02	.252772E-01	.118131E+04	.743607E+02	.315707E+03	.578952E+02
3	.496357E+01	.217021E+01	.146681E+02	.278801E-01	.117726E+04	.743813E+02	.329676E+03	.579239E+02
4	.495709E+01	.206343E+01	.135700E+02	.309972E-01	.117660E+04	.743913E+02	.330192E+03	.579436E+02
5	.495802E+01	.205864E+01	.135842E+02	.300484E-01	.117621E+04	.743926E+02	.330092E+03	.579435E+02
6	.495802E+01	.205950E+01	.135917E+02	.300684E-01	.117623E+04	.743926E+02	.330083E+03	.579432E+02
7	.495803E+01	.205943E+01	.135918E+02	.300684E-01	.117623E+04	.743926E+02	.330085E+03	.579432E+02

IT HAS CONVERGED, HERE ARE THE RESULTS

```
GAUSS WIDTH PARAMETER =  .205652E-01 +/-  .298520E-03 HALF WIDTH AT HALF MAX=  .493802E+01 +/-  .727913E-02 CHANNELS
EXPONENTIAL SLOPE PARM=  .136677E+00 +/-  .392261E-01 DROPS TO 1/2 HEIGHT IN   .205943E+01 +/-  .240018E+00 CHANNELS
EXPONENTIAL TAIL SLOPE=  .509973E-01 +/-  .964509E-02 DROPS TO 1/2 HEIGHT IN   .135918E+02 +/-  .257061E+01 CHANNELS
TAIL HEIGHT / GAUSS HT=  .300684E-01 +/-  .130383E-01
AMP PARM FOR CM244 1  =  .117623E+04 +/-  .178318E+02 GIVES  TOTAL  ACTIVITY=  .154269E+05 +/-  .181411E+03 COUNTS
AMP PARM FOR CM244 2  =  .330085E+03 +/-  .96019E+01 GIVES  TOTAL  ACTIVITY=  .432925E+04 +/-  .112819E+03 COUNTS
CENTROID FOR CM244 1  =  .743926E+02 +/-  .559422E-01 CORRESPONDS TO ENERGY =  .58072DE+01 +/-  .43ae93E-02 MEV
CENTROID FOR CM244 2  =  .579432E+02 +/-  .146046E+00 CORRESPONDS TO ENERGY =  .57e729E+01 +/-  .1453e4E-01 MEV
```

CHAN	ENERGY	COUNTS	SIGMA	CALC COUNTS	% ERROR	CHI**2
1	.562913E+01	.000000E+00	.100000E+01	.138957E+01	.100000E+03	.193090E+01
2	.563155E+01	.300000E+01	.173205E+01	.146443E+01	-.104858E+03	.785995E+00
3	.563398E+01	.200000E+01	.141421E+01	.154406E+01	-.295284E+02	.103939E+00
4	.563641E+01	.300000E+01	.173205E+01	.162907E+01	-.841542E+02	.626483E+00
5	.563883E+01	.600000E+01	.244949E+01	.172021E+01	-.248795E+03	.305277E+01
6	.564126E+01	.700000E+01	.264575E+01	.181847E+01	-.284940E+03	.381547E+01
7	.564368E+01	.600000E+01	.244949E+01	.192516E+01	-.211662E+03	.276758E+01
8	.564611E+01	.300000E+01	.173205E+01	.204206E+01	-.469108E+02	.305866E+00
9	.564854E+01	.300000E+01	.173205E+01	.217151E+01	-.381529E+02	.228800E+00
10	.565096E+01	.300000E+01	.173205E+01	.231366E+01	-.296646E+02	.157021E+00
11	.565339E+01	.400000E+01	.200000E+01	.246883E+01	-.621516E+02	.587655E+00
12	.565582E+01	.500000E+01	.223607E+01	.263936E+01	-.901607E+02	.112399E+01
13	.565824E+01	.400000E+01	.200000E+01	.279840E+01	-.429285E+02	.360840E+00
14	.566067E+01	.200000E+01	.141421E+01	.297120E+01	.326871E+02	.471614E+00
15	.566309E+01	.100000E+01	.100000E+01	.314356E+01	.681669E+02	.459485E+01
16	.566552E+01	.600000E+01	.244949E+01	.331251E+01	-.811315E+02	.120377E+01
17	.566795E+01	.500000E+01	.223607E+01	.347595E+01	-.438457E+02	.464588E+00
18	.567037E+01	.400000E+01	.244949E+01	.363331E+01	-.651386E+02	.933536E+00
19	.567280E+01	.500000E+01	.223607E+01	.378581E+01	-.320722E+02	.294853E+00
20	.567522E+01	.190000E+01	.100000E+01	.393627E+01	.745952E+02	.662166E+01
21	.567765E+01	.400000E+01	.244949E+01	.408872E+01	-.467452E+02	.608832E+00
22	.568008E+01	.400000E+01	.200000E+01	.424775E+01	.581331E+01	.153495E-01
23	.568250E+01	.430000E+01	.200000E+01	.441804E+01	.946212E+01	.436894E-01
24	.568493E+01	.500000E+01	.223607E+01	.460351E+01	-.861178E+01	.314409E-01
25	.568736E+01	.700000E+01	.264575E+01	.480740E+01	-.456089E+02	.666785E+00
26	.568978E+01	.500000E+01	.223607E+01	.503207E+01	-.637313E+00	.205698E-03
27	.569221E+01	.400000E+01	.200000E+01	.527924E+01	.242515E+02	.409114E+00
28	.569464E+01	.600000E+01	.244949E+01	.555035E+01	-.810138E+01	.334982E-01
29	.569706E+01	.600000E+01	.244949E+01	.584698E+01	-.261708E+01	.390253E-02
30	.569949E+01	.400000E+01	.244949E+01	.617136E+01	.277678E+01	.489433E-02
31	.570192E+01	.800000E+01	.282843E+01	.652683E+01	-.225759E+02	.271277E+00
32	.570434E+01	.600000E+01	.244949E+01	.691835E+01	.132748E+02	.180562E+00
33	.570677E+01	.800000E+01	.282843E+01	.735314E+01	-.879711E+01	.523040E-01
34	.570919E+01	.900000E+01	.300000E+01	.784016E+01	.147747E+02	.140137E+00
35	.571162E+01	.100000E+02	.316228E+01	.837[illegible]	[illegible]	.[illegible]

XBL 857-3112

Figure 3.3.1

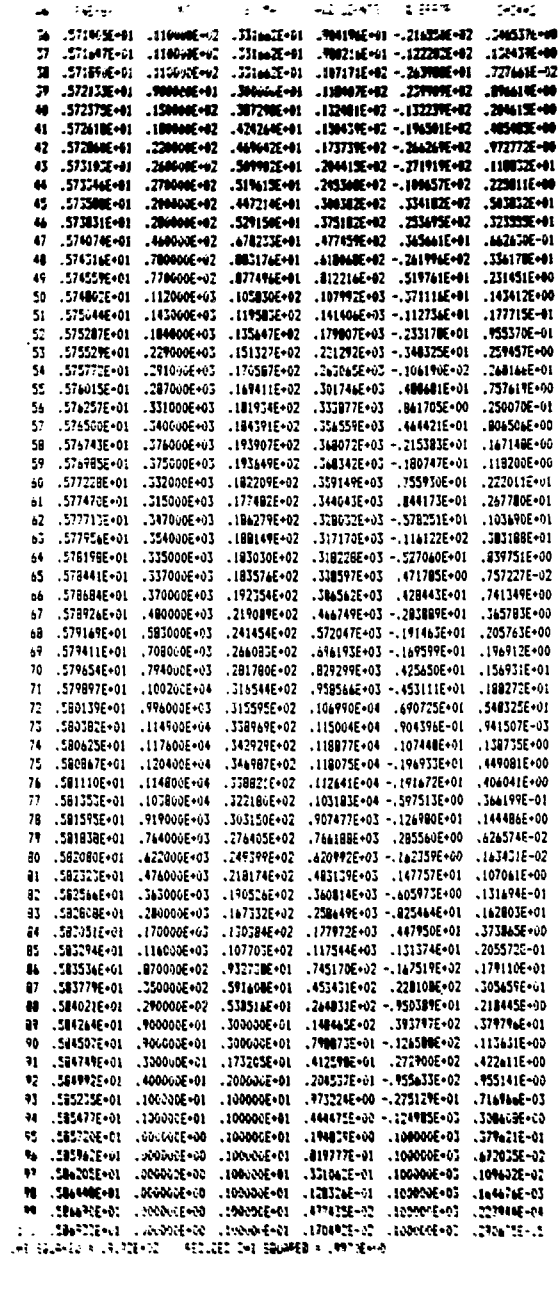

XBL 857-3113

Figure 3.3.2

RESULTS FOR TEST THREE COMPONENTS Zm, aM, SBN VARY ALL PARAMETERS
3 THREE COMPONENTS

ITER	M.L. 01	I.A. 01	M.L. 02	I.A. 02	M.L. 03	I.A. 03	M.L. 04	I.A. 04
INIT	.2e0J0vE+01	.9803e6E+04	.5e6e00E+01	.110e00E+04	.e6e600E+02	.90e60JE+02		
1	.20IB9IE+01	.184776E+05	.750865E+01	.602609E+03	.5402666+02	.9121551E+02		
2	.2025935E+01	.1028J3E+05	.650249E+01	.813343E+03	.5991099+02	.885972E+02		
3	.20162JE+01	.1025576+05	.669447E+01	.847019E+03	.5846008+02	.845380E+02		
4	.2018416+01	.1026955+05	.668380E+01	.837232E+03	.586675E+02	.842175E+02		
5	.2016716+01	.102705E+05	.668359E+01	.836768E+03	.586413E+02	.842463E+02		
6	.2016716+01	.102702E+05	.668347E+01	.836871E+03	.586377E+02	.842519E+02		
7	.2016726+01	.102702E+05	.668346E+01	.836881E+03	.586380E+02	.842515E+02		

IT HAS CONVERGED . . . HERE ARE THE RESULTS

PARAMETER	VALUE	SIGMA
1	.2016706+01	.5866J2E-01
2	.192702E+05	.196919E-3
3	.668346E+01	.112765E+01
4	.836881E+03	.208523E+03
5	.586380E+02	.209692E+02
6	.8425156+02	.248498E+02

RATE	COR. RATE	SIGMA	TIME	DELTA T	A CALC	I ERROR	CHI**2
.9644J2E+04	.809935E+04	.9e7753E+02	.100000E+01	.1000JCE+01	.812069E+04	-.263573E+03	.486a60E-01
.5686986+04	.591372E+04	.826145E+02	.2000006+01	.1000006+01	.592706E+04	-.225626E+03	.2608486-01
.4408026+04	.707740E+04	.500000E+01	.100000E+01	.435690E+04	.115974E+03	.521750E+00	
.3236486+04	.608852E+02	.400000E+01	.100000E+01	.323028E+04	.140794E+00	.559566-02	
.2446096+04	.526346+02	.500000E+01	.100000E+01	.241946E+04	.116970E+01	.295958E+00	
.1805236+04	.457648E+02	.6000006+01	.100000E+01	.183374E+04	-.157941E+01	.388139E+00	
.1354586+04	.400475E+02	.700000E+01	.100000E+01	.140868E+04	-.323216E+01	.1212876+01	
.1019076+04	.352955E+02	.800000E+01	.100000E+01	.109848E+04	.183990E+01	.340303E+00	
.7666166+03	.3137486+02	.9134866+01	.900000E+01	.1000006+01	.870585E+03	-.197220E+01	.288486E+00
.5776086+03	.2807076+02	.1000006+02	.100000E+01	.701805E+03	.139142E+01	.1244596+00	
.4346156+03	.2536526+02	.1100006+02	.100000E+01	.575a3ZE+03	-.800062E+00	.3249716-01	
.3276356+03	.2310736+02	.1200006+02	.100000E+01	.4802916+03	-.36a976E+00	.5791736-02	
.2476176+03	.2117826+02	.1300006+02	.100000E+01	.407370E+03	.231276E+01	.207495E+00	
.1876046+03	.1951856+02	.1400006+02	.100000E+01	.350852E+03	.392543E+00	.4984046-02	
.1429496+03	.1809806+02	.1500006+02	.100000E+01	.306417E+03	.688a80E+00	.1543926+01	
.1096116+03	.1682156+02	.1600006+02	.200000E+01	.276963E+03	.1549796+01	.1166406E+00	
.8381976+02	.1566956+02	.1700006+02	.200000E+01	.218623E+03	-.597579E+01	.1252106+01	
.6661446+02	.1459696+02	.1800006+02	.200000E+01	.1822926+03	-.134726E+01	.5893196-01	
.5142746+02	.1362106+02	.1900006+02	.200000E+01	.1557a0E+03	-.199718E+01	.1105586+00	
.3981676+02	.1273476+02	.2000006+02	.200000E+01	.1355786+03	.a3u896E+00	.1020716-01	
.3087256+02	.1194a6E+02	.2100006+02	.200000E+01	.1197516+03	-.8764a6E+01	.2962486+00	
.2396146+02	.1125826+02	.2200006+02	.200000E+01	.107059E+03	.737402E+01	.1280a6E+01	
.1859496+02	.1061096+02	.2300006+02	.200000E+01	.9a7150E+02	.4535a6E+01	.3759466+00	
.1443a76+02	.1002a76+02	.2400006+02	.200000E+01	.881818E+02	-.138421E+01	.3137556-01	
.1119716+02	.9459206+02	.2500006+02	.200000E+01	.810732E+02	-.8a888E+01	.9825446+00	
.8681696+02	.8930596+02	.2600006+02	.200000E+01	.7516186+02	.433586E+01	.2922986+00	
.6736596+02	.8426916+02	.2700006+02	.200000E+01	.7004606+02	.3a3951E+01	.1894466+00	
.5226356+02	.a055316+02	.2800006+02	.200000E+01	.657332E+02	-.8554a7E+01	.773a27E+00	
.4054846+02	.a075536+02	.2900006+02	.200000E+01	.620257E+02	-.208590E+01	.4905686-01	
.3a33a2E+02	.577446E+02	.3000006+02	.200000E+01	.588132E+02	-.1851a7E+01	.3a81a1E-01	
.2a78146+02	.5249746+02	.3100006+02	.200000E+01	.5600a9E+02	-.372143E+01	.136552E+00	
.2336946+02	.5a2a05E+02	.3200006+02	.200000E+01	.535249E+02	.484471E+01	.1a2906E+00	
.1811816+02	.5438926+02	.3300006+02	.200000E+01	.513287E+02	.5a6854E+01	.a74572E+00	
.1451976+02	.4ea856E+02	.3400006+02	.200000E+01	.4759346+02	-.194396+01	.6472196-01	
.1166a66+02	.4722256+02	.3500006+02	.200000E+01	.4446786+02	.6212346+01	.a84076E+00	
.3985546+02	.4101936+02	.3600006+02	.200000E+01	.4187386+02	-.198554E+01	.5993a6E-01	
.3726816+02	.3a2746+02	.3700006+02	.200000E+01	.395059E+02	-.316479E+01	.1484a6E+00	
.2a6l 5E+02	.22ea.6E+02	.3800006+02	.200000E+01	.3741606+02	-.145a76E+01	.221a6E-01	
.2324a6E+02	.3a2ea3E+02	.3900006+02	.200000E+01	.355196E+02	.216811E+01	.a72725E-01	
.3549476+02	.3a3923E+02	.2948126+01	.7800006+02	.4000006+01	.337647E+02	.729226E+01	.790118E+00

XBL 857-3111

Figure 3.4.1

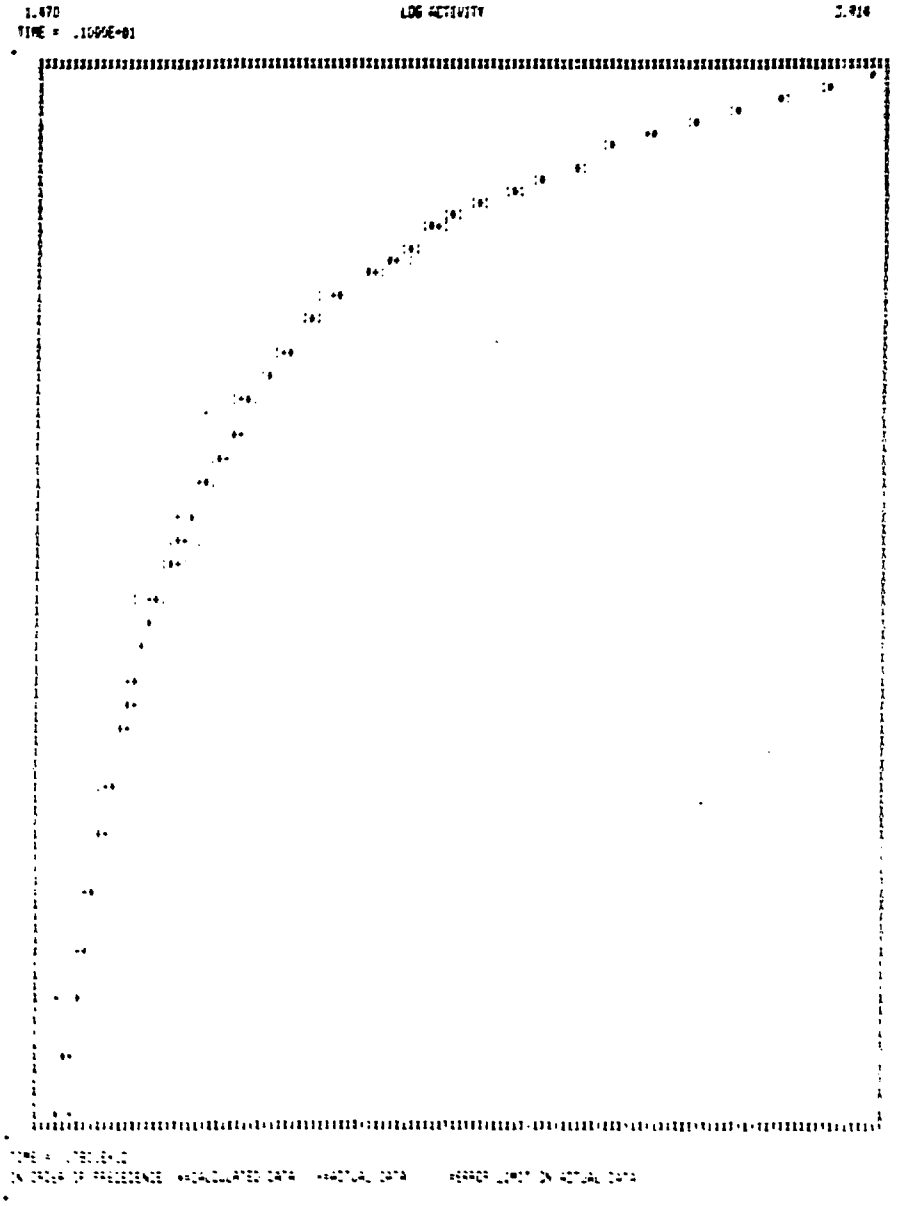

XBL 857-3110

Figure 3.4.2

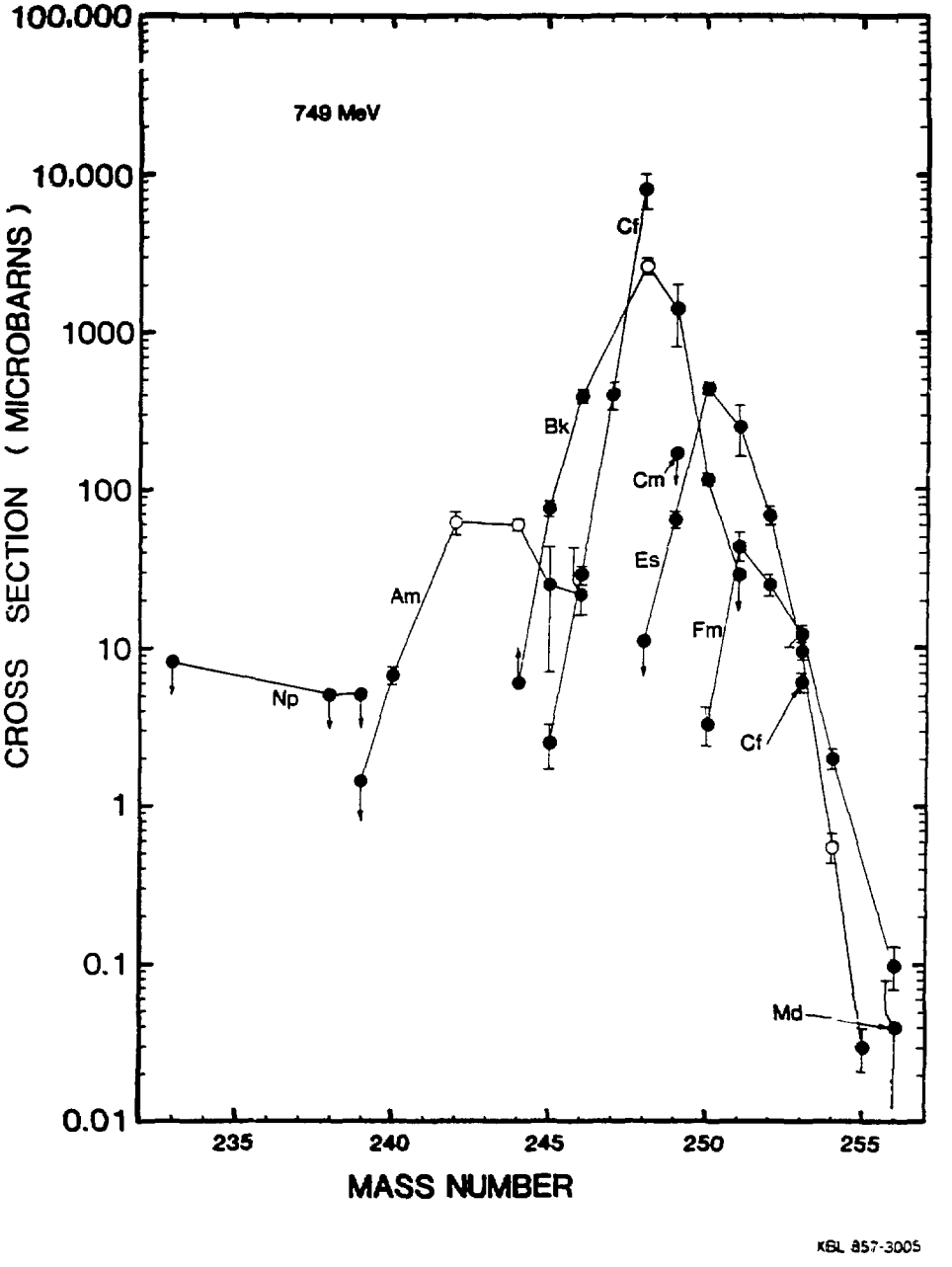
749 MeV
CROSS SECTION (MICROBARNS)
100,000
10,000
1000
100
10
1
0.1
0.01
235
240
245
250
255
MASS NUMBER
Np
Am
Cf
Bk
Cm
Es
Fm
Cf
Md
KBL 857-3005

Figure 4.2.1

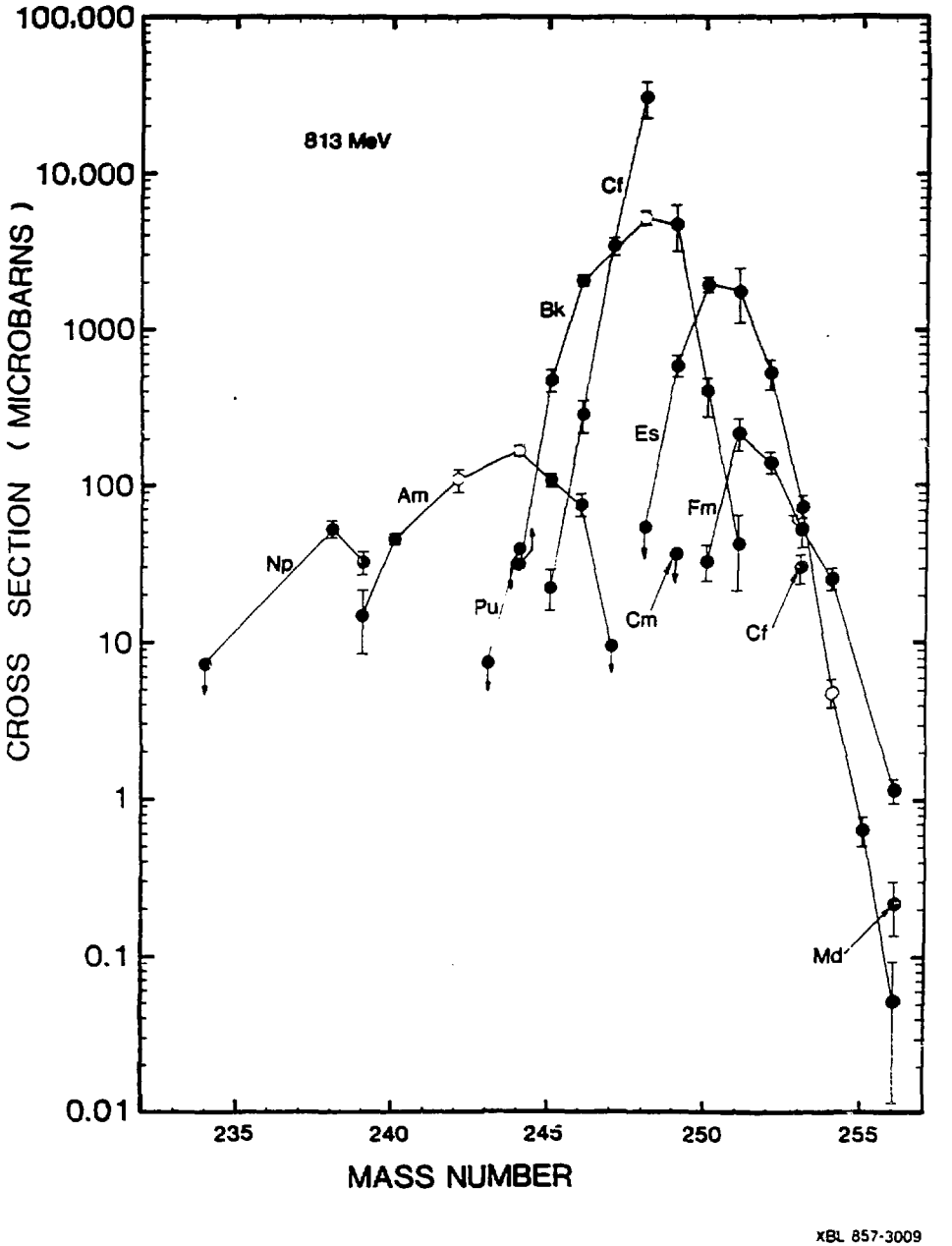
100,000
10,000
1000
100
10
1
0.1
0.01
CROSS SECTION (MICROBARNS)
813 MeV
Np
Am
Pu
Cm
Cf
Bk
Cf
Es
Fm
Md
235
240
245
250
255
MASS NUMBER
XBL 857-3009

Figure 4.2.2

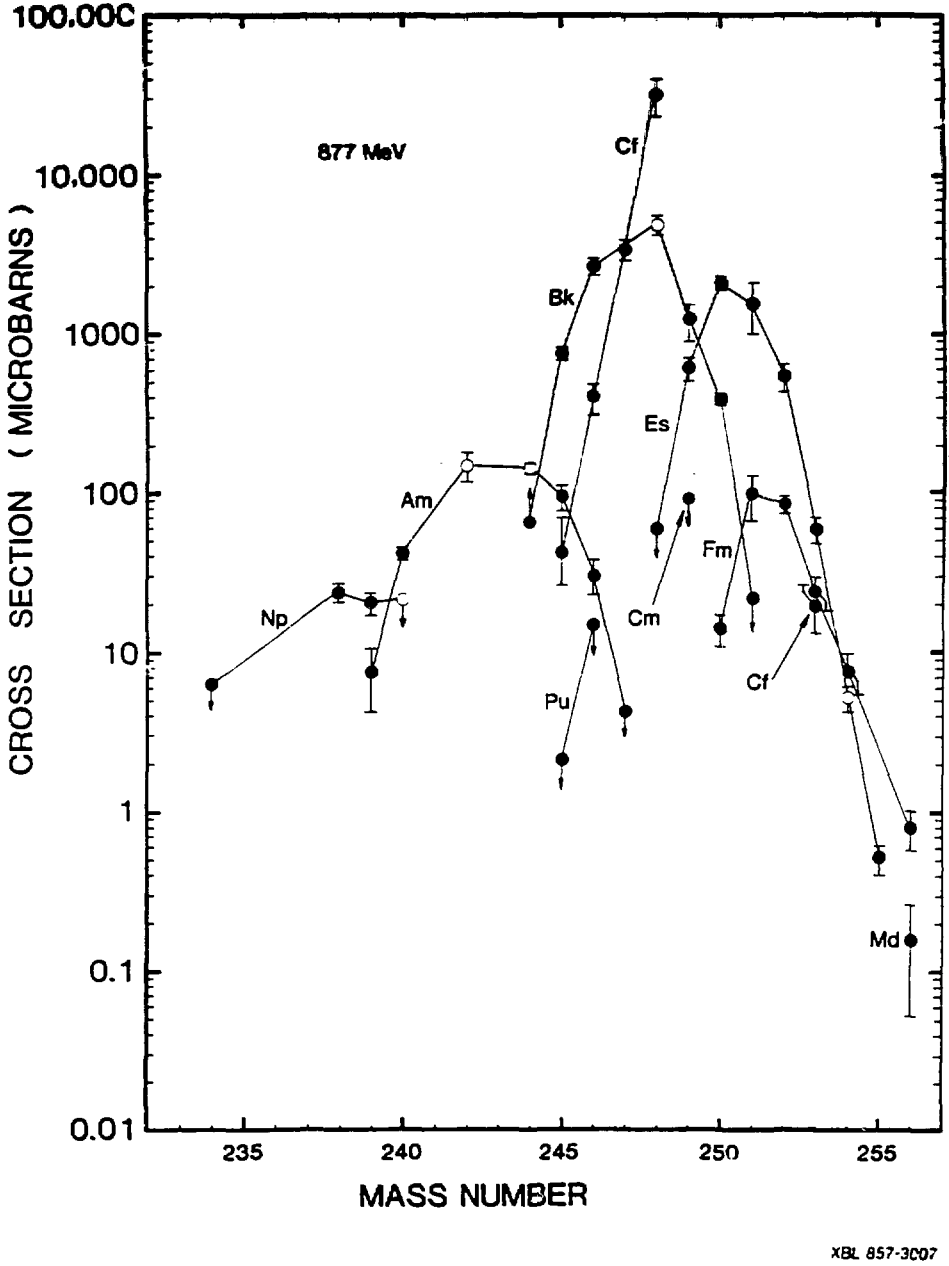
100,000
10,000
1000
100
10
1
0.1
0.01
CROSS SECTION (MICROBARNS)
877 MeV
Cf
Bk
Es
Fm
Am
Np
Cm
Pu
Cf
Md
235
240
245
250
255
MASS NUMBER
XBL 857-3007

Figure 4.2.3

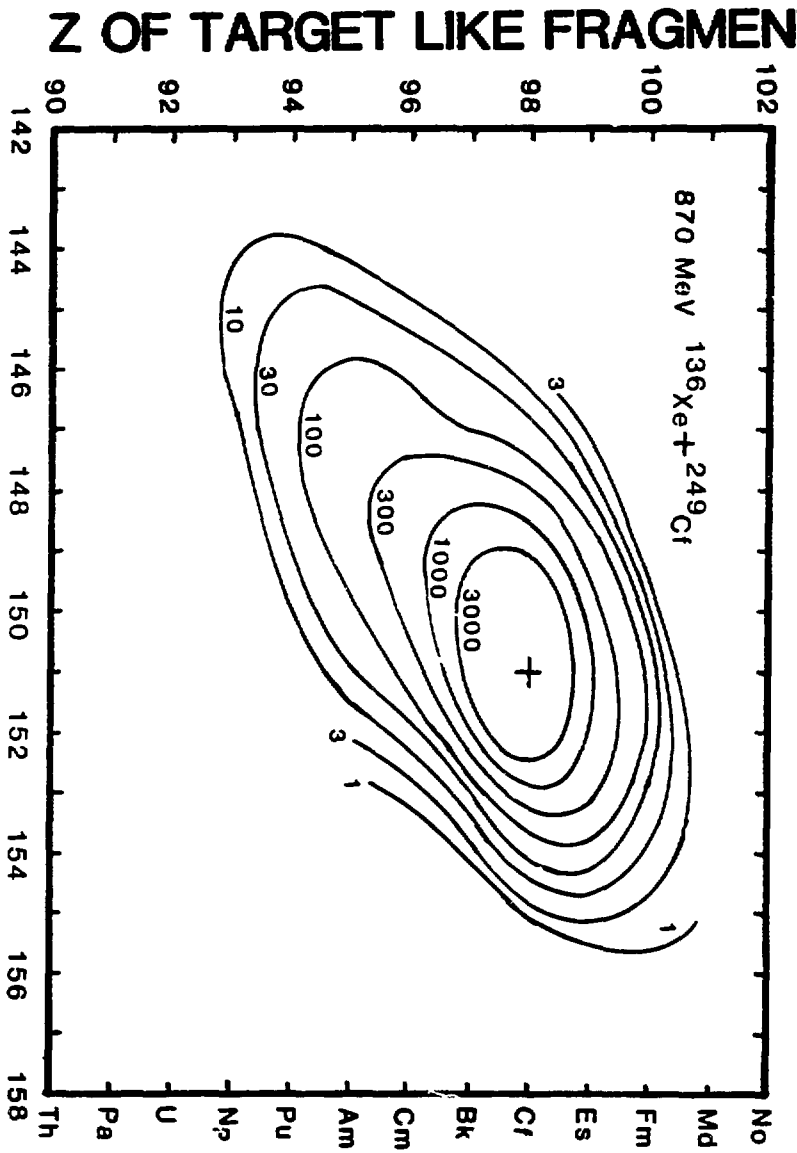

Figure 4.2.4

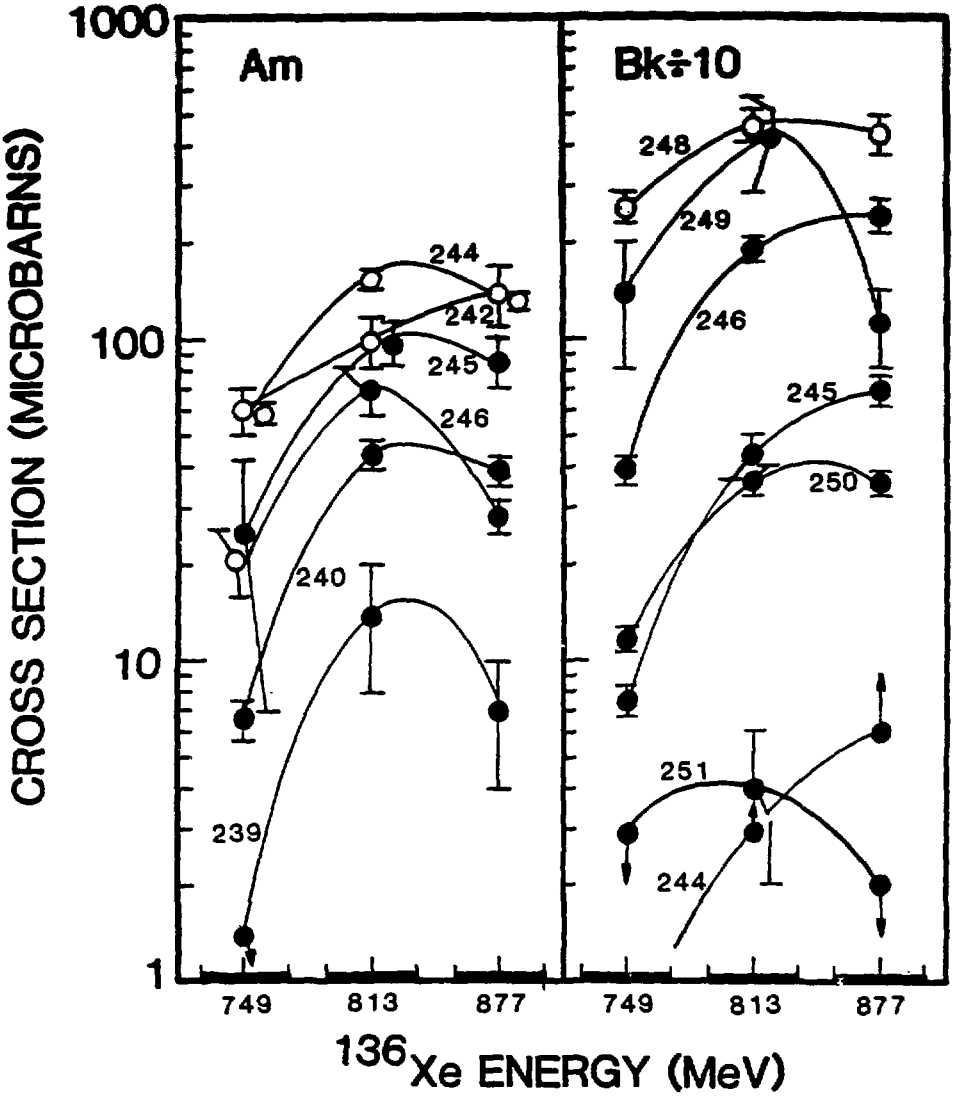

XBL 857-3108

Figure 4.2.5

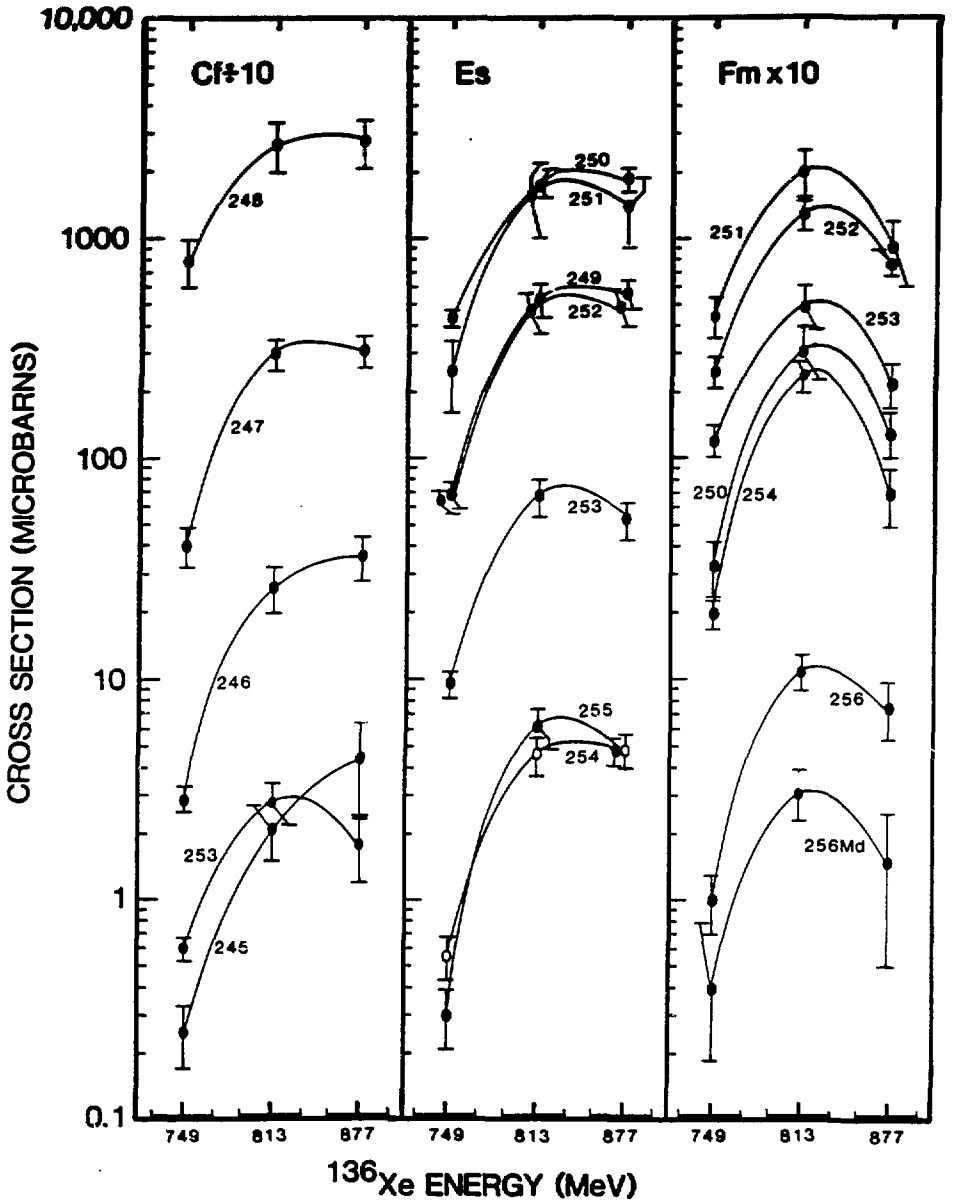

XBL 857-3109

Figure 4.2.6

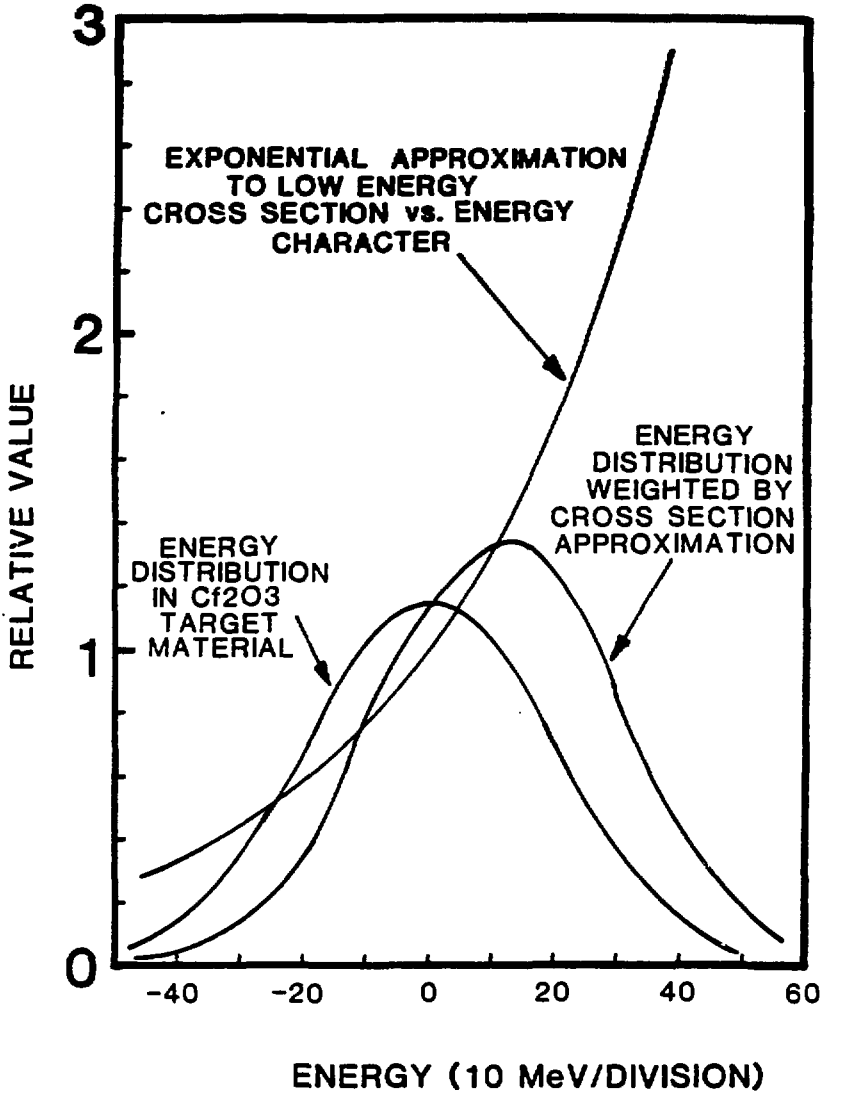

XBL 857-3106

Figure 4.2.7

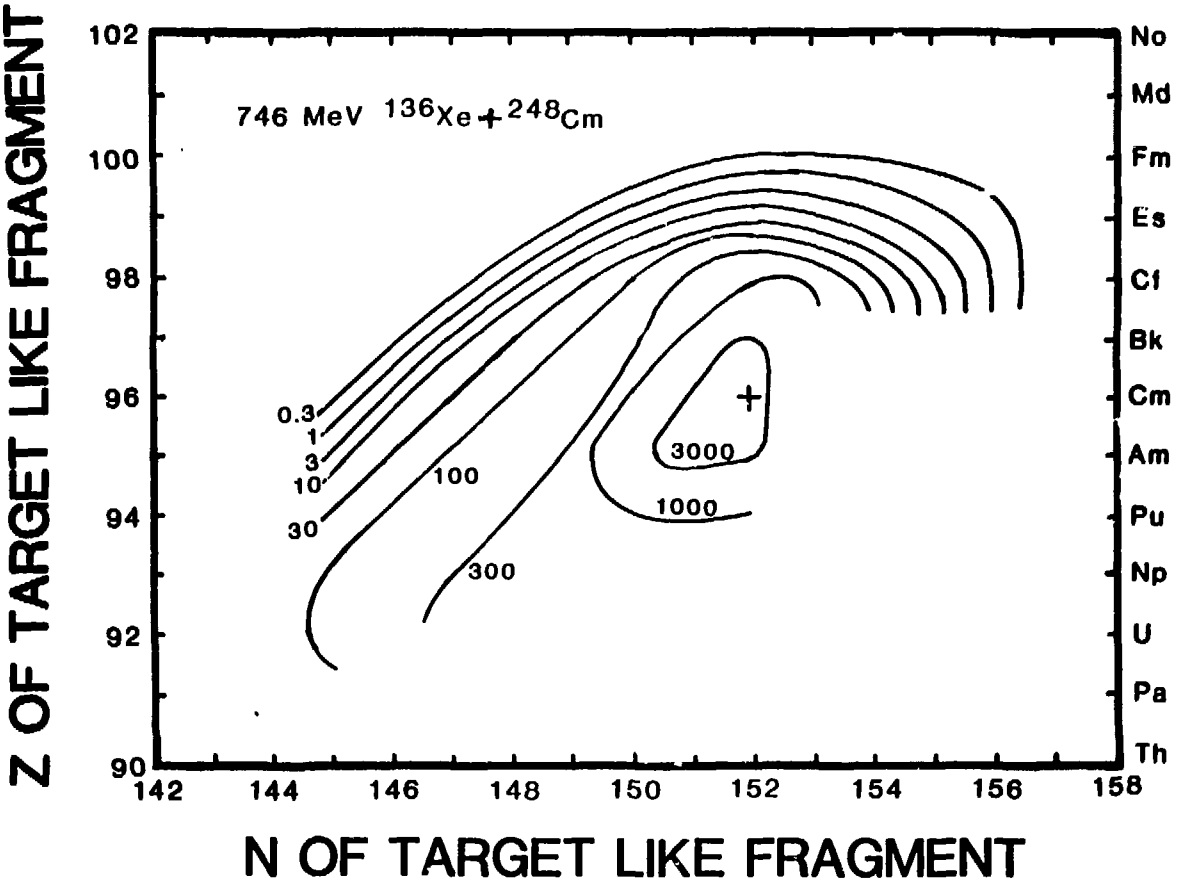

Figure 4.3.1

XBL 858-3243

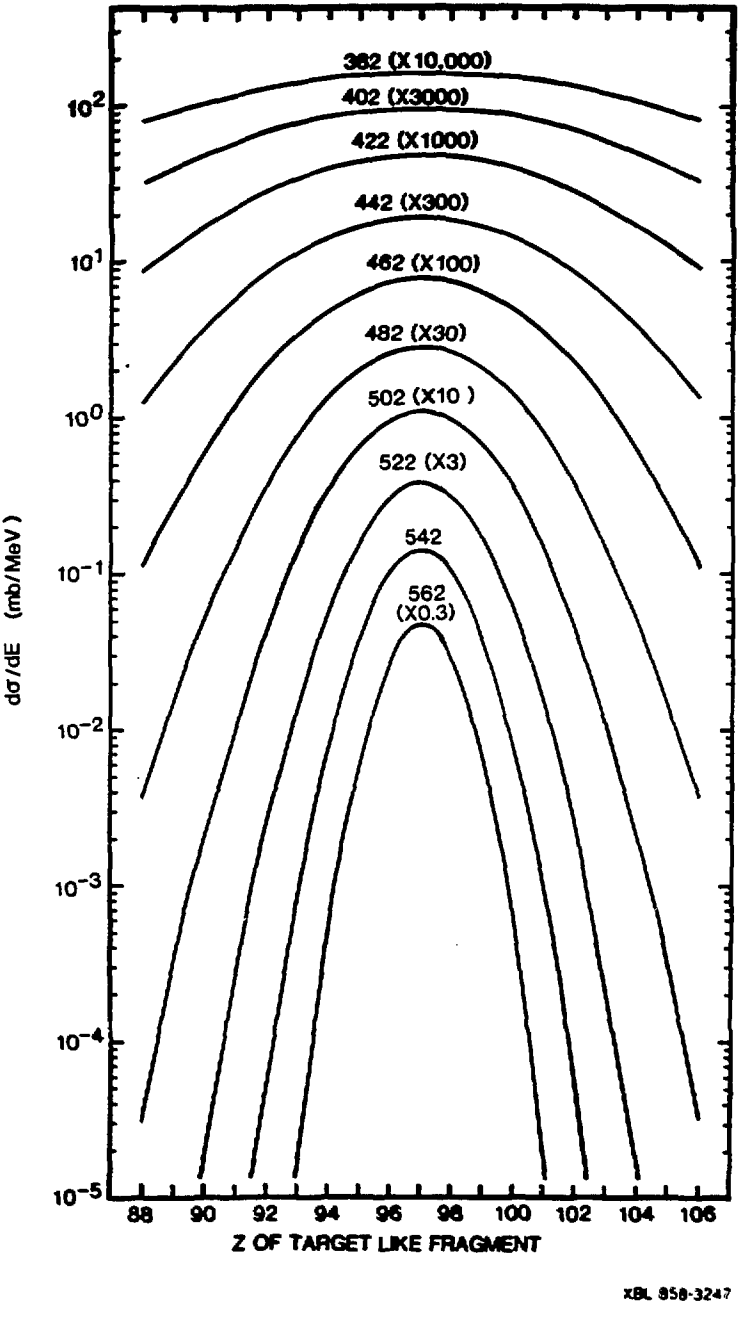
382 (X10,000)
402 (X3000)
422 (X1000)
442 (X300)
462 (X100)
482 (X30)
502 (X10)
522 (X3)
542
562
(X0.3)
dσ/dE (mb/MeV)
Z OF TARGET LIKE FRAGMENT
88 90 92 94 96 98 100 102 104 106
XBL 858-3247

Figure 5.2.1

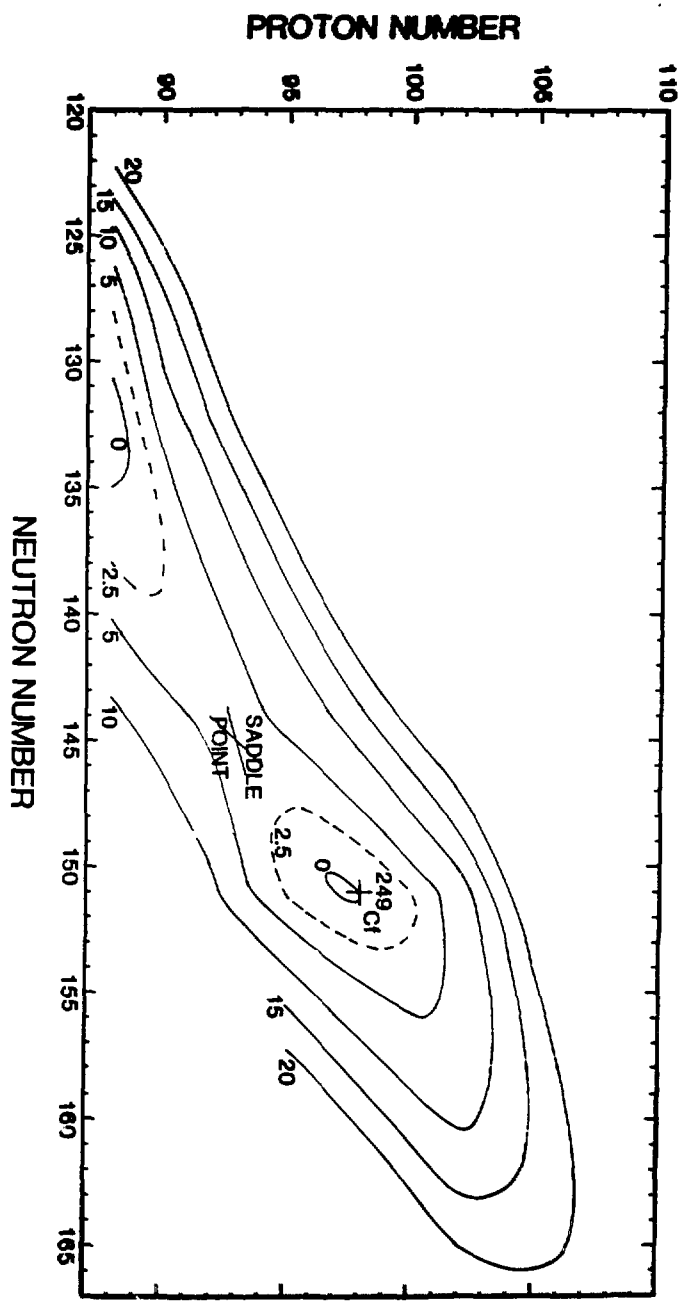

KBL 657.3008

Figure 5.3.1

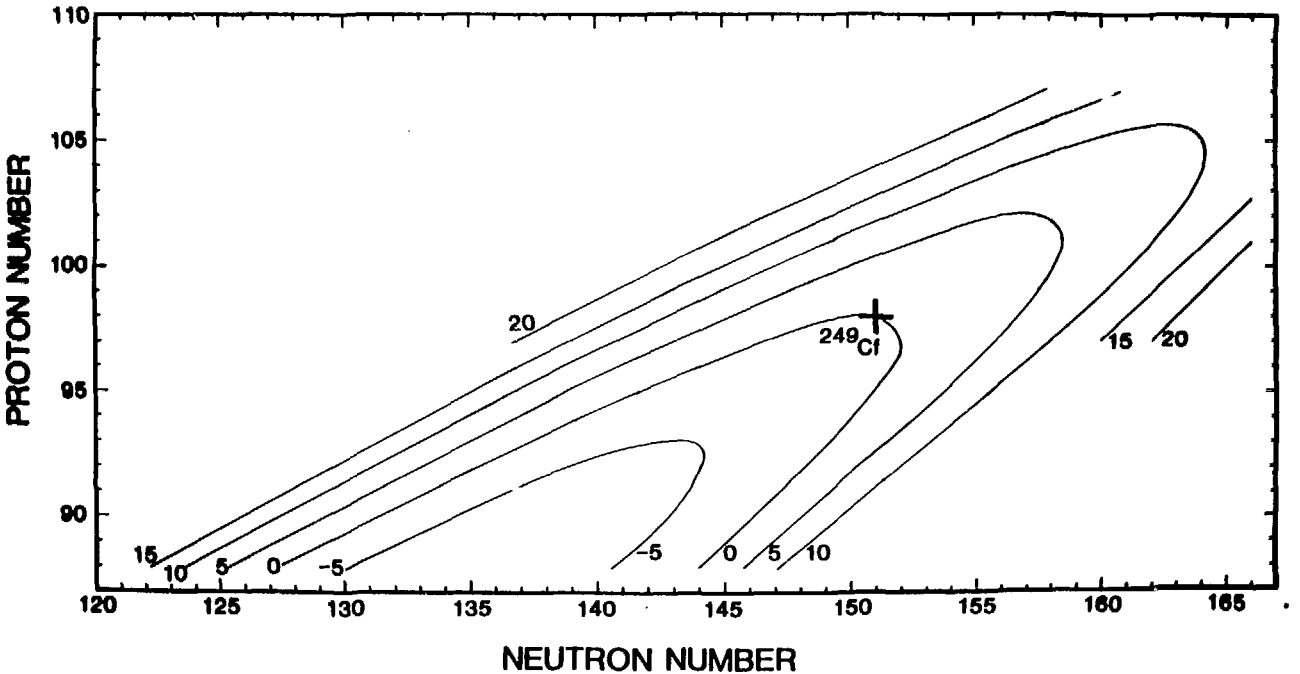

XBL 857-3006

Figure 5.3.2

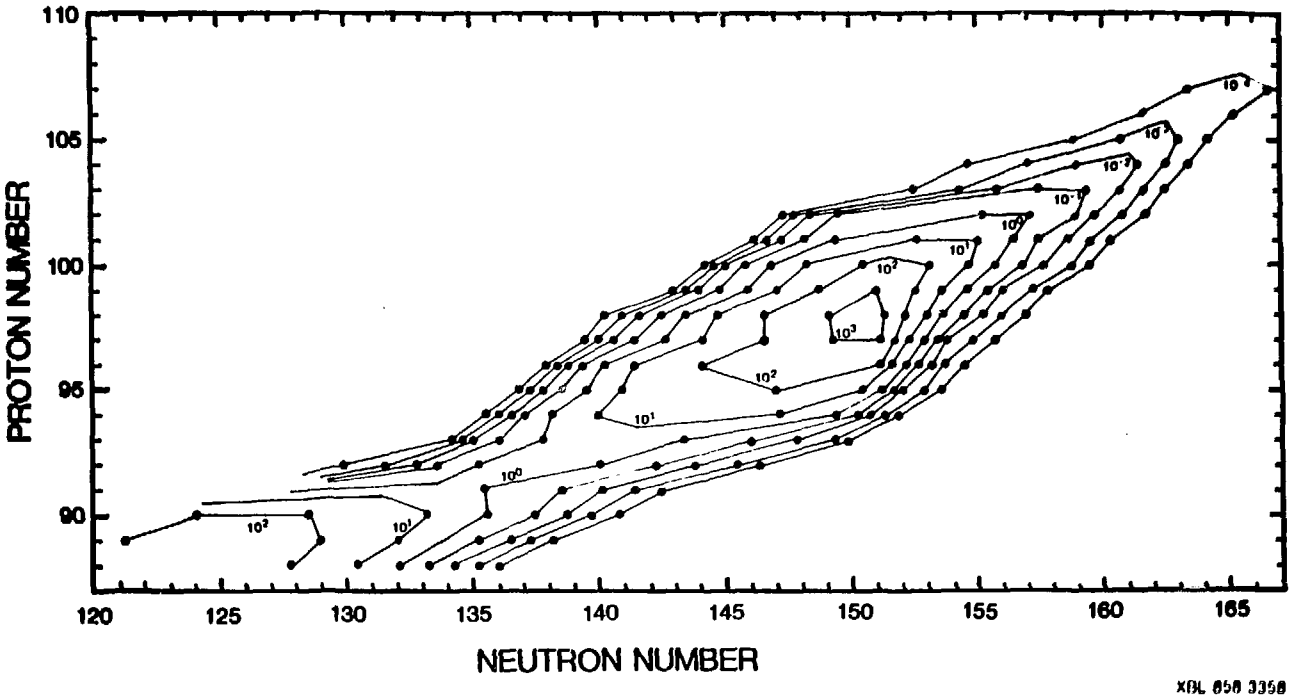
PROTON NUMBER
NEUTRON NUMBER
110
105
100
95
90
120
125
130
135
140
145
150
155
160
165
XBL 858 3358

Figure 5.6.2

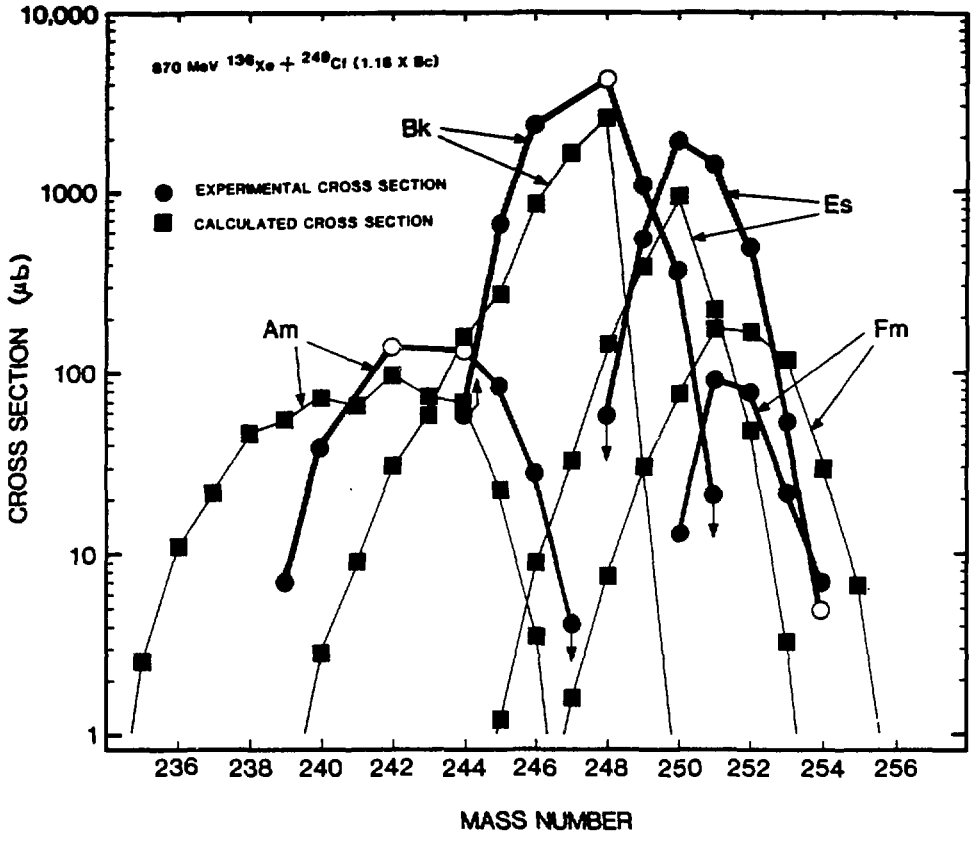

XBL 858-3248

Figure 5.6.3

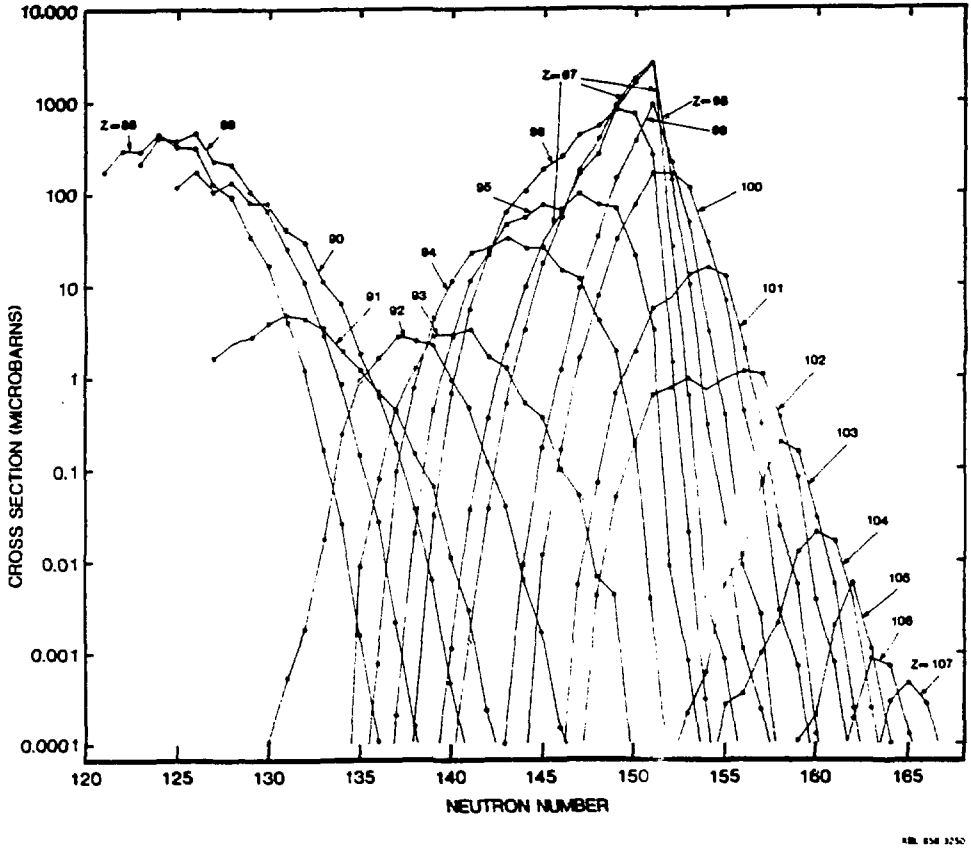
10.000
1000
100
10
1
0.1
0.01
0.001
0.0001
CROSS SECTION (MICROBARNS)
120
125
130
135
140
145
150
155
160
165
NEUTRON NUMBER
Z=97
Z=98
Z=107
90
91
92
93
94
95
96
98
99
100
101
102
103
104
105
106

Figure 5.6.1

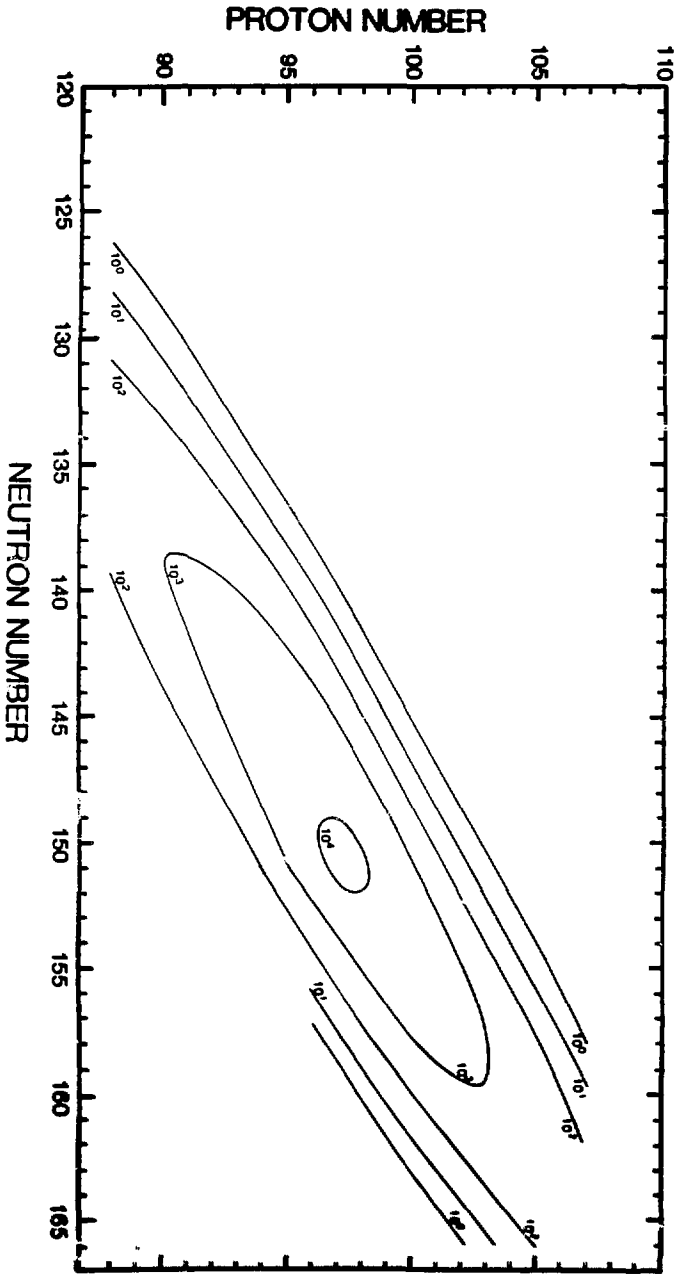

KBL 860 3357

Figure 5.4.1

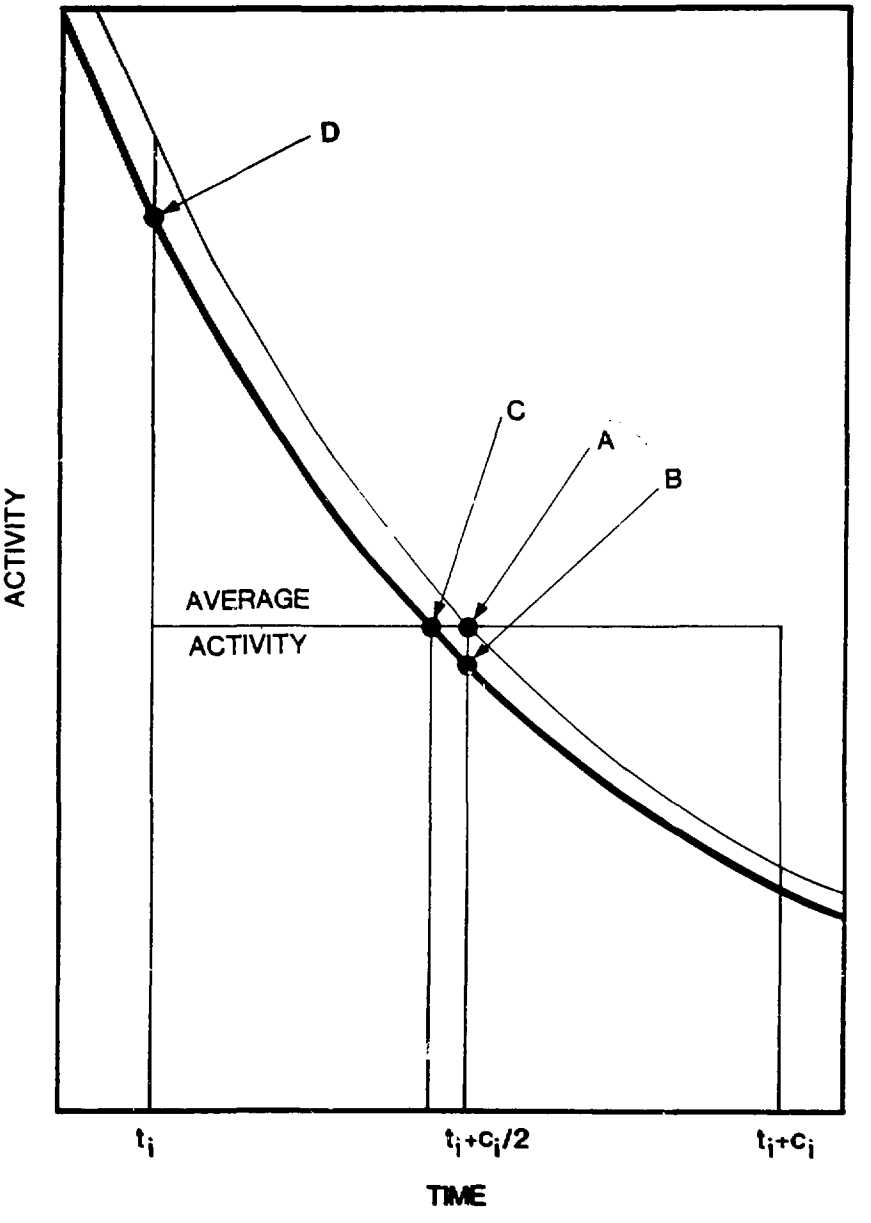

XBL 858-3249

Figure A1